

THESIS ON MECHANICAL ENGINEERING E81

Design Optimization of Smart Composite Structures with Embedded Devices

HENRIK HERRANEN

TUT
PRESS

TALLINN UNIVERSITY OF TECHNOLOGY
Faculty of Mechanical Engineering
Department of Machinery

This dissertation was accepted for the defence of the degree of Doctor of Philosophy in Mechanotechnics on May 21, 2014.

Supervisor: Prof. Martin Eerme, Dr.Sci.Math. Jüri Majak

Faculty of Mechanical Engineering, TUT

Opponents: Dr. Andrey Aniskevich

Institute of Polymer Mechanics, University of Latvia

Dr. Harri Lille

Institute of Forestry and Rural Engineering, Estonian University of Life Sciences

Defence of the thesis: June 19, 2014

Declaration:

Hereby I declare that this doctoral thesis, my original investigation and achievement, submitted for the doctoral degree at Tallinn University of Technology has not been submitted for any academic degree.

/töö autori nimi ja allkiri/



European Union
European Social Fund



Investing in your future

Copyright: Henrik Herranen, 2014

ISSN 1406-4758

ISBN 978-9949-23-641-1 (publication)

ISBN 978-9949-23-642-8 (PDF)

MEHCHANOTEHNIKA E81

**Integreeritud
elektroonikakomponentidega targa
komposiitmaterjali väljatöötamine**

HENRIK HERRANEN

CONTENTS

LIST OF PUBLICATIONS.....	7
INTRODUCTION.....	8
Problem Statement	8
Main Objectives	9
Hypothesis.....	10
ABBREVIATIONS	11
SYMBOLS.....	12
1. THEORETICAL BACKGROUND	13
1.1 Composite Materials and Structures.....	13
1.2 Structural Health Monitoring Systems	13
1.3 Advantages of Embedded Sensors	14
1.4 Sensor Size Concerns	16
1.5 The Influence of Foreign Objects on Mechanical Properties of Composite Material	17
1.6 Physical Interfacing of Sensor Node Body and Composite Matrix.....	17
1.7 Methodology for Development of Smart Composite	18
2. DESIGN OF BASE COMPOSITE MATERIAL.....	20
2.1 Introduction	20
2.2 Experimental Testing	20
2.3 Finite element model of sandwich panel	20
2.4 Optimal Design of Sandwich Panel.....	21
2.4.1 Pareto Frontier	22
2.5 Conclusions	22
3. DESIGN OF ELECTRONIC COMPONENTS	24
3.1 Electronics Miniaturization Possibilities.....	24
3.1.1 Small Size Chips and Bare Integrated Electronics	24
3.1.2 Flexible Substrate Technology	26
3.1.3 Ceramic Substrate Technology.....	27
3.2 Low Cost Strain Sensor Experimental Testing	28
3.2.1 Introduction	28
3.2.2 Method.....	29
3.2.3 Results	30
3.2.4 Summary and Outlook for the Strain Gauge	32

4.	DESIGN OF SMART COMPOSITE.....	33
4.1	First Attempt of Full Embedment.....	33
4.2	Examination of Specimens After Testing.....	34
4.3	Finite Element Analysis Model and Validation	35
4.4	Summary of the Results of First Embedment.....	39
4.5	Design and Optimization of Embedded Foreign Object Geometry.....	39
4.6	Methodology	40
4.7	Specimen Design.....	40
4.8	Higher Level Design	41
4.9	Lower Level Design	42
4.10	Specimen Manufacturing	43
4.11	Examination of Preliminary Specimens	44
4.12	Design of New Specimens	44
4.13	Examination of new specimens.....	44
4.14	Mechanical Testing	45
4.15	Digital Image Correlation Results	46
4.16	Microscale FE Model	54
5.	CONCLUSIONS.....	59
	REFERENCES.....	61
	OTHER PUBLICATIONS.....	65
	AKNOWLEDGEMENTS	66
	ABSTRACT	67
	KOKKUVÕTE.....	69
	APPENDICES.....	71
	Appendix 1	73
	Appendix 2	79
	Appendix 3	133
	Appendix 4.....	136

LIST OF PUBLICATIONS

This thesis is based on the following publications which are presented in Appendix 2 and referred in the text by their according Roman numerals I-V.

- I. H. Herranen, O. Pabut, M. Eerme, J. Majak, M. Pohlak, J. Kers, M. Saarna, G. Allikas, A. Aruniit, "Design and Testing of Sandwich Structures with Different Core Materials" *Materials Science (Medžiagotyra)*, Kaunas University of Technology, vol. 18, no. 1, pp. 1-6, 2012.
- II. H. Herranen, J. Kers, J. Preden, R. Talalaev, M. Eerme, J. Majak, M. Pohlak, H. Lend, G. Allikas, "Embedded Electronics Influence on the Strength of Carbon Fiber Laminate" in *Advanced Material Research, Trans Tech Publications*, vol. 905, pp.239-243, 2014.
- III. H. Herranen, G. Allikas, M. Eerme, K. Vene, T. Otto, A. Gregor, M. Kirs, K. Mädamürk, "Visualization of Strain Distribution Around The Edges of a Rectangular Foreign Object Inside The Woven Carbon Fibre Specimen" *Estonian Journal of Engineering*, vol. 18, no.3, pp. 279-287, 2012.
- IV. H. Herranen, T. Saar, R. Gordon, M. Pohlak, H. Lend, "Durability Performance of Semiconductor Strain Gauges In GFRP Laminate," in *Proceedings of 6th ECCOMAS Thematic Conference on Smart Structures and Materials (SMART2013)*, 2013.
- V. H. Herranen, H. Lend, A. Kuusik, S. Czichon, J. Kers, M. Piirlaid, "Foreign Object Induced Fiber Undulation Influence On Mechanical Properties Of Composite Laminate," in *Proceedings of 19th International Conference on Composite Materials (ICCM19)*, 2013.

INTRODUCTION

Problem Statement

This dissertation is focused on the development of a smart composite material. The smart materials field is a new emerging field of materials systems which combines materials science with information science. In general a smart material is defined as a material that is capable of reacting to stimuli or the environment in a prescribed manner[1].

Current study is focused on smart materials with the ability to sense and process information about the environmental conditions and on its own structural health. Smart materials have often embedded sensorics[1]. Embedding foreign structures inside a composite causes structural mismatch and integrity problems. At the same time it has many benefits, which makes embedding desirable for composites. The result of embedment is a complex smart material system, which feasible realization can be considered as the solution of a multicriteria and multilevel optimization problem.

The multicriteria optimization problem for design of smart composites can be formulated as follows:

$$F(\bar{x}) = (F_1(\bar{x}), F_2(\bar{x}), F_3(\bar{x}), \dots, F_n(\bar{x})) \quad (1.1)$$

subjected constraints in form of equalities or inequalities

$$x_i \leq x_i^*, \quad -x_i \leq x_{i*}, \quad (i = 1, \dots, n), \quad (1.2)$$

$$g_j(\bar{x}) \leq 0, \quad (j = 1, \dots, m), \quad (1.3)$$

$$h_k(\bar{x}) = 0, \quad (k = 1, \dots, l). \quad (1.4)$$

In (1.1)-(1.4) \bar{x} is the vector of design variables and the objective functions are given as

$F_1(\bar{x})$ - stiffness characteristic (strain energy density, etc.)

$F_2(\bar{x})$ - strength characteristic (max stress, max strain, failure index, etc.)

$F_3(\bar{x})$ - collected information characteristic (values of acceleration, stress, strain, humidity, etc.)

$F_4(\bar{x})$ - energy consumption characteristic

$F_5(\bar{x})$ - cost of the structure

$F_6(\bar{x})$ - life expectancy of the structure

Finding an effective solution to a posed problem means that the stiffness and strength of the structure are maximized, the energy consumption is minimized and necessary information acquired.

Main Objectives

Recent advances in sensors and related electronics, communication and signal processing offer in-situ monitoring possibilities of the geometric, environmental, and structural characteristics of composite structures[2],[3].

The main objective of the current study is the development of methodology for design of smart composites with structural health and performance monitoring capabilities. Such materials provide a non-destructive evaluation possibility for detecting damage in composite materials. The study is focused on design of composite structures with fully integrated embedded systems (sensors/actuators) which are able to convey data and information in real time.

Another issue of no lesser importance is validation on proposed methodology in laboratory tests and real world applications. The laboratory tests performed include fatigue tests of smart material with embedded electronics, sensor tests for energy consumption and acquiring information, stiffness and strength test of the base material and smart materials/structures.

Furthermore, wind turbine blades with embedded electronics are designed and tested in field conditions (Estonian company “Goliath Wind OÜ”). The measured characteristic was acceleration.

The main objective of the study can be achieved by completing several complex subtasks which cover essentially quite different disciplines like material science, mechanics, electronics, software development, etc. For that reason the author of the thesis has made collaboration with researchers of the Seebeck Institute of Electronics.

In general, the manufacturing process of smart composite considered can be divided into three main subtasks: manufacturing of base composites, design and manufacturing of electronic components, embedding electronic components in base composites. These subtasks can be performed separately, but are influenced by each other. A smart composite with improved properties can be obtained by performing optimization for each subtask, but not only. For example the electronic component with maximum information acquiring capabilities has typically too large dimensions to perform well as an integrated component. Due to conflicting objectives the optimization should cover also a global level i.e. smart composite level.

Based on above discussion the sub-objectives of the study can be outlined as:

- minimization of the impact of embedded components on strength and stiffness properties of the composite structure
- improvement of the embeddement process of electronic components in host material
- minimization of manufacturing expences of the smart structure

Obviously, the proposed sub-objectives uphold the main objective of the study.

Hypothesis

This research presents efforts to develop structural composite materials which include networks of sensors that extend the functionality of the composite materials to be aware of its own health condition.

The main hypothesis of the thesis can be outlined as follows:

H1: The impact of embedded electronics on strength and stiffness properties of the composite material/structure can be minimized by properly performed design of base composite and electronic components.

H2: Introducing of ALT technology for design of smart composites makes integration of embedded electronics in host composites more flexible.

H3: Using ALT technology together with wireless electronic systems forms a new environment and perspective in the design of smart composites.

H4: Smart composite with embedded electronics can be manufactured with reasonable expenses.

The working hypothesis proposed can be regarded as confirmation of the fact, that the aims of the study are attainable.

ABBREVIATIONS

AM	additive manufacturing
ANN	artificial neural networks
ALT	additive layer technology
CAD	computer aided design
CFRP	carbon fibre reinforced plastic
CLT	classical lamination theory
DCB	direct copper bond
DIC	digital image correlation
DPC	direct plated copper
GFRP	glass fibre reinforced plastic
FRAM	ferroelectric random access memory
FE	finite element
FEA	finite element analysis
FEM	finite element modeling
HDPE	high density polyethylene
HTCC	high temperature co-fired ceramics
IC	integrated circuit
ILSS	interlaminar shear strength
LTCC	low temperature co-fired ceramics
MEMS	micro electro-mechanical system
NCF	non-crimp fabric
NDT	non-destructive testing
NDE	non-destructive evaluation
PCB	printed circuit board
PET	polyethylene therephtalate
PMI	polyimide
PVDF	polyvinylidene fluoride
SAW	surface acoustic wave
SEM	scanning electron microscopy
SHM	structural health monitoring
SLS	selective laser sintering
TSSOP	thin-shrink small outline package
VQFN	very thin quad flat non-leaded

SYMBOLS

σ_i	tensile stress in i -direction
σ_i^c	compressive stress in i -direction
τ_{12}	shear stress in ij -plane
Q_{ij}	reduced stiffness coefficient
ϵ_i	strain in i -direction
γ_{ij}	shear deformation in ji -plane
k_i	curvature constant for the middle surface of composite layer in i -direction
k_{12}	curvature constant for the middle surface of composite layer in ij -direction
z	distance from the middle surface of layer
E_1	Young's modulus
G_{12}	shear modulus
ν_{ij}	Poisson ratio
$F_i(\bar{x})$	objective function of optimization
$f_i(\bar{x})$	normalized objective function of optimization
x_i	design parameter
\bar{x}_i	vector of design parameters
w_{max}	maximum deflection
E	energy
C	capacitance
P	power
V	voltage
w_i	i -th weight coefficient
H	height of resin pocket
L	length of resin pocket
α_{max}	maximal angle between resin pocket walls

1. THEORETICAL BACKGROUND

1.1 Composite Materials and Structures

Composite materials have found a wide range of applications due to their unique properties, of which perhaps high specific strength and resistance to fatigue and corrosion are the most valued. Fibre composites are laminated anisotropic materials, in which damage is often not easily detectable. Carbon fibre is the most promising structural composite reinforcement type. It has very high mechanical strength, yet has low density. Besides high specific strength it is corrosion resistant and extremely durable in fatigue loading conditions. This makes carbon fibre appealing for aerospace and automotive structures. The biggest disadvantage of carbon fibre composites is their proneness to catastrophic failure. One of the most famous catastrophic failure incidences occurred in the 1995 America's Cup sailing yacht race, where a yacht named "OneAustralia" snapped in half and sank in the matter of few dozen seconds with the assistance of its heavy keel [4], [5]. For carbon fibre it is critical to predict failure in advance. This introduces the field of structural health monitoring. This field receives a more detailed introduction in the next section.

1.2 Structural Health Monitoring Systems

Today structural health monitoring is a rapidly evolving field. Structural health monitoring is defined by Farrar et al. [6] as a process of implementing a damage identification and characterization strategy for aerospace, civil and mechanical engineering. Damage is defined as a change of a material's or structure's mechanical or physical properties, including the connectivity to boundary conditions, which causes an adverse reduction of the system's general performance.

Without the SHM system usually safety or failure critical structures are maintained using time-based health or condition assessment. For example most aeroplane critical structures have a pre-defined flight hours reserve after which they must be replaced. A structural health monitoring system's main purpose is to replace the time-based method with condition-based life-expectancy assessment. A typical example is a sensor network (e.g strain gauges) that will register unwanted change of structure or material and then will notify the operator of the system of detected damage. Condition based monitoring helps to reduce the probability of failure, especially in life-hazardous applications. Besides that it has the side effect of helping to reduce excessive material usage. Safety factors can be reduced, which in the longer term will benefit the environment.

SHM methods can be categorized under local and global monitoring methods. Local methods detect the damage usually near the source. These methods are very often used in non-destructive testing fields. The main problem with these methods is the requirement for the measuring unit to be near the damage zone. Their benefit is high sensitivity to damage. Global monitoring methods use indirect damage describing characteristics to identify the occurrence of damage. The most used characteristics are stiffness, mass or energy dissipation properties of a system, which will influence the dynamic response of the whole structure.

1.3 Advantages of Embedded Sensors

Surface mounted sensors are susceptible to damage and their protection from environment is often noticeable extra weight increase. Embedding the sensors allows for protection from harmful environmental conditions. It is also the only way for creating an autonomous structure with a smooth, non-irregular surface. An example of strain gauges with noise-proof analogue signal cabling is shown in Figure 1.1. Embedded sensor nodes remove the need for heavily shielded long signal cables, especially if the primary signal processing is done near the sensor. From the image it can be also estimated that such cabling is a noticeable weight-gain to the lightweight composite structure.



Figure 1.1 Strain gauge rosettes mounted on a ship's underwater appendage structure

Aside from cabling the second concern is sensor protection from environmental influences. The most sensitive devices are those which have a mechanical bond with the material in order to register strains. The interfaces between two materials are sensitive to moisture attack. It is known, that moisture attacks the material interface between a sensor body surface and the composite matrix [7-8]. In order to use strain sensing devices in long-term applications the sensors must be well protected from environmental influences. A feasibility study for a marine environment was conducted in 1990 by Green et al. [9]. They concluded that the performance of a strain gauge sensor in a marine environment is strongly dependent of the adhesion quality and weather protection methods used. It was found that if the device is joined correctly with the structure, then it can perform well, reliably, for up to 20 years, depending on application. They also verified that general polymer enclosed strain gauges perform better than weldable strain gauges.

Correct installation and isolation (from outer environment) of gauges needs a careful adhering procedure with specific high quality adhesives. This is a labor intensive procedure. Besides the aforementioned shortcomings extra time is consumed due to the used adhesion material polymerization times.

Embedding sensors inside the structure allows the use of the composite matrix as the environmental isolation material. This reduces the cost of SHM system application

through reduction of different materials usage and also the assembly and material preparation and polymerization times. Additionally the less different materials used, the lower amount of two-material interface areas exist, which are prone to fail due to hygrothermal attacks.

Composite structures are known to take advantage of using different plies with different stiffness characteristics. Usually the heavily loaded layers or plies are hidden underneath the surface to protect them from external damaging punctures or abrasion. Due to differences in stiffness the outer plies strains may not represent precisely the inner plies strains and stresses. This is typical when tensile and bending loads are applied simultaneously on material. The simplified mechanical behavior can be described with classical lamination theory as in [10]. The stress-strain relations in a plane stress state for an orthotropic lamina with numbering index k are described by stress-strain matrices as shown following equation:

$$\begin{bmatrix} \sigma_1 \\ \sigma_2 \\ \tau_{12} \end{bmatrix} = \begin{bmatrix} Q_{11} & Q_{12} & 0 \\ Q_{12} & Q_{22} & 0 \\ 0 & 0 & Q_{66} \end{bmatrix} \begin{bmatrix} \epsilon_1 \\ \epsilon_2 \\ \gamma_{12} \end{bmatrix} + z \begin{bmatrix} k_1 \\ k_2 \\ k_{12} \end{bmatrix}. \quad (1.1)$$

Where the reduced stiffness's Q_{ij} are defined as follows:

$$Q_{11} = \frac{E_1}{1 - \nu_{12}\nu_{21}}, \quad (1.2)$$

$$Q_{22} = \frac{E_2}{1 - \nu_{12}\nu_{21}}, \quad (1.3)$$

$$Q_{12} = \frac{\nu_{12}E_2}{1 - \nu_{12}\nu_{21}} = \frac{\nu_{21}E_1}{1 - \nu_{12}\nu_{21}}, \quad (1.4)$$

$$Q_{66} = G_{12}. \quad (1.5)$$

The equations apply for a single ply. This can be transferred to a random ply with number indication of k . From these laminas a laminate can be assembled. For a multi-ply laminate the following simplifications are made:

- The laminas are bonded together with a virtual bond which has no thickness nor shear deformations.
- The laminate is considered to be a few magnitudes longer in 12 plane compared to the thickness plane 3.
- All the deformation in lamina happens without changing the laminas' surface normal direction. This excludes shear deformations γ_{13} and γ_{23} .

For composite laminate the reduced stiffness coefficients Q_{ij} have different values if the layers are composed of different angled, different weaving pattern or different materials. As a result the difference in elastic modulus values will cause stress distribution to become discrete in a layer-wise direction. It is depicted in Figure 1.2. The representative laminate is composed of four layers, from which two have different

Young's modulus. The bending strain distribution in z-direction (same as direction 3 in previously mentioned equations) is linearly varying. However the stresses in layers are not necessarily distributed linearly, even though the strain variation is linear. Instead typically the stresses are linear piecewise, but at the layer boundaries between layers they are discontinuous.

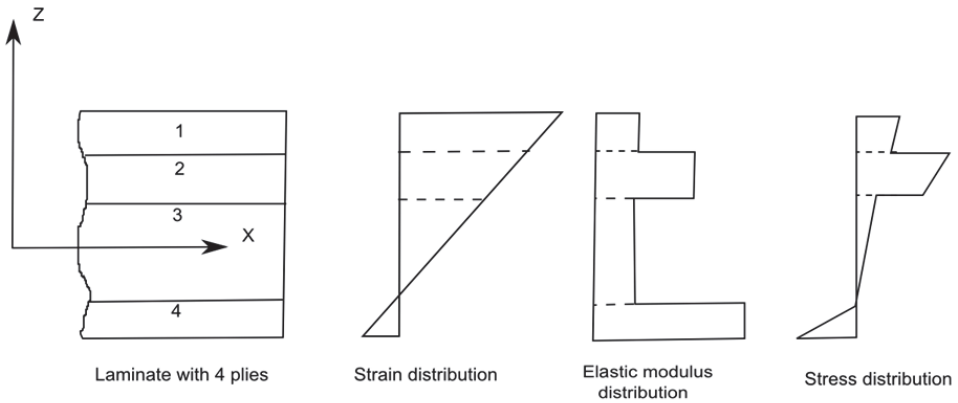


Figure 1.2 Theoretical variation of laminate stresses through thickness

If the strain gauge rosette is placed on the layer, which will not be critically loaded during operation of structure, then it may not detect the catastrophic stress occurrence.

To summarize it is vital and feasible to embed layer stress measuring devices inside the composite laminate instead of surface mounting. The main benefits of this approach are the environmental protection advantages and also the need to detect and quantify the layer stresses directly from the layer under the scope.

1.4 Sensor Size Concerns

Integration of sensors or MEMS devices into fibrous composites is usually achieved by placing the device between the plies of composites during the manufacturing process. The device becomes surrounded by the matrix and the continuous fibres are bent in order to facilitate the embedded device matching with the surroundings. This leads to the increase of interlaminar stresses near the inclusion and a local remissive stress concentrator is created. Besides the weakening of the whole composite structure the stress gradients around the embedded device distort its ability to sense the surrounding environment. Therefore it is necessary to investigate and characterize the mechanical interaction between the embedded device and the host composite structure.

Keeping the sensor very small minimizes perturbations in the normal stress field. The less the foreign object bends the composite fibres out of their normal plane, the stronger the resulting laminate will be. One good example of feasible sensor solution is developed by Mohammed et al. [11]. They developed a high sensitivity MEMS piezoresistive strain microsensor, which has good sensitivity, low power consumption and thermal stability. This all has been achieved at the size of around 10mm times 0.5mm.

1.5 The Influence of Foreign Objectson Mechanical Properties of Composite Material

Embedded foreign objects can be considered to behave similarly to void inclusions. They influence the stiffness and strength of composites negatively as shown by Bowles [12] and Costa [13]. Costa determined that voids in composites may result in severe reductions in matrix-dominated mechanical properties such as interlaminar shear, and compressive and flexural strengths. Quantitative degradation of properties differs strongly depending on the specific material or manufacturing method used. The main contributor to the diversity of degradation is the morphology of voids [14]. Voids are usually hollow gas volumes inside the host structure. Huang and Talreja describe voids as a cutout from the composite material [4]. The voids differ from embedded devices by the fact that embedded devices may not create such high stress concentrations due to their geometry and can have the ability to carry mechanical loading. A controversy might be created by the fact that embedded devices' thermal and moisture expansion coefficients will differ from that of the host materials. This can create extra stresses via expansion mismatch at temperature change. Based on the assumption that voids can be considered as representatives of embedded objects the literature study is conducted. From Liu et al. [15-16] studies it turns out that for $0^\circ/90^\circ$ woven fabric based composites the ILSS reduces around 30% for void concentration of 3% in case of carbon/epoxy laminate.

Composite materials are known to have reduced compression properties compared to isotropic materials. The void content inside the composite material influences the already weaker compression properties further. Hapke et al. [17] investigated the failure of unidirectional carbon-fibre composites with scanning electron microscope. He concluded that the damage mechanism at compression failure is caused by local microscopic fibre kinking and ensuing fibre fracture which leads to a catastrophic event. From his conclusions it can be assumed that foreign inclusion caused macroscopic fibre misalignment is a precondition to enhance fibre kinking proneness.

Czichon [14] has conducted an extensive literature review and research on the void content influence on the properties of composite laminates with different production methods. He summarizes that the influence of void content on the properties is strongly material, laminate and manufacturing method dependent. To conclude this section it can be said that the foreign object inside a laminate has complex interaction with the structure. It is feasible to determine the characteristic properties of a composite experimentally for specific material and embedded device combination.

1.6 Physical Interfacing of Sensor Node Body and Composite Matrix

Composite materials in wind turbine and marine applications work in harsh outer environment. Unlike aerospace structures they are not stored in protective hangars to allow recovering from moisture attacks or icing. Moisture influences composites negatively in multiple aspects.

Tsenoglou et al. [18] investigated the water absorption properties of polyester resin based glass fibre laminate. They concluded that moisture diffuses along the microchannels surrounding the fibres. The moisture sorption and drying cycles cause the size of the microchannels' volume to increase, which leads to an almost logarithmic increase of diameter of channels.

Zafar et al. [19] proposes that fibre-resin interfacial properties are decreased due to chemical degradation and mechanical degradation. Chemical degradation is the result of hydrolysis of the bonds at the interface. It is a function of the environment temperature and pH value. Mechanical degradation is the result of matrix swelling causing stresses large enough to pull the matrix apart from the fibre. Amer et al. [20] estimated that swelling is the main reason for interfacial damage. The complex mechanical radial tensile stress state pulls the matrix off the fibres.

Zafar et al. [19] determined experimentally that absorbed water destroys the crosslinks inside the epoxy structure and by doing that segments rigidity. Pure epoxy resin lost its properties 15%–18% on average after being conditioned 40 and 300 days.

It can be concluded that two material adhesion suffers severely under moisture attack.

1.7 Methodology for Development of Smart Composite

As pointed out above the embedded sensors have several advantages with respect to surface mounted sensors:

- sensors are protected from adverse environmental conditions,
- possibility to create an autonomous structure with a smooth surface finish

Besides the aforementioned advantages, embedding the electronics inside the host laminate has the benefit of reducing the signal noise issues related to long cabling and enables the possibility to commit local primary signal processing. Thus, it is reasonable to proceed with design of smart composites with embedded electronic components and to consider surface mounted components based structures as an alternative solution for particular situations.

However, based on literature overview and discussion given in sections 1.1–1.7 it can be concluded that there are a number of key factors influencing structural health of the smart composite with embedded electronics:

- stiffness characteristics of the structure,
- strength characteristic (max stress, max strain, failure index, etc.),
- acquired information characteristic (values of the acceleration, stress, strain, humidity, etc.)
- energy consumption characteristic.

In the current study an attempt is made to consider the effects of all key factors in design of smart composite. For that reason the following approach is proposed:

- The design problem of smart composite can be formulated as a multicriteria optimization problem utilizing above mentioned key factors as objectives and including the cost as an additional objective (see section 1.1):
 - The stiffness of the smart structure is subjected to maximization. The characteristics considered involve the elasticity tensor components. Instead of maximizing components of the elasticity tensor certain simplification was made –the strain energy density has been subjected to minimization (providing stiff structure).
 - The strength of the smart structure is subjected to maximization. The considered characteristics –maximum stress and maximum strain, both

are maximized. An alternative possible approach is to minimize the maximum failure index (calculated for each element).

- The energy consumption has been subjected to minimization. For smart composites with embedded systems energy consumption is especially important, since powering or recharging is a more complicated task. Reduction in energy use is provided by careful design of electronic components, optimizing data exchange and management.
 - The acquired information capacity is subjected to maximization. However qualitative information capacity is meant here, not quantitative. The information can be filtered in sensor nodes and only selected information should be stored and sent during data exchange sessions. The characteristics included are acceleration, stress, strain and humidity.
 - The cost is subjected to minimization.
- The solution procedure can be decomposed into subtasks, which have a hierarchical structure and can be solved iteratively
Obviously, the posed multicriteria optimization problem contains conflicting objectives, several technological, geometrical, etc. constraints, discrete variables, local extremes and its solution is complicated. The solution procedure can be decomposed in the following subtasks: design of host structure (stiffness, strength), design of embedded electronics (data acquirement, shape, size), design of embedding process.
 - Design of smart composite structure includes iterative repetition of above mentioned subtasks.
 - An analysis of the usability of resistance strain gauges in local sensor nodes should be performed.
 - Possible loss of structural integrity of composite structure caused by the inclusion of foreign objects in the material should be estimated.

2. DESIGN OF BASE COMPOSITE MATERIAL

In the following an overview of *Paper I* (see Appendix II for full paper) results is given.

2.1 Introduction

An example sandwich material design study was conducted with the purpose to optimize its price performance.

The multicriteria optimization problem has been formulated and solved by applying multicriteria analysis techniques [21-24] and genetic algorithms [25-28].

The main goal of the current study was to develop a new composite material with optimal mechanical properties. The optimality criterion targets are mechanical strength and cost.

2.2 Experimental Testing

The mechanical properties of experimentally manufactured sandwich composite materials were tested. The sandwich composite panels were tested in 4-point bending conditions according to ASTM C393/C393M. Three different core materials were tested. The principal scheme of the 4-point bending test is described in Figure 2.1, where: P is the load, S is the distance between supports, L is the span. The span of the lower supports was 560 mm and upper supports 100 mm.

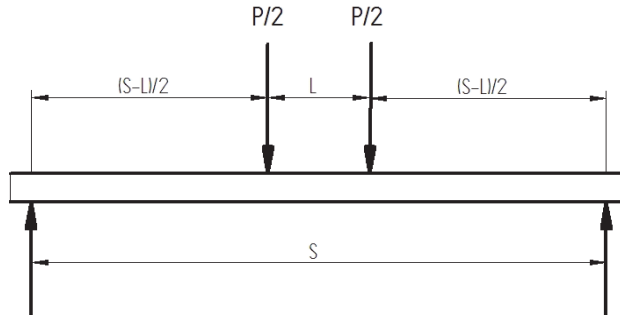


Figure 2.1 Loading scheme in 4-point bending

2.3 Finite element model of sandwich panel

Finite element analysis subjected to 4-point bending was conducted with ANSYS APDL v12.1 software. A plane strain 2D assumption was used. A linear orthotropic material model was used to define laminate properties. A linear isotropic material model was used to define core properties (defined by elastic modulus E and Poisson's ratio ν).

For FEA model validation the results of 4-point bending tests and virtual testing have to be compared. As it follows from Table 2.1 for the sandwich panels with PET and PMI foam the deflection rates obtained by real and virtual tests are quite similar differentiating only by 3 % and 6 %, as the shear modulus of these foams (see Table 2.1) are in the same range from 19 MPa to 20 MPa. Regarding the sandwich panel with HDPE foam the deflection rate obtained by real testing is differing almost 40 % from the virtual result.

This can be explained by relatively low shear modulus (11 MPa) and buckling with plastic deformation of the tested panel.

Table 2.1 Comparison of the real and virtual 4-point bending test results

Type of Core material	w_{max} by testing, mm	w_{max} by FEA, mm	τ by FEA,MPa
PET	34.2	32.0	0.97
HDPE	69.9	41.5	0.94
PMI	30.0	30.9	0.94

The obtained FEA analysis results were used for optimal design of the sandwich panel. Three core materials from eleven were physically tested, other eight were numerically tested.

2.4 Optimal Design of Sandwich Panel

In order to improve mechanical properties of the sandwich structure design optimization has been performed. The aim was to design the sandwich structure with maximum stiffness/strength properties while keeping expenses minimal. Behaviour of the different strength characteristics of the sandwich structure has been analyzed and the maximum stress was selected as an optimality criterion i.e. the aim was to find out the configuration of the sandwich structure providing the highest failure load. Certain similarity in behaviour of the stiffness/strength characteristics has been observed (proportional relations). An alternative concurrent optimality criterion was the cost of the sandwich structure.

Thus, the multicriteria optimization problem considered can be formulated as

$$F_1(\bar{x}) = \sigma_{\max} \rightarrow \max, F_2(\bar{x}) = Cost \rightarrow \min, \quad (2.1)$$

subjected to linear constraints applied to the design variables vector \bar{x}

$$x_i \leq x_i^*, \quad -x_i \leq x_i^*, \quad i = 1, \dots, n, \quad (2.2)$$

and non-linear constraints applied to the maximum deflection of the sandwich w_{\max} , maximum stresses of the each layer σ_k as

$$w_{\max}(\bar{x}) \leq w^*, \quad (2.3)$$

$$\sigma_k(\bar{x}) \leq \sigma_k^*. \quad (2.4)$$

In 2.2–2.4, the indexes * refer to the upper limit value of the corresponding variable. The objectives 2.1 are normalized by taking use the following non-dimensional functions

$$f_1(\bar{x}) = \frac{\max F_1(\bar{x}) - F_1(\bar{x})}{\max F_1(\bar{x}) - \min F_1(\bar{x})}, \quad (2.5)$$

$$f_2(\bar{x}) = \frac{F_2(\bar{x}) - \min F_2(\bar{x})}{\max F_2(\bar{x}) - \min F_2(\bar{x})}. \quad (2.6)$$

Obviously, both concurrent objectives $f_1(\bar{x})$ and $f_2(\bar{x})$ are subjected to minimization and the Pareto optimality concept can be applied.

2.4.1 Pareto Frontier

Repetitive evaluation of the objective function $f_1(\bar{x})$ and nonlinear constraints 2.3 and 2.4 during the optimization procedure is time consuming. For that reason, the FEA has been performed for a fixed set of design variables and on the basis of obtained numerical results the response surface has been constructed (most commonly used technique to reduce the cost of the computational analysis and /or experimental tests). In the current study the artificial neural network (ANN) has been employed for response surface modeling. The surface constructed by the use of ANN does not normally contain the given response values (similarity with least-squares method in this respect). An approach proposed is based on the use of the MATLAB neural network toolbox (two layer network with one hidden layer). The Pareto front of the maximum stress and cost of the sandwich structure is given in Figure 2.2. It is composed of 3 separate curves. The reason for gaps between curves is an un-continuous or discrete option for core materials. The gaps are locations, where there is no physical core material option available.

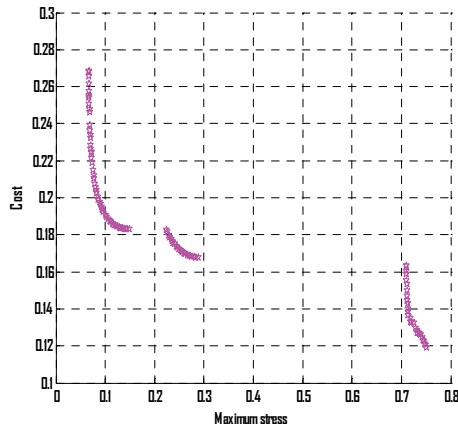


Figure 2.2 Maximum stress versus cost of the sandwich structure

First note that the minimum values of the objective function $f_1(\bar{x})$ in the Pareto front correspond to maximum values of the original stress function $F_1(\bar{x})$ (see formulas 2.1 and 2.5). The Pareto front depicted in Figure 2.2 contains discontinuities and is made up from three parts corresponding to sandwich structures with different values of maximum stress and cost. Obviously, the Pareto front can be made less gradual by design of the neural network model, but this is not the target desired. The main aim is to provide as much information as possible for decision making i. e. for selection of an optimal point on the Pareto front. Points before a sudden rise of the cost function seem most appropriate. However, all points on the Pareto front are optimal (Pareto optimality) and a final decision depends on the particular case.

2.5 Conclusions

Optimal design of the light-weight sandwich panel has been performed. Different combinations of the core material and layer thicknesses are considered. The study involved experimental investigation and numerical simulation for determining

mechanical properties of the layer materials of the sandwich structure. In order to reduce computational time the metamodeling technique has been employed (ANN). Finally, relying upon the obtained response surface the Pareto optimality concept is applied and optimal solutions are determined. It can be concluded that:

- the solution appears more sensitive with respect to core material selection than core layer thickness (it was assumed that the total thickness on the sandwich structure remains unchanged, i.e. core thickness can decrease with increasing facing layers thickness);
- the use of certain expensive core materials like PMI leads to a sudden increase in cost, but does not provide significant improvement of the mechanical properties; thus in most cases use of such core materials is not reasonable;
- the sensitivity of the solution function with respect to design variables is times higher in points neighbouring the discontinuity points of the Pareto front.

The Pareto optimality chart describes the price performance of the sandwich structure in this specific application. It can be seen, that the cost response is non-linear. Using structural health monitoring in order to reduce the reserve factors can justify the cost of the SHM system and also lead to general material consumption reduction. This also leads to environmental saving benefits.

3. DESIGN OF ELECTRONIC COMPONENTS

In this chapter the design of electronic components is studied in the point of view of:

- information acquiring capabilities,
- embedding possibilities of components in composite structure.

3.1 Electronics Miniaturization Possibilities

Embedded device dimensions are dominated mainly by the size of integrated electronics. Printed circuit boards and microchips and components are all options for size reduction. It was decided at first to focus on available commonly used electronic devices' casings. Economical methods that could be used without interfering with the chip design's fundamental technologies are the following:

- Selection of minimum size chips casing. This means searching for the smallest available casing design that is easy to assemble on to the system.
- Bare integrated circuits. This design is simply a semiconductor device, which has no moulded protective casing.
- Flexible substrate electronics[29].
- Ceramic substrate technology.

3.1.1 Small Size Chips and Bare Integrated Electronics

Most IC's have multiple packaging options. The core of the SHM system under development is a Texas Instruments produced FRAM based ultra-low power consumption microcontroller MSP430FR5379. The easiest and cheapest way to decrease the size of electronics is simply selecting components packaging that has the smallest dimensions. For the available MSP430FR5379 integrated circuit it means choosing between TSSOP and VQFN type packaging. Their designs are depicted in Figure 3.1 and Figure 3.2. From the longitudinal and height dimension comparisons it can be concluded that the size reduction of selecting VQFN type packaging reduced the dimensions of this controller simply by approximately one third. This is an economic decision to reduce the size of the electronics of the prototype.

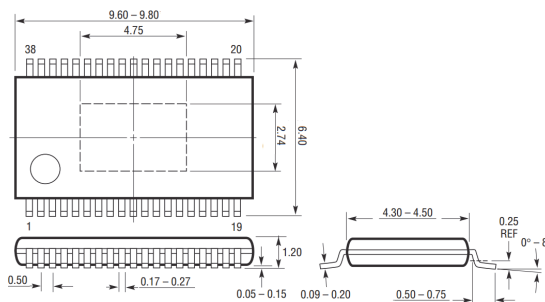


Figure 3.1 TSSOP packaging of MSP430FR5379 microcontroller

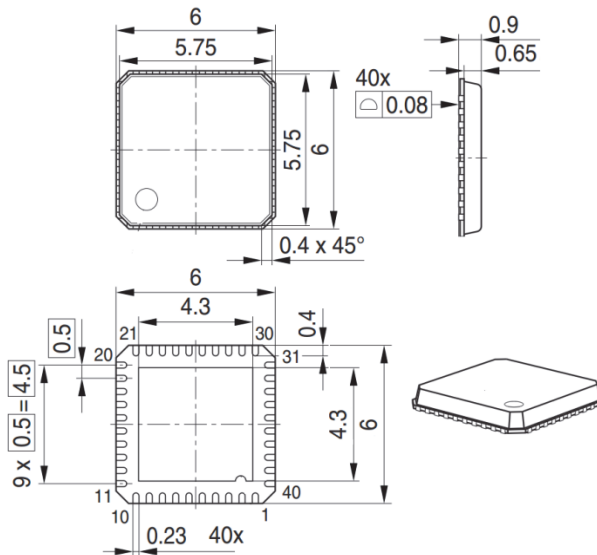


Figure 3.2 VQFN type packaging of MSP430FR5379 microcontroller

The main limit to reducing the chip size is its manufacturability. The smaller devices get, the more difficult it is to reliably assemble them on a PCB.

Bare integrated circuits (also known as *bare die*) are used in the author's first study of experimental embedment of electronics. Semiconductor devices are cut out from semiconductor wafers. The small parts on which a single integrated circuit lies are called dies. See Figure 3.3 for further explanation. Integrated circuit's bare die is the smallest possible conventional electronics option, which does not need the alteration of basic semiconductor design. Modifying or redesigning the silicon wafer cost is approximately twice as costly as simple PCB based electronics development [30].

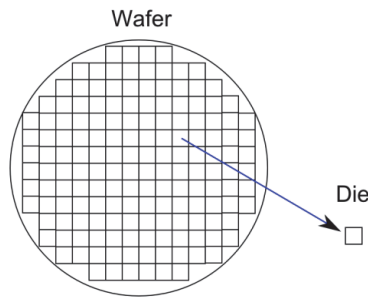


Figure 3.3 Wafer is composed of dies

A bare IC design is used sometimes, when there is a need for high packaging density of electronics. The advantages of bare dice technology is well summarized by Al-Sarawi et al. [31]. The most important factors to point out in the context of embedded devices are compactness, noise resistance, power consumption and speed. Removing the discrete housings from microchips reduced the size of integrated circuits from between 5 to approximately 20 times. Noise resistance is increased based on the reduction of interconnection lengths. This reduces crosstalk noise, reflection noise and

electromagnetic interference. Reduction of noise leads to increased reliability. Power consumption is reduced due to reduction or interconnect parasitic capacitance C . An electronic system dissipates energy according to the equation[31]:

$$E = CV^2, \quad (4.1)$$

where V is the voltage swings along the interconnect.

The power consumption P process of energy dissipation is a function of voltage swings across the interconnections and f is the frequency of swings. The equation is as follows:

$$P = fCV^2 \quad (4.2)$$

The speed gain is achieved through taking advantage of reduced energy dissipation: lower parasitic capacitance enables increase of the clock frequency of integrated circuits without extra power consumption.

The main disadvantage of a bare integrated circuit is its vulnerability. The ceramics are very brittle and conductor junctions are extremely thin. They are generally too fragile to be handled by a human being. Therefore a prerequisite for their usage are automated assembly and manufacturing methods for the structure.

3.1.2 Flexible Substrate Technology

Flexible substrate electronics are a high potential material choice for embedded devices. The biggest advantage of flexible substrate electronics is their high strain resistance. Lacour et al. [32] developed an elastomeric substrate with in-built compressive stress pretension which creates wavy buckled conductors. This material could be stretched to 22% tensile strain before its gold conductors fractured. This value exceeds typical structural epoxy resin maximum strain value by around fivetimes. Kim et al. [33] review the current state of the art in making inorganic high rigidity materials flexible for flexible electronics. Different authors use different geometrical patterning to make rigid semiconductor materials like Si, GaAs, GaN etc. flexible. Various physical effects are used: buckling strategy, stretchable metal interconnects, stretchable strain isolated systems etc.

Besides inorganic materials an emerging field is so-called organic and also printed nanocomposite thin film transistors. An example of the latter is developed by Hsieh et al. [34]. Hsieh develops carbon nanotubes enriched polythiophene active transistor channel, which is produced by ink-jet printing. This technology is relatively cheap and additionally has the ability to work under a high strain environment.

Under the flexible substrate technology are also characterized multifunctional structural batteries. Liu et al. [35] developed a deformable lithium ion battery, which has material properties tuneable from elastic to rigid. The battery's design is based on polyvinylidene fluoride (PVDF) matrix carbon fibre composites. It achieved modest energy density (35Wh/kg) while being able to withstand tensile strain up to 10%. This battery can be successfully embedded inside a smart composite structure. The current state of the art is well documented in [36] and [37].

The latest developments and trends in thin film flexible electronics are reviewed by Nathan et al. in [38]. Its biggest strength is its high variety of application possibilities. The examples are from energy harvesting, energy storing (super capacitors, flexible batteries) to novel sensor types (strain tuneable antennas etc.). Flexible substrate technology is closely related to development of nanomaterials. Flexible substrate technology is perhaps the only technology from this paragraph's technologies, which is truly able to cooperate with the high strains of composite structures.

3.1.3 Ceramic Substrate Technology

Under ceramic substrate technology there are categorized multiple different manufacturing methods. Among others the most versatile are direct copper bond (DCB), direct plated copper (DPC), thick film substrates and thin film substrates. Ceramic substrate technology based electronics are generally at least of a magnitude more expensive than simple PCB based electronics according to Bethold [30]. Nevertheless they have certain advantages which make them desirable for fully embedded devices.

Ceramic substrate technology allows for high miniaturization. The ceramic board can be produced with thicknesses starting from 0.254mm [39]. The most economical thickness is 0.635mm [39]. Conductive copper, silver or gold layers can have thicknesses from 5 μ m to 20 μ m and width around 50 μ m [40]. An example power electronics module is depicted in Figure 3.4.

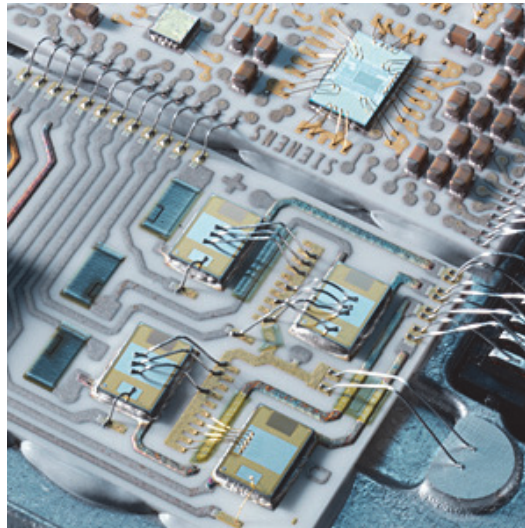


Figure 3.4 Hybrid circuit composed of silicone semiconductors printed on a ceramic board[30]

According to Bechtold [30] LTCC and HTCC technologies can guarantee a life expectancy of more than 20 years. This is feasible since the electronics cannot be removed after the host material has been finalized. Predicted PCB life expectancy is, by comparison, around 3 years.

The thermal expansion coefficients are small, around 6 μ m/m/K. This fact makes ceramic substrate technology thermal expansion more compatible to carbon fibre polymer composites, which also have very small thermal expansion coefficients. One relevant property is the high difference of the thermal coefficient of expansion with a PCB. It is a magnitude lower compared to PCB technology. Composites are sensitive to

thickness direction strains. Avoiding extra strains from thermal loading in that direction makes the smart composite structure more robust.

Perhaps the most important characteristic of ceramic substrate technology based devices is their mechanical strength. LTCC technology has flexural strength around 200MPa and HTCC devices have it around 350MPa [30]. This allows them to withstand, to at least some extent, mechanical loading and also shock-loading. These stress levels are close to the permitted stresses for GFRP laminates.

The ceramic substrate devices have 0% water absorption property. Ceramic substrate devices are therefore hydrophobic. This is a strong advantage in moisture filled environments.

3.2 Low Cost Strain Sensor Experimental Testing

This section is a short summary of *Paper IV* (see Appendix II for full paper).

3.2.1 Introduction

The research topic of this article is the fatigue testing of fully embedded semiconductor strain gauges (see Figure 3.5) in order to check their potential in embedded structural health monitoring system applications. In the testing procedure two different composite materials are used. Different matrixes were used for specimen manufacturing: vinyl ester and epoxy resins. Epoxy resins have very high adhesion properties while vinyl esters are widely used medium cost polymers for wind turbine and seaborne industries.

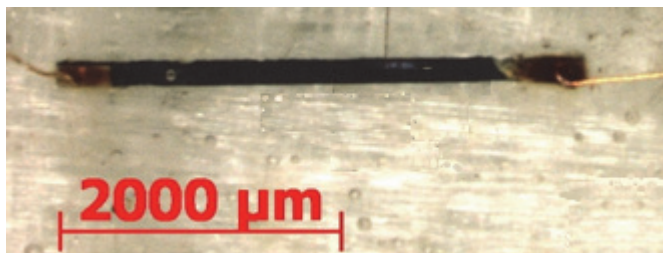


Figure 3.5 Silicon semiconductor strain gauge embedded in glass fiber laminate

Strain sensitive characteristic dependability from local defects has often been utilized to identify damage in structures [41]. Semiconductor strain gauges have a good potential for embedded structural health monitoring applications. The sensors usually have a rectangular thin bar shape, with thickness around tenths of a millimetre. The shape similarity to fibres and material similarity to glass fibres make this sensor appealing to composite SHM. The proportions of the sensor are close to the typical fibre: the length dimension is magnitudes higher than width or thickness.

Semiconductor strain gauges have high piezoresistivity. The resistance change occurs in all conditions of static and dynamic strain. The gauge factor for semiconductor strain gauges are 50- 60 times higher compared to metallic foil gauges [42]. This removes the necessity to use high gain voltage amplifiers associated with metallic strain gauges.

The main advantage of a semiconductor strain gauge is its high fatigue life. Since the gauges are single-crystal elements, they have no measurable hysteresis or creep [42]. This makes them attractive for long-term installations or for use in unique transducer

applications.

Distributed wireless sensor node networks are good examples of where to apply semiconductor strain gauges [43]. Nodes are able to measure the temperature locally near the strain sensors. This allows compensation of the non-linear behaviour of the strain sensor.

Hygrothermal conditioning is used to imitate the real application conditions. It is known, that moisture attacks the material interface between the semiconductor and the matrix [44], [45]. Vinyl ester has a magnitude lower interfacial strength than epoxy. It is also more susceptible to damage caused by humidity [45].

3.2.2 Method

The performance of embedded semiconductor strain gauges was estimated using fatigue testing similar to the ASTM E1949 standard. This standard describes the experimental measurement procedure of the fatigue performance of metallic foil resistance strain gauges. The shape of the specimen was developed similarly to ASTM E251 standard. A cantilever constant stress body with linearly decreasing cross-section was developed based on a requirement to maximize the uniformity of longitudinal strain field distributions. The cyclical load to be applied had $R = -1$ fatigue ratio value. The strains were generated by the use of high stiffness machine tool with crank mechanism. Principal schematic of loading is depicted on Figure 3.7. This mechanism could generate stroke radius between 10 mm to 40mm.

The analytical calculation was numerically verified with ANSYS Workbench V14.0. The used body was generated as shell-type geometry and orthotropic material properties were determined. First results showed that the free edge shear stresses concentration and the bolt hole structure at the free end cause perturbations in the uniformity of laminate surface major strain values. A response surface was created in the ANSYS Workbench Design of Experiments module to find a sufficiently uniform stress field. The longitudinal strain gradients values difference minimization was set as a design criterion. The optimal shape of laminate was searched in the near region of the preliminary designed laminate. An example of the final design of the geometry is depicted in Figure 3.6.



Figure 3.6 Vinyl ester specimen during wire soldering process

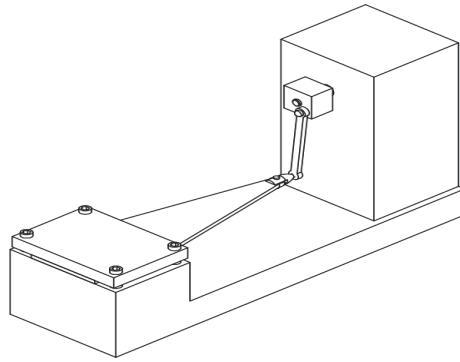


Figure 3.7 Loading method with machine tool and crank

3.2.3 Results

The fabrication process damaged most of the sensors. From 20 sensors only 7 survived to the fatigue testing stage. After the environmental conditioning the vinylester type specimens copper extension wires laminated under the first layer were severely corroded. Therefore it is concluded that at this salinity level direct seawater access through sufficient cracking near the sensors will damage the electronics through corrosion. Also the strain sensor polymer contact adhesive had a darkening change of colour.

The fatigue life of the sensors is summarized on Figure 3.8. It is interesting to note that the sensors did not have any sensitivity declination or hypersensitivity occurrence until failure. Also the temperature increase due to mechanical strains was negligible. The temperature curves were constant and had no correlation with change of excitation speed. The average environmental temperature was 26.6°C.

It is obvious that despite the low amount of sensors the fatigue life of sensors is severely shortened with environmental conditioning. Due to limited amount of data from fatigue testing no statistical numerical conclusions can be drawn, yet the following conclusions can be made as qualitative:

- Epoxy resin specimen fatigue performance is difficult to analyze since the first virgin structure loading was not progressively conducted. From the epoxy resin fatigue results can be concluded that the breakdown strain value will be decreased 56% (from 0.22%-0.26% to 0.06%-0.15%).
- From vinylester testing results it is difficult to estimate the sensor strength reduction values because the damaged specimen had only one operational sensor left. Nevertheless it is evident that is decreased on the scale of 70% (from 0,17%-0.26% to 0.065%).

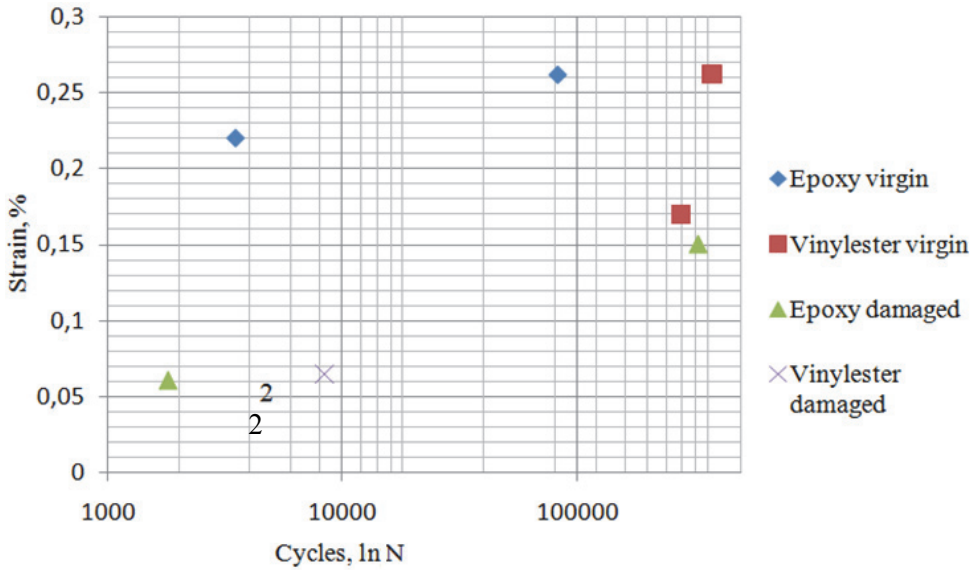


Figure 3.8 Sensors fatigue breakdown

The breakdown of sensors is probably caused by the separation of one contact from the surface of the sensor. This is estimated based on the fact that the sensors stopped working normally in tension mode, but restored electrical circuit continuity in compression mode (see Figure 3.9).

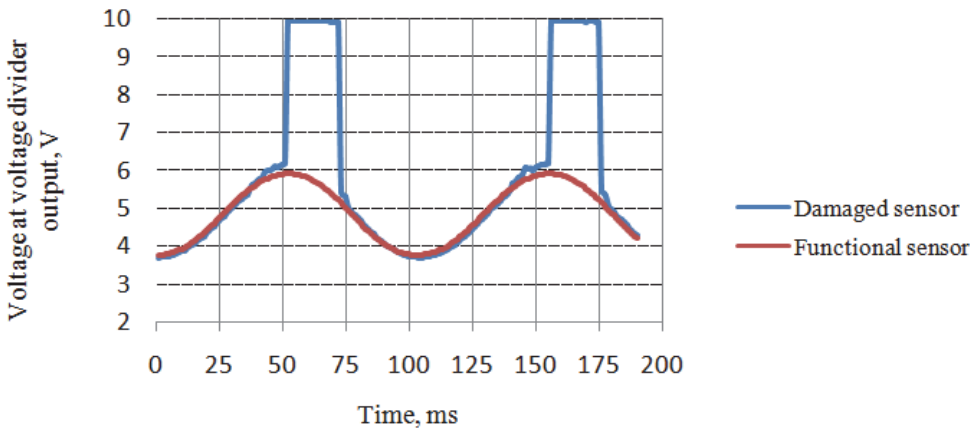


Figure 3.9 Sinus signal shape change due to loss of electrical contact(matched from two measurements)

The breakdown in most cases did not start as an abrupt change, instead the shape of the sine curve at the peak strain values lost its smoothness at first(see Figure 3.10) and progressively the shape of the sine function was totally lost.

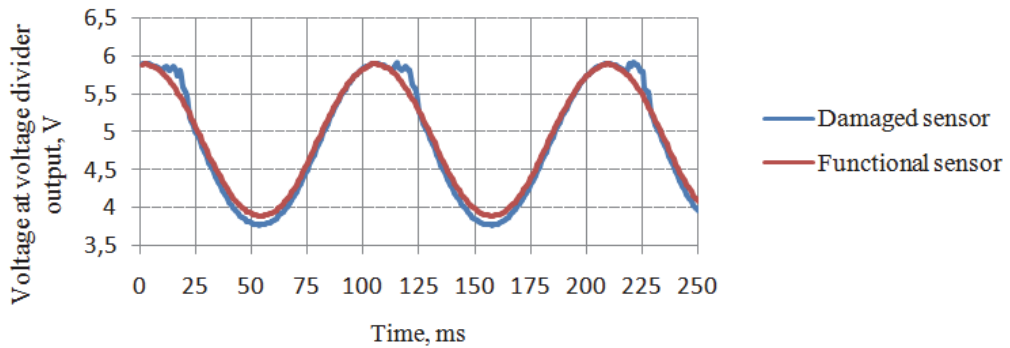


Figure 3.10 Abruption of sine function continuity – the first sign of sensor failure

3.2.4 Summary and Outlook for the Strain Gauge

Fully embedded semiconductor strain gauge testing revealed that the surrounding composite material matrix phase reduces the sensor strength appreciably. Environmental aging damages the sensor thoroughcorrosion and also significantly reduces sensor's fatigue performance. It is critical to protect sensors from moisture attack, especially in the area of junction crystal-joint. The weakest link seems to be the electrical junction contact point to the silicon plate. The strains in these regions should be relieved by some stress relieving geometrical solution. Aside from reduced strength properties the semiconductor strain gauges worked fairly well: no noticeable zero point drift, increased sensitivity or other anomaly was detected before the first signs of total failure. The used copper wires suffered severely from environmental aging. Therefore it is suggested to use extra caution by environmental insulation of wiring. It is useful to perhaps use more corrosion resistant wire material like silver alloys for long-term applications. Using silicon strain gauges seems to be a good solution for detecting strains: the gauges have strong signal output, which is easily measureable using a simple voltage divider.

4. DESIGN OF SMART COMPOSITE

This section is composed of three sub-sections. Firstly a summary of *Papers II* and *III* is given. Then the content of *Paper V* is summarized. Finally a development based on the content of *Paper VI* is documented starting from paragraph 4.15. There the DIC scanner results are analyzed and a finite element model is developed and validated.

4.1 First Attempt of Full Embedment

A case study was conducted in order to determine the possibility to embed naked microelectronics containing printed circuit boards into composite materials. Experimental study is concentrated on manufacturing, testing and examination of the smart composite structure obtained by embedding complex geometry of a naked electronics circuit inside a carbon fibre composite. The base material was woven carbon fibre prepreg.

A printed circuit board (PCB) with low thickness and bare die microchips was chosen for the electronics placeholder. The PCB is depicted in Figure 4.1 on the left. The height of the board was 0,6mm. The thickness with at the thickest point of the PCB was 2.45mm. The PCB was 22mm long and 15mm wide.

Three configurations of PCBs were considered. They are depicted in Figure 4.1 on the right. The PCB was placed longitudinally and transversely to the loading direction for tensile and compression testing. The printed circuit boards were placed in three configurations: longitudinally, transversely and tilted at an angle of 45°. The different angle of sensor placement was chosen in order to simulate the compatibility of node orientation with possible sensors that might be aligned in shear fibre locations.

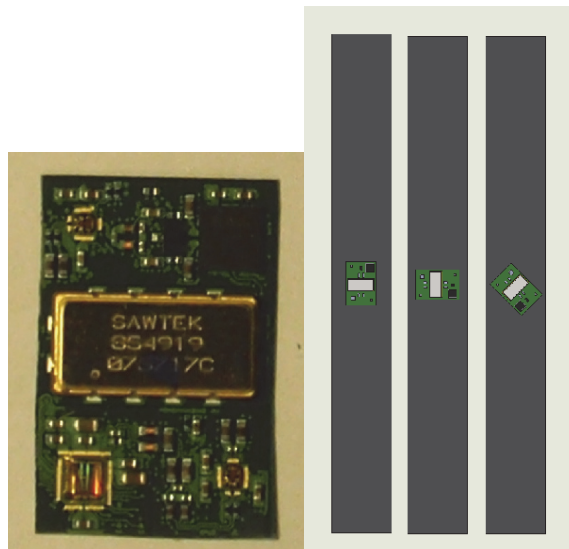


Figure 4.1 Appearance of the electronic circuit on the left and the orientation of the circuit inside the specimens on the right

Chips were placed on the neutral axis. The material was fabricated on a glass plate to imitate a production mould that ensures a smooth continuous surface on one side. This

formed a structure that has asymmetry in the z-direction and it can be concluded that near the foreign object a resin-rich zone is formed (analogical results are obtained in[46]).

The tensile and compressive testing specimens failed similarly for the whole test lot: through the gauge zone occurred a delamination crack which was followed by a lateral crack on the curved surface side of the specimen. Only one specimen from tensile testing had a pure delamination failure. Also in case of compressive specimens one specimen failed only through a pure lateral crack. The shear specimens did not show visually identifiable failure modes. The results from mechanical testing are summarized in Table 2 of *Paper II*. The strength properties decreased on average by 14.9%. The highest reduction occurred in compressive strength properties. The compressive strength decreased by 32.6%, tensile strength by 14.7% and shear strength by 3.3%, respectively. It is interesting to note that the maximum compressive strain and tensile strain increased by 28.8% and 35.9%, respectively.

4.2 Examination of Specimens After Testing

The most intact specimens were chosen as suitable to examine the internals of the specimens after their failure. In all cases the failure cracks started from resin rich pockets at the edges of the circuit boards. Example specimens are depicted in Figure 4.2 and in Figure 4.3.



Figure 4.2 Tensile specimens after delamination failure

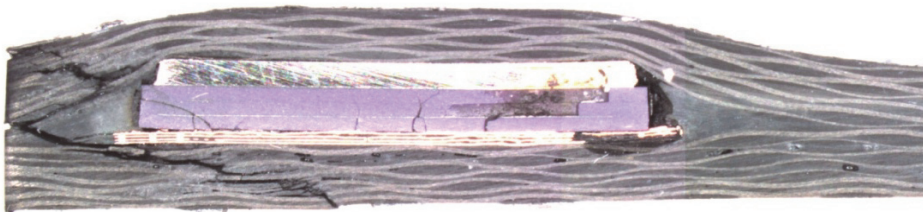


Figure 4.3 Compression testing specimens after crushing type failure and after delamination type failure

The specimens of shear testing were deformed to a shear strain value of 5%. The specimens did not show any signs of mechanical failure although the electronics had a large amount of fractures in their structures.

It should be noted that the electronics have large amount of cracks in the components. Examination of compression testing specimens shows that the printed circuit board has buckled. It is clearly distinguishable by the buckled copper layers that lie inside the PCB. The primary source of failure of electronics functionality is the micro-cracking of soldered junctions (or lead-free adhered junctions) as is stated in[47]. Thus, it can be

concluded that the circuit in real application context would have been destroyed long before the detected PCB and semiconductor breakdown.

4.3 Finite Element Analysis Model and Validation

In this section the FEA model is introduced and validated. The obtained results are discussed. A 2D plane stress finite element model was developed. The models strain information was compared with DIC scanning results.

Two different geometries are simulated in ANSYS V14.0 software. First is the tensile/compression specimen with transversal orientation and second with longitudinal orientation, respectively. The CAD geometry was directly derived from microscope images. The geometry of the simulation model is depicted in Figure 4.4.

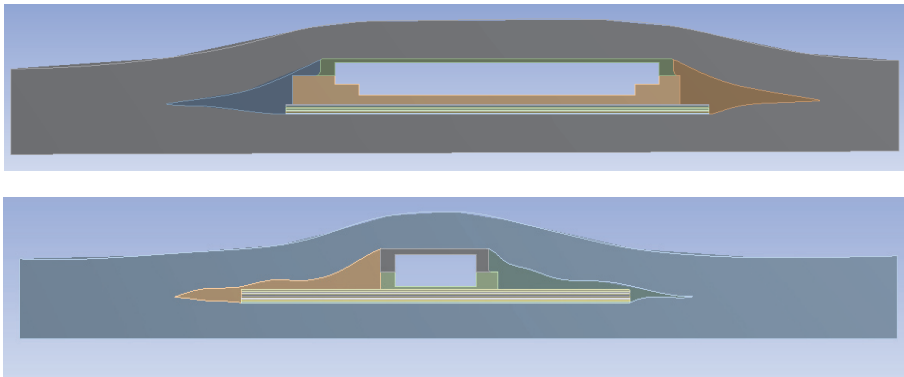


Figure 4.4 Geometry used for simulation

Both structures were analyzed with a finite element method in tension and compression. Structures were loaded to the tensile and compressive limits. The stress distribution was evaluated through the use of von Mises stress and von Mises stress based factor of safety values. Tensile loading condition for von Mises stress distribution in the cross-section of the specimens is shown in Figure 4.5. The factor of safety distribution among the various materials is shown in Figure 4.6.

The most critical zone in both specimen types is at the edges of the resin-rich pockets. SAW filter and resin interface have the highest stress concentration.

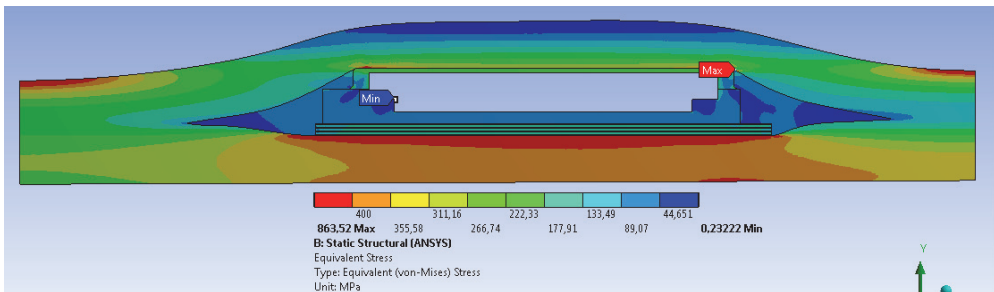


Figure 4.5 Von Mises stress values in the cross-section of tensile specimen

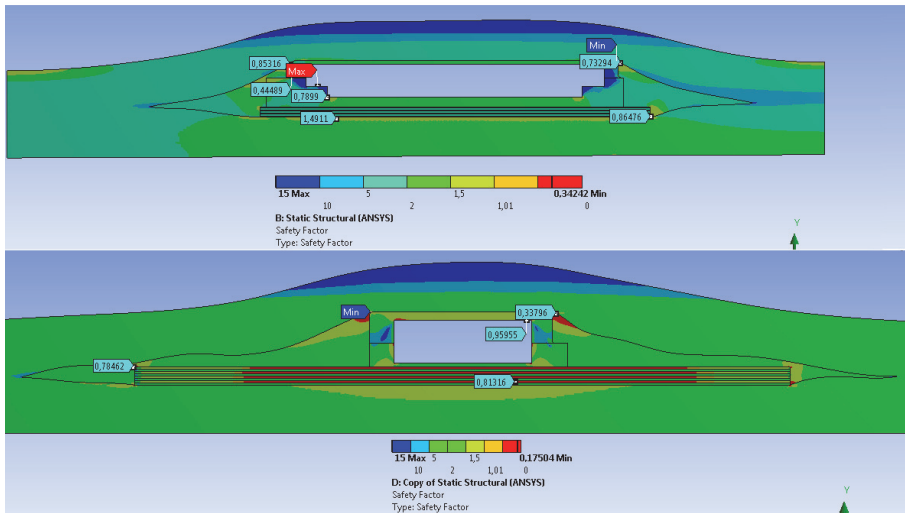


Figure 4.6 Factor of safety values in the cross-section of tensile specimens

Compression loading simulation results are depicted in Figure 4.7 and Figure 4.8. The simulation gives an overall impression that the most critical regions are resin pockets at the end of a foreign object and also high modulus materials, especially steel, quartz or copper (see in Figure 4.6 and Figure 4.8 factor of safety based contour charts).

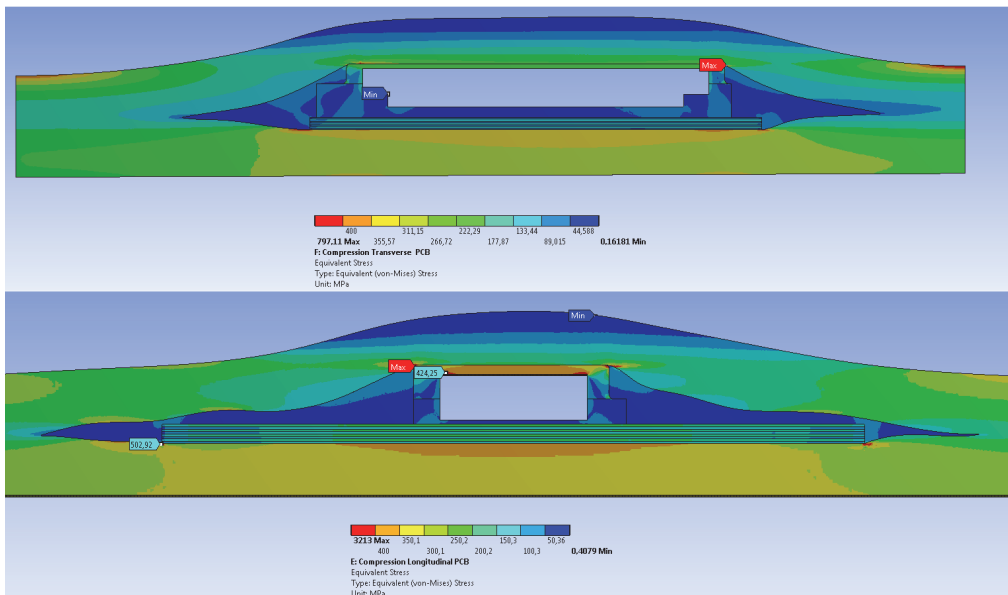


Figure 4.7 Von Mises stress values in the cross-section of compression specimens

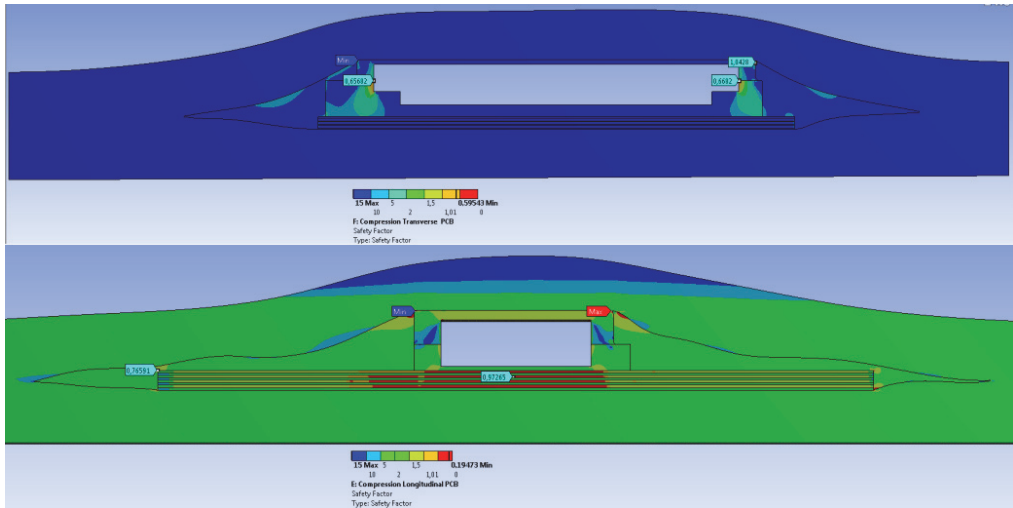


Figure 4.8 Factor of safety values in the cross-section of compression specimens

The finite element analysis model was validated through comparison with the strains occurring on the surface of real specimens. Comparison was made for tensile and also compression testing specimens. The measurements were taken from the middle of the specimen around the circuit. The specimens with embedded electronics were monitored by the DIC scanner during their loading to failure.

Figure 4.9 depicts snapshots of tensile strain field distribution surrounding the foreign object in case of tensile loading condition. The compressive strain distribution is shown in Figure 4.7 and 4.8. For numerical comparison with FE model strain values were extracted from the middle of the specimen. The sectioning surfaces are visible in Figure 4.9 and Figure 4.10 as the black dotted lines.

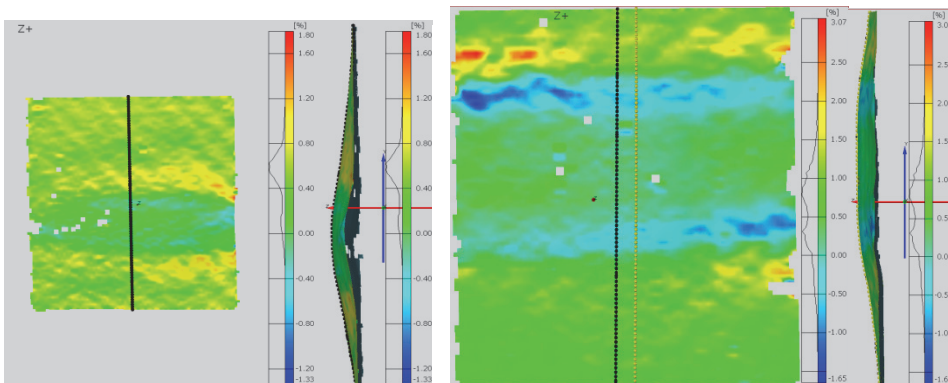


Figure 4.9 Tensile strain distribution on the surface of longitudinally placed PCB specimen at 359MPa tensile stress on the left and transversely placed at 353MPa on the right

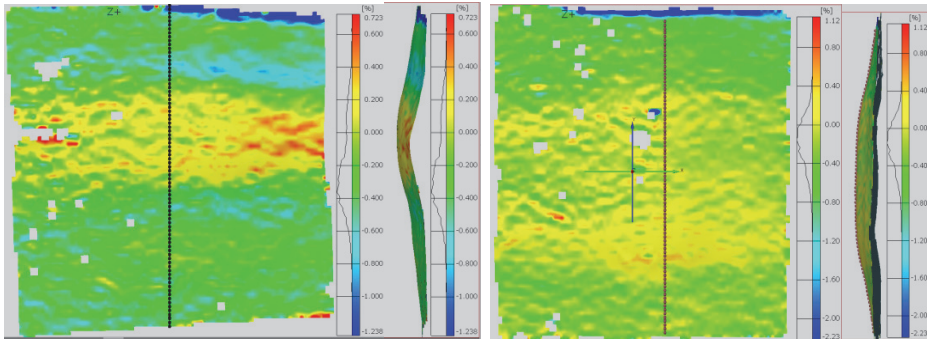


Figure 4.10 Compressive strain distribution on the surface of longitudinally placed PCB specimen at 222 MPa compressive stress and with transverse PCB at 237MPa

The comparison of the strain distributions are depicted in Figure 4.11 and Figure 4.12. The experimental values of the compressive strains differ from corresponding simulation results less than the tensile testing results. This can be explained by the fact that compression results are taken from a much lower mechanical stress level, where the signal-to-noise ratio of the scanner is worse. The waviness of the experimental curve might be caused by the woven fabric repeating structure. The tensile testing specimens have high strain differences in the regions where the SAW filter device ends and resin pockets begin. The maximum difference occurs in the transversely placed PCB specimen at longitudinal coordinate $Y = 7$ mm. The experimental strain value is 1.35% while the FE simulation value is 0.1%. This could be caused by the void bubbles near the edges of the SAW device.

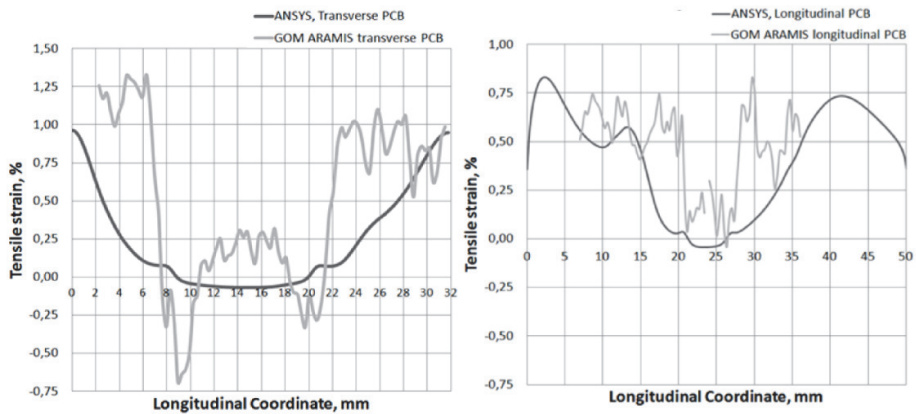


Figure 4.11 Tensile strain distribution comparisons. Left transverse and right longitudinal specimen

The compression results have a maximum difference also in the transversely placed PCB specimen at longitudinal coordinate $Y = 21$ mm. The experimental strain value is 0.35% while the FE simulation value is -0.05%. In both loading condition types the biggest differences between the simulation and experimental results are observed at the edges of the SAW device.

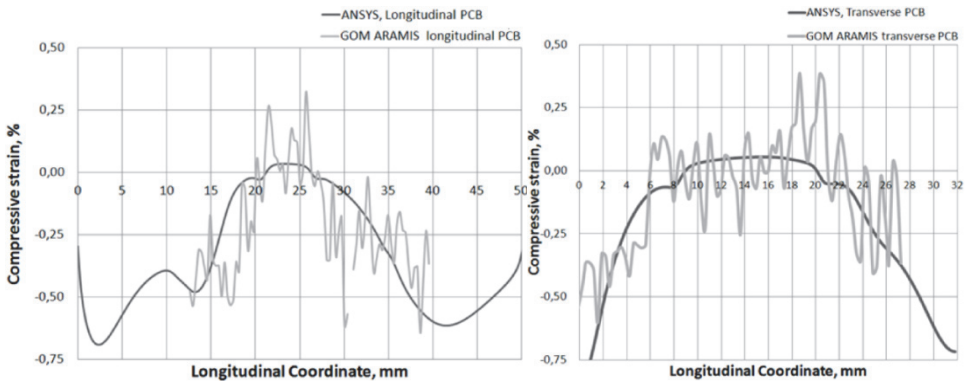


Figure 4.12 Compressive strain distributions comparison. Left transverse and right longitudinal specimen

4.4 Summary of the Results of First Embedment

An experimental study on the fully embedded complex circuit placeholder inside carbon fibre laminate has been performed. The mechanical performance of the laminate with the embedded system is examined. The most critical zones in the specimen are found to be the resin-rich pockets at the end of the circuit boards and high-stiffness metallic structures e.g. SAW filter.

The FEA model for simulating the behaviour of the laminate with embedded electronics has been developed and validated against experimental data. In most simulation cases the resin-rich pockets were the first to fail the test of factor of safety.

4.5 Design and Optimization of Embedded Foreign Object Geometry

Selective laser sintering (SLS) is technology which permits a layer-wise build-up of very complex geometrical shapes. It is an additive layer technology (ALT). SLS is a technology which is a feasible solution for manufacturing an enclosure around electronics which are to be integrated inside the main material.

This study section is focused on embedding SLS produced components inside the main structure. An SLS built enclosure around the composite reduces the elasticity mismatch or even isolates the incompatible materials from each other.

Inserting a foreign object inside the laminate is similar to the effect of a void on the composite structure. The change of geometry causes fibre undulation around the object and locally increased waviness. This change significantly affects structural performance of the composite [48]. Besides undulation, the embedded object has a different elasticity – if it is electronics, then it is much stiffer and causes extra stresses. In this article an SLS produced PA-12 nylon enclosure for electronics is inserted in the host material. The mechanical properties of PA-12 nylon are very similar to polyester resins and epoxy resins. Additionally SLS produced PA-12 nylon could weaken by hygrothermal influences [49]. A phenomenon called plasticization occurs. This further reduces the mechanical strength of the two material interface.

4.6 Methodology

Embedding the electronic components directly in composite may lead to impairments of the components during fabrication or exploitation of the composite structure (mechanical defects, overheating, etc.). For that reason additive layer technology has been employed for manufacturing housings which can host the electronic components.

Any embedded components have an impact on the mechanical, thermal, etc. properties of the composite structure. Thus, the design of housings is necessary. First the design of the experiment has been performed. Next the specimens with ALT manufactured embedded structures are fabricated and mechanical tests performed.

The finite element (FE) model has been developed for modeling the stress-strain behaviour of the composite structure with embedded components. The finite element model is validated through a comparison with digital image correlation scanner results. Also, the results obtained from mechanical tests and the FE model are compared. The FE model developed covers fibre undulation caused by embedded objects.

Based the experimental results amathematical model is developed.Finally the size and shape optimization of the embedded structure has been performed. The size of the pockets formed at ends of the embedded structure and the mechanical stresses around the embedded structure are considered as objective functions. The multicriteria optimization problem posed has been divided into a multistage optimization procedure and solved by use of a weighted summation technique.

4.7 Specimen Design

It is correct to point out that in the current context the design of the specimen contains mainly a housingdesign for electronics which will be mounted in the specimen (in addition to specimen dimensions, the shape and dimensions of the housing are considered as design variables).

The strength characteristics of the specimen have been analyzed. The following optimality criteria were selected:

$$\begin{aligned} F_1 &= H(x_1, \dots, x_n) \rightarrow \min, \\ F_2 &= L(x_1, \dots, x_n) \rightarrow \min, \\ F_3 &= \alpha_{max}(x_1, \dots, x_n) \rightarrow \min, \\ F_4 &= \sigma_f(x_1, \dots, x_n) \rightarrow \max, \end{aligned} \tag{4.1}$$

where H, L, α_{max} and σ_f stand for the height and length of the pocket, maximal angle of the pocket diagonal side and failure stress, respectively. Parameters x_1, \dots, x_n stand for design variables.

Before selection of multicriteria optimization strategy it is important to understand general characteristic behaviour of the optimality criteria used [26],[50],[51]. Preliminary analysis of the optimality criteria 4.1 allows to conclude, that in general:

- The optimality criteria F_1, F_2, F_3 given by 4.1 are not contradictory (decrease or increase for the same dataset).
- The optimality criterion F_4 increase with decreasing values of criteria F_1, F_2, F_3 and vice versa. However, criterion F_4 is subjected to maximization, and there is not contradictory with criteria F_1, F_2, F_3 .

Thus, there is no need to apply the Pareto optimality concept to handle conflicting objectives. In the following the weighted summation technique is employed. The objectives 4.1 should first be normalized, due to their different magnitude. The normalization is performed by formulas 2.5 for objectives subjected to minimization (F_1, F_2, F_3) and by formulas 2.6 for objectives subjected to maximization (F_4). In 4.1 to 4.4 $i = 1, 2, 3$ and \bar{x} stands for the vector of design variables.

According to weighted summation technique the combined objective can be written as

$$f = \sum_{i=1}^m w_i f_i \rightarrow \min, \quad (4.4)$$

where w_i stand for the weights of the objectives 4.1 to 4.4 and are evaluated as

$$w_1 = w_2 = w_3 = w_4 = 0.25, \quad (4.5)$$

i.e. all are considered to have the same importance.

The housings for embedded electronics with different shapes have a different number of design parameters x_1, \dots, x_n . For that reason the two level optimization strategy has been introduced [52 -54].

4.8 Higher Level Design

In the higher level design stage the most suitable shape and size of the housing have been determined. Rectangular, trapezoid, round and ellipse shapes are considered. The size of each shape has been varied. The full factorial design of the experiment has been employed for shapes except trapezoid. In the latter case the Taguchi design of experiment was applied. The size range was chosen to accommodate the structure to a specific electronic device. Circular cross-section has no real application potential. It was used in order to investigate the fibre undulation around a short object. The variables are discrete values as shown in Table 4.1.

Table 4.1: Variables of geometrical shapes

Shape	Length, mm	Height, mm	Side angle, °
Ellipse	10; 25; 40;	1; 2; 3;	-
Circular	diameter 1.5mm; 2mm; 4mm;		
Rectangular	10; 25; 40;	1; 2; 3;	-
Trapezoid	10; 25; 40;	1; 2; 3;	50; 53; 56;

The level values for Taguchi method is 3. Taguchi design matrix is depicted for trapezoid shape in Table 4.2.

Table 4.2 Parameter values for trapezoid

Nr.	Width, mm	Height, mm	Angle, °
1	10	1	50
2	10	2	53
3	10	3	56
4	25	1	53
5	25	2	56
6	25	3	50
7	40	1	56
8	40	2	50
9	40	3	53

The performed numerical analysis permits the conclusion that the ellipse appears to be the most suitable shape of the housing. Also the optimal values of the height and width of the housing are found to converge to 1 and 25, respectively. However, the results depend on selected values of weights 4.5, also from accuracy of the measured values of objectives functions. The smaller height of the housing is obviously better – causing less damage of the structure by not influencing the straightness of fibre bundles. Actually there are a lot of options for the selection, design of embedded electronics depending on cost, aptitude, etc. Unfortunately, not all variants of embedded electronics can be fitted in a housing with height values equal to 1mm and even to 2 mm. Thus, different heights should be considered for future analysis (cost can be included).

4.9 Lower Level Design

In lower level design the selected elliptic shape of the housing is assumed, but certain improvement of the shape is introduced. Namely, the elliptic shape is divided into two parts, consisting from two ellipses with different half-axes (see Figure 4.13).

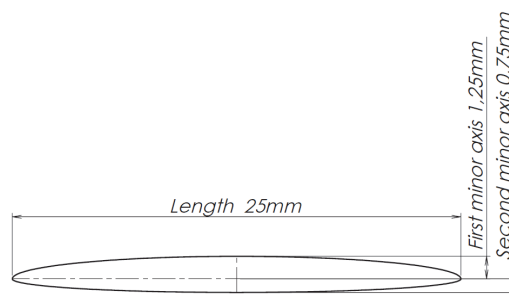


Figure 4.13 Design variables: minor half-axes and length

The minor half-axes of the ellipse are considered as design variables. For fixed values of the minor half-axes the major half-axes values are determined by total length of the ellipse and continuity conditions. The remaining design variable considered in lower level design is the length of the specimen.

Obtained preliminary numerical results include optimal design where the value of the length of the specimen is near the considered value and the minor half-axes of the lower ellipse (see Figure 4.13) is substantially smaller than the minor half-axes of the upper ellipse (1/2...1/4 depending on total height of the ellipse).

4.10 Specimen Manufacturing

The reinforcement is biaxial 0°/90° non-crimp type glass fibre with surface density 600g/m² and the matrix is vinylester resin ATLAC 580 ACT. The mechanical properties of the laminate are depicted in Table 4.3.

The foreign objects are manufactured with a EOS GmbH Formiga P100 selective laser sintering machine. Selective laser sintering technology allows creation of complex shapes with almost no geometrical limits. The base material is PA-12 polymer. The foreign objects were laminated between 6 plies of laminate on the mid-plane, the lay-up notation is [0°/0°/0°/ ForeignObject /0°/0°/0°]. The specimen was laminated at 0.8 bar vacuum and post-cured after manufacturing at 60°C for 16 hours.

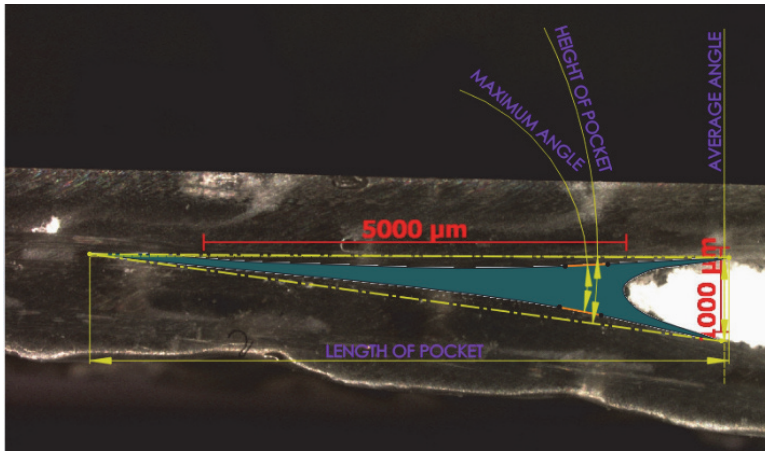


Figure 4.14 Example of resin pocket measurable parameters

Table 4.3 Mechanical properties of laminate

Property	Value
E_x, E_y	19.6GPa
E_z	5GPa
ν_{xy}	0.26
ν_{yz}	0.01
ν_{xz}	0.01
G_{xy}	3.28GPa
G_{xz}, G_{yz}	1.6GPa
σ_x^c, σ_y^c	215.9MPa
σ_x, σ_y	304.7MPa
$\tau_{xy}^{0,2}$	23.1MPa

4.11 Examination of Preliminary Specimens

The undulation size and shape will be estimated from sectioned specimens by the method of microphotography. The measurable parameters are depicted in Figure 4.14. It is known from various authors that fibre waviness is one of the most critical parameters of composite mechanical properties[48],[55]. In this study simple waviness parameters like amplitude and wavelength are not sufficient to describe the resin pocket properties. This is because the resin pocket around a foreign object is a single event, not a repeating pattern. Lemanski and Sutcliffe [56] measured fibre misalignment angle influence on the mechanical properties of unidirectional laminate. In this research the measurable parameters are as mentioned in the methodology section, the height H and length L of the pocket, maximal angle and average angle of the pocket diagonal side and failure stress σ_B , respectively. All the parameters except those of failure stress can be measured from microscope images. The data from these measurements was inserted into the weighted summation optimization procedure. The weight values are taken from equation 4.5.

4.12 Design of New Specimens

Based on the results of the weighted summation optimization method the smallest influence on fibre undulation was an ellipse with dimensions 25 mm x 2 mm. It was discovered during the microscopic examination procedure that some slender ellipses tried to conform to the flat manufacturing mould surface by bending the closer surface curvature to collinearity with the mould surface. Therefore it is proposed that the most suitable shape for the foreign object should instead be composed of two half ellipses with different minor radii. A batch with different half ellipse combinations was manufactured. The length of ellipse remained at the same 25 mm value, but the minor radius combinations were varied as depicted in Table 4.4. Two possible thicknesses for the whole foreign object were chosen. Also a special combination of half-ellipse and straight line was used (the sharp ends were rounded by fillet with radius 0.18 mm).

Table 4.4 Dimensions of new specimens

Length, mm	Minor radius 1, mm	Minor radius 2, mm	Total thickness, mm
25	2.75	0.25	3
25	1.5	0.5	2
25	3	flat	3
25	1.75	0.25	2
25	1.25	0.75	2
25	2.5	0.5	3

4.13 Examination of new specimens

The new batch of specimens had microphotography based measurements repeated analogically to the previous batch. The results are in Table 4.5.

Table 4.5 Results for new specimens

Shape No.	Pocket length, μm	Pocket height, μm	Avg. undulation angle, degrees	Max. undulation angle, degrees
1	4117	806	8.3	12.8
2	9203	1827	10.8	15
3	3650	764	8.8	12
4	14543	1653	5.5	11.3
5	1773	664	16.6	24
6	5705	1154	9.9	14.5

4.14 Mechanical Testing

The specimens with embedded object were tested only for tensile loading. It was concluded from previous research [56] that the main source of failure is delamination initiated from resin pockets at the interface surface of the foreign object and the matrix. The failure mechanisms are similar for compression and tension, the only difference being the reduction magnitude of the properties. Tensile testing is less sensitive to manufacturing faults, therefore it was chosen as a more reliable method. Testing was carried out with a tensile testing machine coupled with a digital image correlation (DIC) scanner. The base standard for test settings was ISO 527-4 (equivalent to ASTM D3039). The testing results are depicted in Figure 4.15 and summarized in Table 4.6.

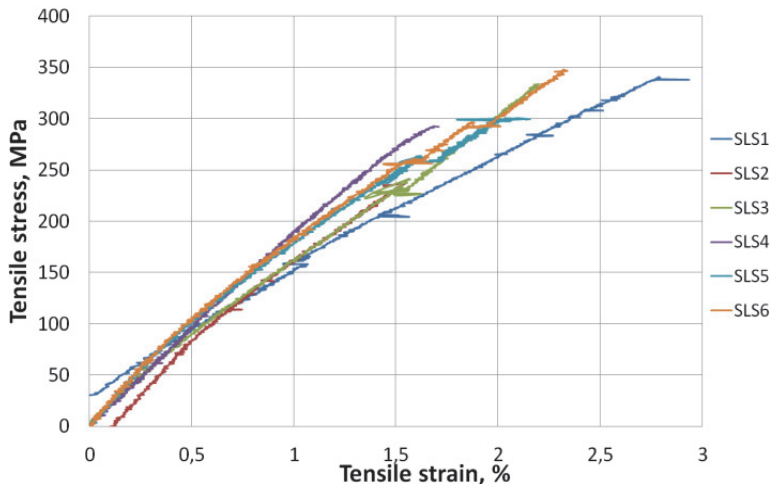


Figure 4.15 Tensile testing results chart

Table 4.6 Tensile testing results

No.	Thickness of undist. section, mm	Thickest point at for.object, mm	1st minor radius, mm	2nd minor radius, mm	Failure stress, MPa
SLS1	3.12	6.4	2.75	0.25	155.6
SLS2	2.93	5.3	1.5	0.5	231.6
SLS3	3.1	6.6	3	0	236.1
SLS4	3	5.3	1.75	0.25	202.8
SLS5	3	5.1	1.25	0.75	261.2
SLS6	3	6.3	2.5	0.5	252.3
Average:					223.28

Specimen number 5 had the highest strength which was 16.9% higher than the average. This specimen also had a very small resin pocket which was tightly packed by three 90° fibre yarns. Cross-section image is shown in Figure 4.16.

The actual tensile strength was determined from DIC scanning images. The laminate was considered to have failed after the occurrence of first macrocrack.



Figure 4.16 Specimen number 5 cross-section image. Foreign object visible at the right side of the image.

4.15 Digital Image Correlation Results

The strain distribution around and inside the embedded part was measured in the thickness direction at the side of the specimen using a GOM ARAMIS 2M digital image correlation scanner similarly to the method used in *Paper III*. The measuring volume was set to 35 mm x 25 mm. The computation type was set to total strain method and plane stress.

A post analysis for failure initiation and progression was conducted based on digital image correlation scanning results combined with microscope visual analysis. It is known that micro-damage development in NCF composites starts with transverse intra-bundle cracking as found in [58]. This was confirmed when gradient zones. For example, under the foreign object were investigated by microscope after the specimen failure.

The analysis of specimen failure from DIC results is a partially difficult task. This is due to image noise, lack of image resolution of the scanner to capture each micro defect and due to the fact that the scanner can see only the surface of the specimen instead of the full volume. The internal failures are not detectable. The used method to detect the failure is a procedure as follows:

1. Facet size was decreased to 12 pixels with 10 pixels overlap. This was conducted in order to increase the local defects detectability. Other settings for DIC scanning were left as they were before: validity quote 55% and computational size 3.
2. Defects were detected using von Mises strain gradients.

Strain level for failure was determined firstly using contour plot with a colour range of three times the standard deviation of all captured image data. All detected cracks with length approximately above 0.25mm were gathered. Crack initiation was considered as a change of gradient in two following images which had a size above the 0.25mm length value and the change of strain was visually identifiable in the measured location stress versus strain plot (see Figure 4.18 for further information).

First 10 failure points were chosen for evaluation. The average failure von Mises strain for transverse bundle cracks was 0.976% with standard deviation of 0.295%.

3. Contour plot strain range was set to 2% upper value based on average failure strains found in the previous point. This enables a good detectability of occurring cracks.
4. If the region of crack was noisy, a further refinement to the discrete values of colour range 1.5% or 3% was used. The 1.5% value increased the sensitivity to the crack occurrence and 3% value suppressed the neighbouring smaller defects gradients compared to the crack of interest.
5. Occurred gradient must be present after first appearance in all following images. Otherwise it is categorized under temporary image noise.
6. Crack length for cracks, that were bigger than bundle failure, was measured. Length measurement was conducted based on original images. The crack opening is usually easily visually distinguishable (see example in Figure 4.19).

The locations of failures were categorized into five zones. The location of the zones is depicted in Figure 4.17.

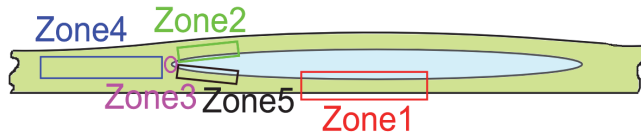


Figure 4.17 Locations of the failure zones

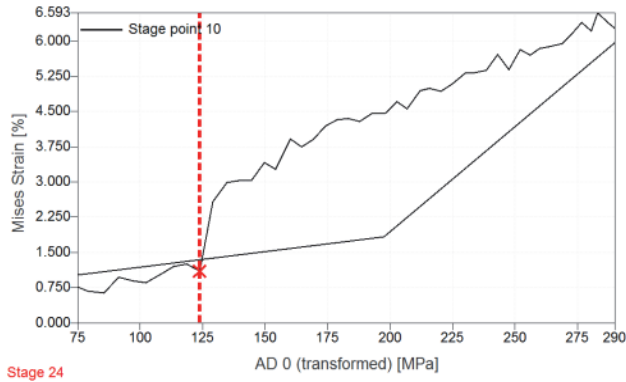


Figure 4.18 The stress versus strain plot of a measurement point in specimen nr.4. The rapid jump of strain is noticeable at stress of 125 MPa.

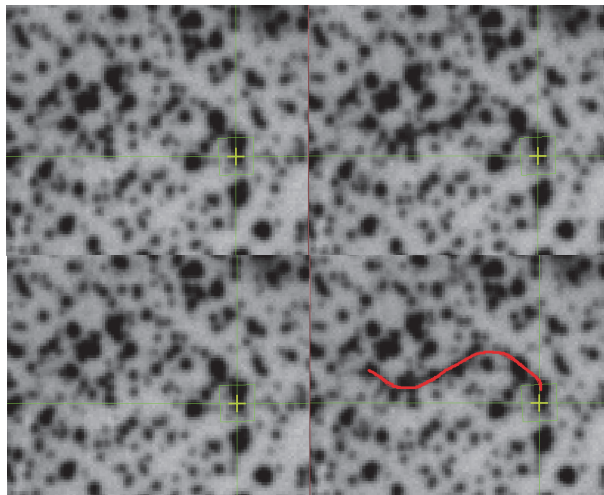


Figure 4.19 Visual crack identification example. Left row is without crack. Right has crack (red line highlights it)

According to the thickness of the foreign object the specimens can be categorized in two lots: specimen thickness 3mm and 2mm (see Table 4.6 for dimensions).

The sequence of failure process for specimens 1 and 3 is similar. First the object slips inside the specimen before cracking. Then a tip crack in zone 3 occurs before resin pocket cracks in zone 4. Specimen 6 starts to fail through transverse bundles cracking. At least 5 bundles fail before a tip crack develops. Resin pocket cracks occur before final failure.

Specimens 2 and 5 develop similar failure propagation. The failure starts with 6 transverse bundles progressively failing under the foreign object in zones 1 and 5. After that specimen 2 fails through a tip crack in zone 3. Specimen 5 has a tip crack, but before failure three pocket cracks occur in the resin pocket. Specimen 4 receives a tip crack after the first few transverse bundle failures. Right after the resin pocket cracks and transverse bundle failures lead turnwise into final failure.

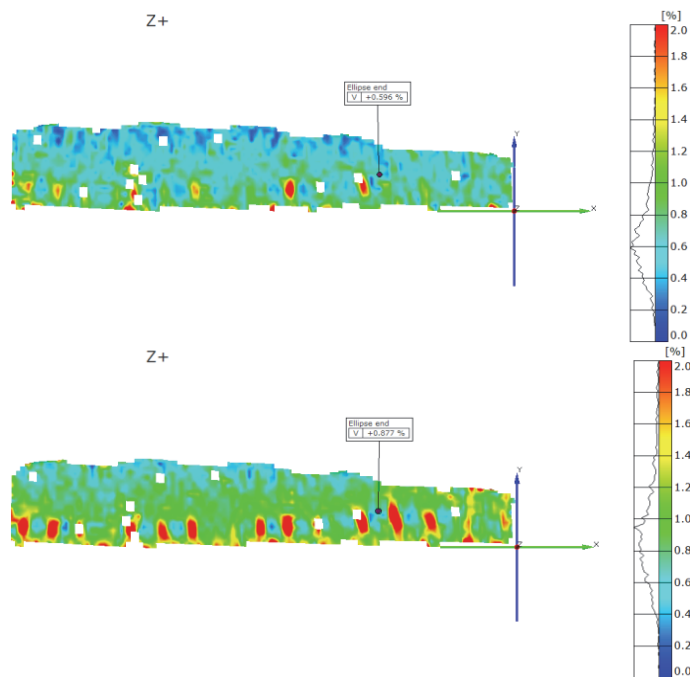


Figure 4.20 Von Mises strain on specimen 5 at 117 MPa (upper image) and 173MPa tensile stress (lower image)

The plots of strain distributions in all specimens are given in appendix I. Separate attention is given to the best performing specimen number five. The contour plot of von Mises strain distribution is depicted in Figure 4.20. Comparison of two stress levels reveals that the increase of stress causes transverse bundles that are lying under the foreign object to fail one-by-one. Also the resin pocket crack next to the embedded part has already developed. It is also identifiable that the length of the transverse bundle cracks increases in positive correlation with load. In Figure 4.21 shear angle distribution for the same loading conditions is depicted. The increase of shear strains right after the foreign object can be identified. The strains also tend to concentrate near to the upper surface of the specimen. Shear strains increase and saturate the whole in this region until the failure of the specimen at 262MPa stress. The shear strains are compared to the

strains of samples 2, 3 and 6 (appendix I, Figure 4). Base stress value is taken to be at the 170MPa level. The shear stress concentrates away from the embedded piece only for sample number 2. In cases 3 and 6 it is partially expanding on to the foreign object. Therefore it can be concluded that in the case of a 2 mm thick object the shear strains tend to withdraw from the object to the nearby resin pocket.

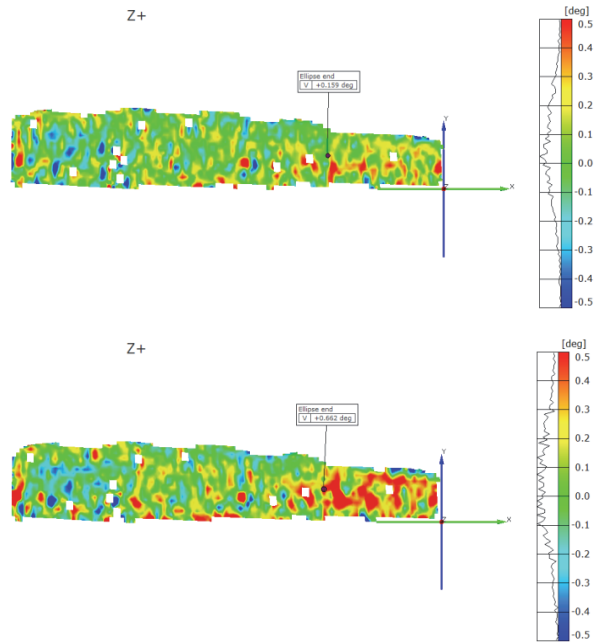


Figure 4.21 Shear angle on specimen 5 at 117MPa(upper image) and 173MPa tensile stress (lower image)

The order of failure propagation events is graphically summarized in Figure 4.22. It is identified that the longest failure propagation is for the strongest specimens: numbers 5 and 6. The best performing specimen 5 has the lowest ascent and distortion of failure stress curve until event number ten. The previous finding that shear strains concentrate away from the foreign object into the resin pocket is assumed to be the cause for similar failure propagation in the first seven points in samples number 2 and number 5, where transverse bundle cracking is the main source of failure.

The failure development events for all specimens are documented in Table 4.7 and Table 4.8. From this data and previous DIC results examination the following points are concluded:

- Failure in weakest specimens started from object slipping inside the specimen.
- First damage occurrences are transverse bundle cracks. Strongest specimens get most transverse bundles under the foreign object damaged during the tensile testing. Those transverse bundles that are in between the straightest longitudinal fibres and near the embedded part are the weakest.
- Resin pocket always cracks during tensile failure. Resin pocket cracks are in all instances perpendicular or near-perpendicular to the loading direction.

- In all cases, except specimen 2, a crack at the tip of the foreign object occurred before the resin pocket cracked.
- The strongest specimens 5 and 6 both developed multiple resin pocket cracks during the failure process. This could mean that the stress intensity is distributed on a larger area more evenly.
- Samples 2, 5 and 6 receive their first macro-scale crack in the pocket around the average value of 159.4MPa tensile stress. The length of crack shows a high value of released fracture energy in this zone. Edgren et al. [58] have used a calculation of stress times developed crack length to evaluate the released G_{1c} fracture energy. It means that in all three samples a noticeable amount of potential elastic energy gathers near the foreign object tip at an average distance of 1.48mm. The fracture is on average a 1.74mm long vertical crack.

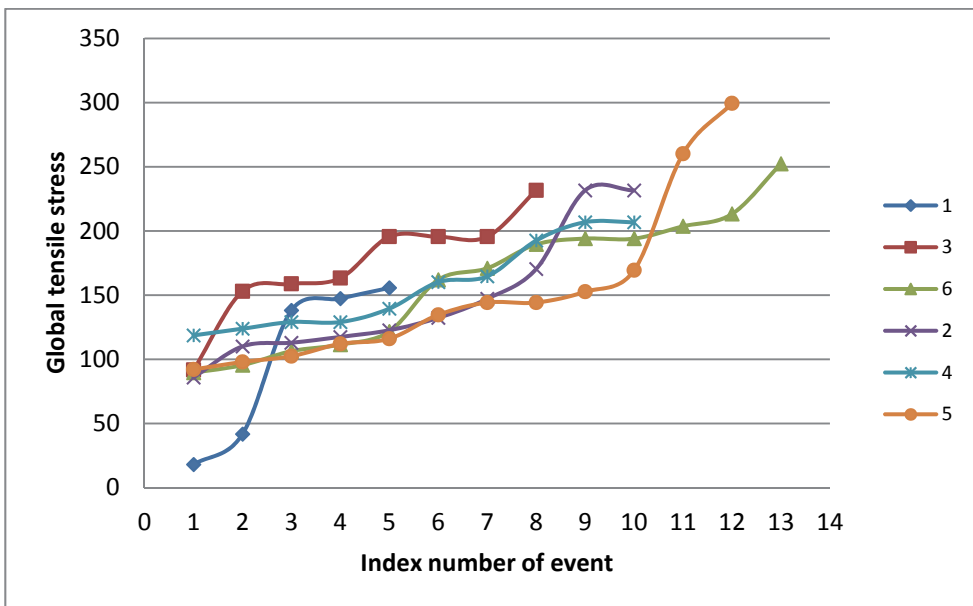


Figure 4.22 Order of the failure events

Table 4.7 Failure events of 3 millimetre thick specimens

Specimen nr [minor axis1;minor axis2]	Event	Crack length, mm	Tensile stress on specimen, MPa	Location zone number	Distance from nearest tip, mm
1 [2.75;0.25]	Object slipping		18	1	
	Object slipping		41.6	2	
	Tip crack		138.03	3	
	Pocket crack	1.43	147.3	4	2.56
	Final delamination failure		155.6	3	
3 [3;0]	Object slipping		91.6	1	
	Object slipping		152.9	2	
	2 Transverse bundle cracks		158.7	1	
	Transverse bundle crack	0.57	163.23	4	0.93
	Tip crack	1.2	195.5	3	
	Transverse bundle crack	1.12	195.5	4	3.29
	Transverse bundle crack	1.2	195.5	4	2.56
	Final delamination failure		231.6	-	
6 [2.5;0.5]	Small vertical crack		89.6	2	0.75
	Transverse bundle crack		95.4	5	4.3
	Transverse bundle crack		106.3	5	3.5
	Transverse bundle crack		111.4	1	
	Transverse bundle crack		121.6	1	
	Pocket crack	1.95	161.9	4	1.83
	Pocket crack	0.4	170.9	4	7.61
	Tipcrack		189.5	3	
	Tipcrack propagates to macro crack and slipping		194	3	
	Slipping		194	2	
	Pocket crack	0.54	203.6	4	4.13
	Pocket crack	0.37	213.2	4	5.52
	Final delamination failure		252.3		

Table 4.8 Failure events of 2 millimetre thick specimens

Specimen nr [minor axis1;minor axis2]	Event	Crack length. mm	Tensile stress on specimen. MPa	Location zone number	Distance from nearest tip. mm
2[1.5;0.5]	Transverse bundle crack		85.8	5	2.28
	Transverse bundle crack		110	5	3
	Transverse bundle crack		112.9	1	
	Transverse bundle crack		117.4	5	6.5
	Transverse bundle crack		122.6	1	
	Transverse bundle crack		132.26	5	4.16
	Pocket crack	1.59	147.1	4	1.66
	Transverse bundle crack		170.3	5	4.29
	Tip crack surrounding tip, tip slips		231.6	3	
	Final delamination failure		231.6		
4[1.75;0.25]	Transverse bundle crack		118.6	5	4.9
	Transverse bundle crack		123.8	1	8.9
	Tipcrack		129	3	
	Transverse bundle crack	1.37	129	1	
	Pocket crack		139.4	4	3.25
	2 Transverse bundle cracks		160.1	1	
	Pocket crack	0.84	164.6	4	6.4
	Transverse bundle crack		192.5	1	8.33
	Pocket crack	1.94	206.8	5	3.26
	Final delamination failure		206.8	-	
5[1.25;0.75]	Transverse bundle crack		92	1	17.7
	Transverse bundle crack		97.9	1	9.78
	2 Transverse bundle cracks		102.4	1	
	Transverse bundle crack		112	5	4.8
	Transverse bundle crack		116	5	1
	Tip crack		134.6	5	0.86
	Pocket crack	0.87	144.2	4	2.59
	Pocket crack	0.83	144.2	4	3.93
	Transverse bundle crack		152.6	1	
	Pocket crack	1.68	169.3	4	0.95
	Major Longitudinal crack		260.1	4	Above 3 previous cracks
	Final delamination failure		299.4		

4.16 Microscale FE Model

A microscale finite element model has been developed in order to investigate stress distribution inside the specimens. The model is a half symmetry in longitudinal direction of the best behaving specimen number five. The width of the model is chosen to describe the unit width of laminate which includes one warp fibre width. The length of the model is 23.5 mm and the width is 3.65 mm. The simulation model basic geometry is an assembly of 49 bodies. The bodies are categorized under fibre, matrix and foreign object. Fibre bundle sizes are derived from measurements from a microscope cross-sectioning procedure. Each yarn is composed of two ellipsoidal cross sections which in turns repeat themselves with a pattern step of 3.65mm. Its ellipsoidal half-axes are 1.51 mm and 0.19 mm. The cross-section which corresponds to the flattened yarn part has ellipse half-axes of 1.71mm and 0.14mm. The flattened ellipse ends are rounded with a tip fillet of 0.09 mm. This removes the unnecessary sharpening of cross-section at the ends.

The mesh of the model consists of 1689564 elements with local refinements in critical zones (see Figure 4.23). All solid-bodies are interfaced to each other with bonded contacts.

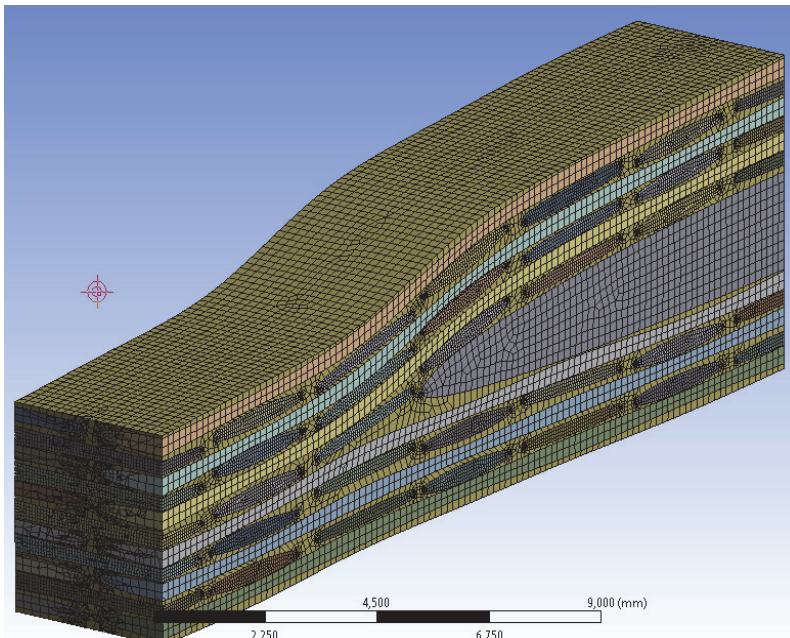


Figure 4.23 Meshing density

The mechanical properties of the materials used are listed in Table 4.9. Fibres have orthotropic material properties. Local coordinate systems were used to define the directional properties of fibre yarns. The resin and foreign object have isotropic material models. The simulation model uses linear elastic material models for all materials.

Table 4.9 Mechanical properties of materials used in FEM

Glass fiber yarn			Resin ATLAC 580 AC 300			Polyamide PA-12		
E_x	45	GPa	E	3.5	GPa	E	1.65	GPa
E_y	10	GPa	ν	0.38	-	ν	0.45	-
E_z	10	GPa						
ν_{xy}	0.291	-						
ν_{yz}	0.42	-						
ν_{xz}	0.291	-						
G_{xy}	4.8	GPa						
G_{yz}	3.8	GPa						
G_{xz}	4.8	GPa						

The load steps used are chosen based on specimen 5 failure events summarized in Table 4.8 at tensile stress 100, 115, 135, 150, 170 and 260 MPa. Loading scheme is depicted in Figure 4.24. The first examination loadstep is at 115 MPa stress. It is depicted in Figure 4.25. In experimental data already 6 transverse bundles under the foreign object have failed at this state. The left image indicates that longitudinal fibres experience a stress increase under the embedded object and also on the upmost layer away from the foreign object. The simulation model depicts that the bundles under the object are under high stress. Additionally it is noticed that the transverse fibres on the upper surface before the foreign object are also exposed to the increased tensile stress.

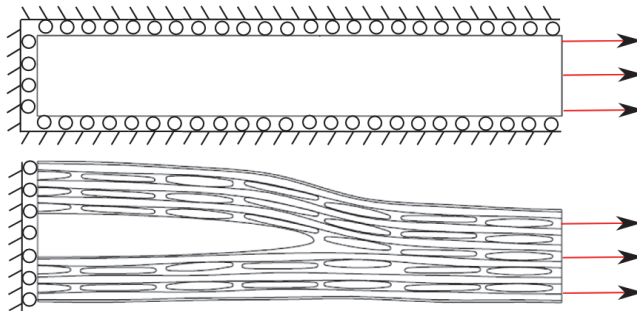


Figure 4.24 Boundary conditions of FEM model

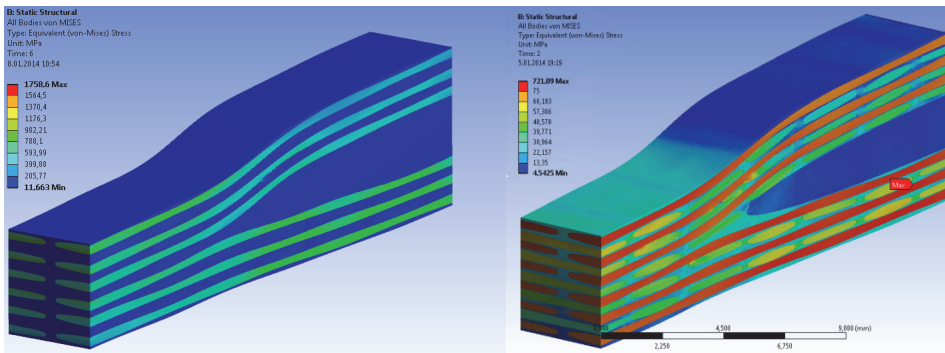


Figure 4.25 Von Mises stress distribution inside specimen at 115 MPa tensile stress with different contour map sensitivity.

The second load step under investigation is at a tensile stress of 170 MPa, depicted in Figure 4.26. From there it can be noticed that transverse bundles only above the foreign object are less loaded than other surrounding fibres. The resin pocket under the tip of the foreign object shows signs of a local increase of von Mises stress. The mechanical stress or strain between the bundle ends transfers to the neighbouring bundles. It can be visually identified that the von Mises stress intensity has a dependency of the distance between bundles. Therefore it might be a good idea to allow extra space between the bundles that are surrounding the foreign object.

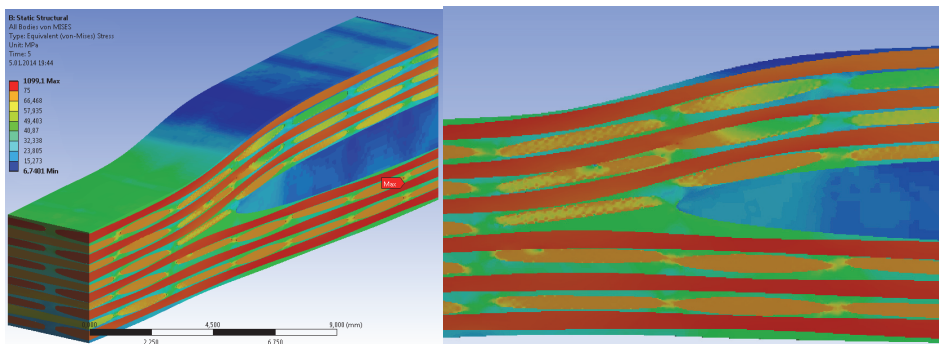


Figure 4.26 Contour plot of simulation model at 170 MPa tensile stress

The simulation model is also analysed with the use of von Mises equivalent elastic strain (Figure 4.27 and Figure 4.28.). The high strain zones are the same regions, which have the most fractures occurring in experimental data. In DIC scanner results section it was determined that the average failure von Mises strain for transverse bundle cracks is 0.976%. In Figure 4.27 it can be seen that the matrix areas surrounding the transverse bundles that are cracking in experimental data at this stress state are in simulation already tensioned with around 0.8% strain. This simulation model does not describe the interior contents of fibre bundles. The bundle fibre and matrix content has been homogenized and the output is homogenized elastic modulus.

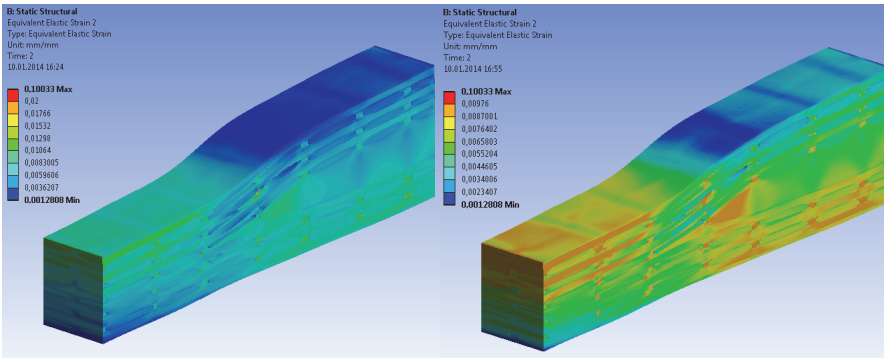


Figure 4.27 Von Mises equivalent strain distribution at 115MPa. Left image upper value for colour range is 2% and right 0.976%.

The finite element model and digital image correlation scanning results are compared in Figure 4.29. The average strain on the side-surface of the specimen is chosen for comparison. In ANSYS software the area of each element on the measured surface is used to weigh the influence of the nodal strain of the current elements on the average strain value on the whole surface. The procedure is conducted using ANSYS APDL language specific ARNODE() function. In the diagram the DIC scanning results standard deviation in each measurement point is also shown. The slope of the stress-strain curve is 4.3% higher for the experimental result if the trendline is calculated based on the full curve length. There is a noticeably higher slope at the beginning of the DIC stress-strain curve until a stress value of 161MPa. The slope of the curve in this region is 39.8% higher compared to FE model. For the whole range of two curves the stiffness has only 4.3% difference.

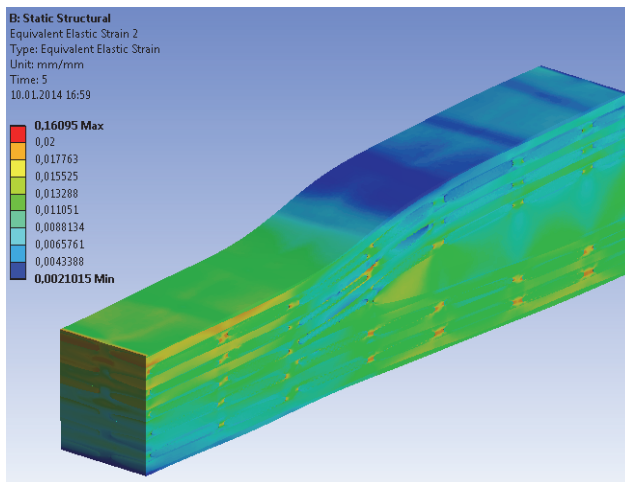


Figure 4.28 Von Mises equivalent strain distribution at 170 MPa. Upper value range for contour colors is 2%.

Table 4.8 reveals that around the 161MPa stress level a large pocket crack occurred which probably led to loss of stiffness. The conclusion can be drawn from comparison, that the DIC and FEM results are comparable for qualitative comparison. There is noticeable non-linearity in the experimental result due to material cracking, which

unfortunately the used FE model is unable to simulate. The validation was successful and the results of the microscale model can be used for qualitative analysis of smart composite structure.

From the FEM analysis the following points can be concluded for future analysis:

- The tip of the elliptical object still has some stress concentration occurring. This region is not optimum in its design. It needs further development.
- The main stress concentration areas are under the foreign object and just next to it. Shifting from laminate upper layers to lower layers.
- Thin layer of matrix around the foreign object helps to reduce stress gradients near the fibres.

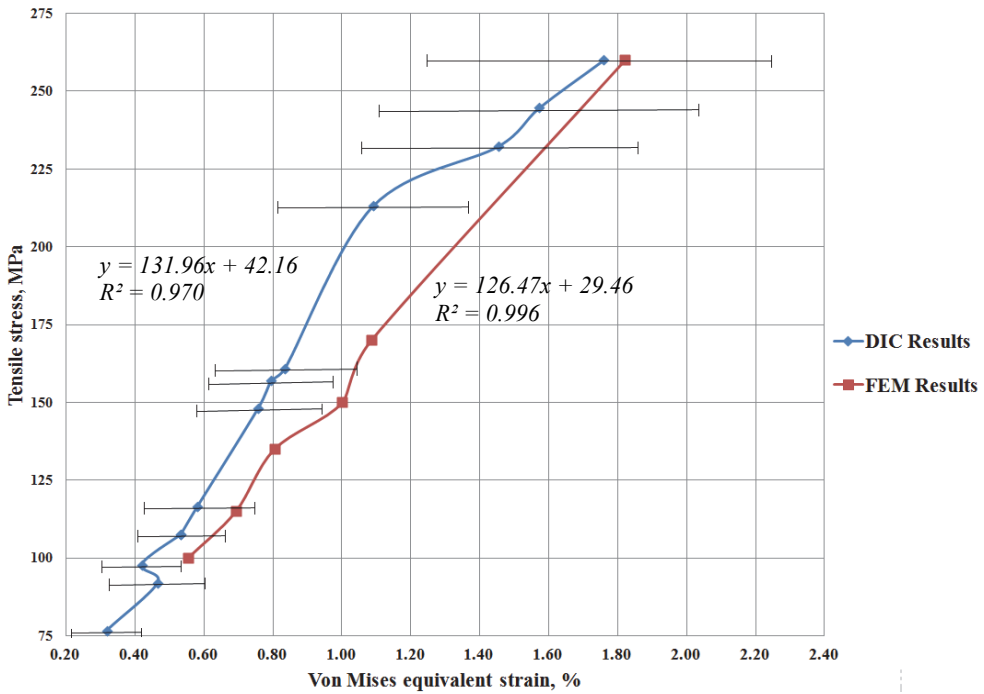


Figure 4.29 DIC scanning results and FEM model results comparison

5. CONCLUSIONS

The topic of this dissertation is the development of a smart composite material, which is composed of composite material layers and embedded foreign objects. The novelty of this thesis can be listed as follows:

- optimal design of smart composites is formulated and solved as a multicriteria and multilevel optimization problem,
- need for the interface layer between host structure and embedded electronic device has been experimentally verified,
- a novel concept of using additive layer technology to produce enclosure for embedded electronics has been proposed,
- an optimization strategy for the determination of optimal geometry of the enclosure has been developed (two half ellipses in considered case).

A literature study on electronic component miniaturization is conducted to compose a review of realistic possibilities to reduce the size of embedded devices for industrial application in the smart structure.

The main objective of the study has been achieved - the methodology for the design of smart composites with structural health and performance monitoring capabilities has been developed and validated in laboratory tests and real world applications (Goliath wind OÜ). The proposed methodology includes formulation of the multicriteria and multilevel optimization problem, development of solution procedure and concepts. In the following the fulfilment of the sub-objectives of the study is discussed in detail. The impact of embedded electronics on the mechanical properties has been minimized. The shape of the embedded object has a strong influence on the mechanical performance of the whole material. Therefore it is vital to design and optimize it well to comply and cooperate with the strains and stresses inside the host structure. The first attempt of full embedment was conducted with pure unencapsulated electronics. It was observed that the much more elastic host structure strains deform the electronics strongly and lead to early failure of the electronics components. The metallic components with a high modulus of elasticity are the most stressed. Visual examination determined that the components fail through multiple location cracking which leads to functional failure of electronics. The main locations of host structure failure start from resin pockets at the end of the foreign object where multiple material bonding points cause, through elasticity and Poisson ratio mismatch, an increase of stress levels. It is concluded that embedding pure electronics into composite laminate has severe performance issues for both components. Therefore it is feasible to isolate the strains of host material from interior content. The mechanical properties of composite laminate decreased roughly from 15% (average) to 33% (compression strength).

The integration of embedded electronics has been improved by introducing ALT technology. A novel concept of using additive layer technology to produce optimized encapsulation for the foreign object is proposed. Asymmetric ellipse cross-section is found to be the most optimal shape for NCF fabric material. The encapsulation shape is

optimized. The two level optimization procedure is developed for solving the multicriteria optimization problem posed. An analysis of the optimality criteria is performed and the weighted summation technique is applied. The multilevel optimization strategy proposed allows decomposing the initial problem into two simpler tasks, which can be solved sequentially. The obtained numerical results contain the optimal shape and size of the housing for embedded electronics. The optimization procedure helps to minimize the resin pocket dimensions, the criticality of which as a delamination starting point has been verified by the digital image correlation scanning and FEM analysis. The used linear elastic finite element model has been qualified as sufficiently accurate for evaluating strain distributions inside the specimen in a qualitative manner.

The procedure for price performance optimization of the composite sandwich is developed. As a result the composite structure with reasonable price has been developed. A Pareto frontier is developed to estimate the price performance behaviour of a structural material composed of discrete component materials. The response curve is non-linear and has a variable sensitivity in various regions.

The results of this research contribute to the better understanding of successful foreign object embedment inside composite laminate with the goal of influencing composite integrity minimally. The methodology developed in this research helps to develop smart composite materials with better mechanical performance and lower time-to-market.

REFERENCES

- [1] V. K. Varadan, K. J. Vinoy, and S. Gopalakrishnan, *Smart Material Systems and MEMS: Design and Development Methodologies*. John Wiley & Sons, 2006.
- [2] C. Vendittozzi, G. Sindoni, C. Paris, and P. P. del Marmo, "Application of an FBG sensors system for structural health monitoring and high performance trimming on racing yacht," in *2011 Fifth International Conference on Sensing Technology (ICST)*, 2011, pp. 617–622.
- [3] C. Ratcliffe, D. Heider, R. Crane, C. Krauthauser, M. K. Yoon, and J. W. Gillespie Jr., "Investigation into the use of low cost MEMS accelerometers for vibration based damage detection," *Composite Structures*, vol. 82, no. 1, pp. 61–70, Jan. 2008.
- [4] B. Wilson and A. S. Writer, "DISASTER - ONEAUSTRALIA BREAKS IN TWO, SINKS," *DeseretNews.com*. [Online]. Available: <http://www.deseretnews.com/article/408065/DISASTER---ONEAUSTRALIA-BREAKS-IN-TWO-SINKS.html?pg=all>. [Accessed: 22-Oct-2013].
- [5] 29 September 2003 David SaltABC Monday, "Yachts get bender detector," 29-Sep-2003. [Online]. Available: <http://www.abc.net.au/science/articles/2003/09/29/955984.htm>. [Accessed: 22-Oct-2013].
- [6] Charles R. Farrar and Keith Worden, "An introduction to structural health monitoring," *Philosophical Transactions of the Royal Society of London*, vol. 365, pp. 303–315, Dec. 2006.
- [7] A. Chateauinois, L. Vincent, B. Chabert, and J. P. Soulier, "Study of the interfacial degradation of a glass-epoxy composite during hygrothermal ageing using water diffusion measurements and dynamic mechanical thermal analysis," *Polymer*, vol. 35, no. 22, pp. 4766–4774, Oct. 1994.
- [8] S. Pavlidou and C. . Papaspyrides, "The effect of hygrothermal history on water sorption and interlaminar shear strength of glass/polyester composites with different interfacial strength," *Composites Part A: Applied Science and Manufacturing*, vol. 34, no. 11, pp. 1117–1124, Nov. 2003.
- [9] E. Green and A.J. Wood, "SSC-344 Development of an Onboard Strain Recorder." Ship Structure Committee, 1990.
- [10] Robert M. Jones, *Mechanics of Composite Materials*, vol. 2nd. Philadelphia, USA: Taylor & Francis Inc., 1998.
- [11] Ahmed A. S. Mohammed, Walied A. Moussa, and Edmond Lou, "High Sensitivity MEMS Strain Sensor: Design and Simulation," *Sensors 2008*, vol. 8, pp. 2642–2661, Feb. 2008.
- [12] S. F. Kenneth J. Bowles, "Void Effects on the Interlaminar Shear Strength of Unidirectional Graphite-Fiber-Reinforced Composites," *Journal of Composite Materials*, vol. 26, pp. 1487–1509, 1992.
- [13] M. L. Costa, M. C. Rezende, and S. F. M. D. Almeida, "Strength of hygrothermally conditioned polymer composites with voids," *Journal of Composite Materials*, vol. 39, pp. 1943–1961, 2005.
- [14] Czichon, Steffen, "Multiscale Failure Analysis of Fibre Reinforced Polymers with production induced Porosity Defects." University of Hannover, Institute of Statics and Dynamics, 2013.

- [15] L. Liu, B.-M. Zhang, D.-F. Wang, and Z.-J. Wu, "Effects of cure cycles on void content and mechanical properties of composite laminates," *Composite Structures*, vol. 73, pp. 303–309, Jun. 2006.
- [16] L. Liu, Z.-S. Guo, and B.-M. Zhang, "Experimental investigation of porosity and its effects on interlaminar shear strength in composite laminates," in *SAMPE '06: Creating New Opportunities For The World Economy, Apr 30-May 4 2006*, Long Beach, CA, United States, 2006, vol. 51, p. 7.
- [17] J. Hapke, F. Gehrig, N. Huber, K. Schulte, and E. T. Lilleodden, "Compressive failure of UD-CFRP containing void defects: In situ SEM microanalysis," *Composites Science and Technology*, vol. 71, no. 9, pp. 1242–1249, Jun. 2011.
- [18] C. J. Tsenoglou, S. Pavlidou, and C. D. Papaspyrides, "Evaluation of interfacial relaxation due to water absorption in fiber–polymer composites," *Composites Science and Technology*, vol. 66, no. 15, pp. 2855–2864, Dec. 2006.
- [19] A. Zafar, F. Bertocco, J. Schjødt-Thomsen, and J. C. Rauhe, "Investigation of the long term effects of moisture on carbon fibre and epoxy matrix composites," *Composites Science and Technology*, vol. 72, no. 6, pp. 656–666, Mar. 2012.
- [20] M. S. Amer, M. J. Koczak, and L. S. Schadler, "Relating hydrothermal degradation in single fibre composites to degradation behaviour in bulk composites," *Composites Part A: Applied Science and Manufacturing*, vol. 27, no. 9 PART A, pp. 861–867, 1996.
- [21] C. F. and W., Patrick O. Gerald, *Applied Numerical Analysis, Fifth Edition*. Addison - Wesley.
- [22] M. D. Rowe and B. L. Pierce, "Sensitivity of the weighting summation decision method to incorrect application," *Socio-Economic Planning Sciences*, vol. 16, no. 4, pp. 173–177, 1982.
- [23] M. Zeleny, *Programming. In: Multiple Criteria Decision Making*. Columbia: University of Southern Carolina Press, 1973.
- [24] D. H. Bassir, J. L. Zapico, M. P. González, and R. Alonso, "Identification of a spatial linear model based on earthquake-induced data and genetic algorithm with parallel selection," *International Journal for Simulation and Multidisciplinary Design Optimization*, vol. 1, no. 1, pp. 39–48, Dec. 2007.
- [25] J. M. Meelis Pohlak, "Engineering optimization of a car frontal protection system component," *Estonian Journal of Engineering*, vol. 15, no. 1, pp. 61–72, 2009.
- [26] M. Pohlak, J. Majak, K. Karjust, and R. Küttner, "Multi-criteria optimization of large composite parts," *Composite Structures*, vol. 92, no. 9, pp. 2146–2152, Aug. 2010.
- [27] J. Kers and J. Majak, "Modelling a new composite from a recycled GFRP," *Mech Compos Mater*, vol. 44, no. 6, pp. 623–632, Dec. 2008.
- [28] J. Kers, J. Majak, D. Goljandin, A. Gregor, M. Malmstein, and K. Vilsaar, "Extremes of apparent and tap densities of recovered GFRP filler materials," *Composite Structures*, vol. 92, no. 9, pp. 2097–2101, Aug. 2010.
- [29] A. B. Lostetter, F. Barlow, A. Elshabini, K. Olejniczak, and S. Ang, "Polymer thick film (PTF) and flex technologies for low cost power electronics packaging," pp. 33–40.
- [30] F. Bechtold, "A comprehensive overview on today's ceramic substrate technologies," *IEEE Xplore*, 15-Jun-2009. [Online]. Available: <http://ieeexplore.ieee.org/xpl/articleDetails.jsp?reload=true&arnumber=5272912>. [Accessed: 06-Oct-2013].

- [31] S. F. Al-Sarawi, D. Abbott, and P. D. Franzon, "A review of 3-D packaging technology," *IEEE Transactions on Components, Packaging, and Manufacturing Technology, Part B: Advanced Packaging*, vol. 21, no. 1, pp. 2–14, 1998.
- [32] S. P. Lacoura, S. Wagner, Z. Huang, and Z. Suo, "Stretchable gold conductors on elastomeric substrates," *APPLIED PHYSICS LETTERS*, vol. 82, no. 15, pp. 2404–2406, 2003.
- [33] D.-H. Kim, J. Xiao, J. Song, Y. Huang, and J. A. Rogers, "Stretchable, Curvilinear Electronics Based on Inorganic Materials," *Advanced Materials*, vol. 22, pp. 2108–2124, 2010.
- [34] G.-W. Hsieh, F. M. Li, P. Beecher, A. Nathan, Y. Wu, B. S. Ong, and W. I. Milne, "High performance nanocomposite thin film transistors with bilayer carbon nanotube-polythiophene active channel by ink-jet printing," *Journal of Applied Physics*, vol. 106, no. 12, p. 123706, Dec. 2009.
- [35] P. Liu, E. Sherman, and A. Jacobsen, "Design and fabrication of multifunctional structural batteries," *Journal of Power Sources*, vol. 189, no. 1, pp. 646–650, Apr. 2009.
- [36] J. F. Snyder, R. H. Carter, and E. D. Wetzel, "Electrochemical and Mechanical Behavior in Mechanically Robust Solid Polymer Electrolytes for Use in Multifunctional Structural Batteries," *Chem. Mater.*, vol. 19, no. 15, pp. 3793–3801, Jul. 2007.
- [37] J. P. Thomas and M. A. Qidwai, "The design and application of multifunctional structure-battery materials systems," *JOM*, vol. 57, no. 3, pp. 18–24, Mar. 2005.
- [38] A. Nathan, A. Ahnood, M. T. Cole, S. Lee, Y. Suzuki, P. Hiralal, F. Bonaccorso, T. Hasan, L. Garcia-Gancedo, A. Dyadyusha, S. Haque, P. Andrew, S. Hofmann, J. Moultrie, D. Chu, A. J. Flewitt, A. C. Ferrari, M. J. Kelly, J. Robertson, G. Amaratunga, and W. I. Milne, "Flexible Electronics: The Next Ubiquitous Platform," *Proceedings of the IEEE*, vol. 100, no. Special Centennial Issue, pp. 1486–1517, 2012.
- [39] "Thick-Film Ceramic Substrates Design Guide." CoorsTek, 2008.
- [40] "Technical characteristics and design rules of thick film printed ceramic substrates production." ELCERAM a.s., 2012.
- [41] Y. Y. Li, "Hypersensitivity of strain-based indicators for structural damage identification: A review," *Mechanical Systems and Signal Processing*, vol. 24, no. 3, pp. 653–664, Apr. 2010.
- [42] R. B. Watson, "Bonded Electrical Resistance Strain Gages," in *Springer Handbook of Experimental Solid Mechanics*, W. N. Sharpe, Ed. Boston, MA: Springer US, 2008, pp. 283–334.
- [43] Haksoo Choi, Sukwon Choi, and Hojung Cha, "Structural Health Monitoring system based on strain gauge enabled wireless sensor nodes," 2008, pp. 211–214.
- [44] A. Chateauminois, L. Vincent, B. Chabert, and J. P. Soulier, "Study of the interfacial degradation of a glass-epoxy composite during hygrothermal ageing using water diffusion measurements and dynamic mechanical thermal analysis," *Polymer*, vol. 35, no. 22, pp. 4766–4774, Oct. 1994.
- [45] S. Pavlidou and C. . Papaspyrides, "The effect of hygrothermal history on water sorption and interlaminar shear strength of glass/polyester composites with different interfacial strength," *Composites Part A: Applied Science and Manufacturing*, vol. 34, no. 11, pp. 1117–1124, Nov. 2003.

- [46] A. J. C. Hansen, J.P. Vizzini, "Fatigue Response of a Host Structure with Interlaced Embedded Devices," *Journal of Intelligent Material System and Structures*, vol. 11, pp. 902–909, 2000.
- [47] S. Mall and J. M. Coleman, "Monotonic and fatigue loading behavior of quasi-isotropic graphite/epoxy laminate embedded with piezoelectric sensor," *Smart Material Structures*, vol. 8, pp. 822–832, 1998.
- [48] H.-J. Chun, J.-Y. Shin, and I. M. Daniel, "Effects of material and geometric nonlinearities on the tensile and compressive behavior of composite materials with fiber waviness," *Composites Science and Technology*, vol. 61, no. 1, pp. 125–134, Jan. 2001.
- [49] R. Seltzer, F. M. de la Escalera, and J. Segurado, "Effect of water conditioning on the fracture behavior of PA12 composites processed by selective laser sintering," *Materials Science and Engineering: A*, vol. 528, no. 22–23, pp. 6927–6933, Aug. 2011.
- [50] K. Karjust, M. Pohlak, and J. Majak, "Technology Route Planning of Large Composite Parts," *Int J Mater Form*, vol. 3, no. 1, pp. 631–634, Apr. 2010.
- [51] M. Pohlak, R. Küttner, and J. Majak, "Modelling and optimal design of sheet metal RP&M processes," *Rapid Prototyping Journal*, vol. 11, no. 5, pp. 304–311, Dec. 2005.
- [52] J. Majak and M. Pohlak, "Decomposition method for solving optimal material orientation problems," *Composite Structures*, vol. 92, no. 8, pp. 1839–1845, Jul. 2010.
- [53] J. Majak and M. Pohlak, "Optimal material orientation of linear and non-linear elastic 3D anisotropic materials," *Meccanica*, vol. 45, no. 5, pp. 671–680, Oct. 2010.
- [54] J. Lellep and J. Majak, "Nonlinear constitutive behavior of orthotropic materials," *Mech Compos Mater*, vol. 36, no. 4, pp. 261–266, Jul. 2000.
- [55] G. Karami and M. Garnich, "Effective moduli and failure considerations for composites with periodic fiber waviness," *Composite Structures*, vol. 67, no. 4, pp. 461–475, Mar. 2005.
- [56] S. L. Lemanski and M. P. F. Sutcliffe, "Compressive failure of finite size unidirectional composite laminates with a region of fibre waviness," *Composites Part A: Applied Science and Manufacturing*, vol. 43, no. 3, pp. 435–444, Mar. 2012.
- [57] H. Herranen, G. Allikas, M. Eerme, K. K. Vene, T. Otto, A. Gregor, and M. Kirs, "Visualization of strain distribution around the edges of a rectangular foreign object inside the woven carbon fibre specimen," *Estonian Journal of Engineering*, vol. 18, no. 3, pp. 279–287, 2012.
- [58] F. Edgren, D. Mattsson, L. E. Asp, and J. Varna, "Formation of damage and its effects on non-crimp fabric reinforced composites loaded in tension," *Composites Science and Technology*, vol. 64, no. 5, pp. 675–692, Apr. 2004.

OTHER PUBLICATIONS

- [1] T. Saar, M. Reidla, O. Märtens, R. Land, M. Min, and H. Herranen. “Chirp-Based Piezo-Impedance Measurement,” in *Proceedings of WISP2013 8th IEEE International Symposium of Intelligent Signal Processing*, 2013, pp. 83–86.
- [2] G. Allikas, J. Kers, A. Aruniit, H. Herranen, M. Eerme, J. Majak, M. Pohlak, and O. Pabut, “Design of Light-weight Sandwich Panels for Trailers.” in *Proceedings of Fifteenth European Conference of Composite Materials*, 2012.
- [3] O. Pabut, G. Allikas, H. Herranen, R. Talalaev, and K. Vene, “Model Validation and Structural Analysis of a Small Wind Turbine Blade.” in *Proceedings 8th International Conference of DAAAM Baltic Industrial Engineering*, 2012. pp. 74–79.
- [4] J. Majak, M. Kirs, M. Mikola, M. Heero, and H. Herranen, “Nanoscale Vibration Analysis of Graphene Sheets Using Nonlocal Elasticity Theory,” in *Proceedings of International Conference on Composites/Nano Engineering (ICCE 21)* 2013.
- [5] A. Aruniit, J. Kers, D. Goljandin, M. Saarna, K. Tall, J. Majak, and H. Herranen, “Particulate Filled Composite Plastic Materials from Recycled Glass Fibre Reinforced Plastics.” *Materials Science (Medžiagotyra)*, Kaunas University of Technology, vol.18, no.1 2012.
- [6] A. Aruniit, J. Kers, A. Krumme, M. Antonov, G. Allikas, H. Herranen, and O. Pabut, “Wear Resistance Influencers of Particle Reinforced Polymer Composite.” in *Proceedings of 19th International Conference on Composite Materials (ICCM19)*, 2013.

AKNOWLEDGEMENTS

This research was supported by the national R&D program "Materials Technology" project „Smart Composites - Design and Manufacturing“ 3.2.1101.12-0012. ETF grant 8485 and targeted financing project SF0140035s12.

I would like to thank all my colleagues in the Department of Machinery, in the Department of Materials Engineering and in the Thomas Johann Seebeck Department of Electronics (ELIN). Firstly I would like to thank my supervisors professor Martin Eerme and especially co-supervisor Jüri Majak. This dissertation would not be like it is without their systematic supervising and guidance.

Special thanks to colleagues, who's assistance and cooperation was invaluable: professor Tauno Otto, professor Jaan Kers, dr.Tõnis Saar from ELIKO and mr. Georg Allikas from Department of Machinery.

Thanks to dr. Steffen Czichon from Germany for pleasant cooperation. This thesis benefited alot from knowledge he shared.

I would like to also thank my family: my father Toivo, brothers Reino and Tarmo and my girlfriend Maarja. Their patience and constant support during my studies was remarkable. I am truly thankful to my mother Hiie, who unfortunately did not live long enough to see my graduation. May your soul rest in peace mom.

Finally special thanks to my friend ms. Jessica Page, whose support and kindness to help with the language correction was highly valuable.

ABSTRACT

"Design Optimization of Smart Composite Structures with Embedded Devices"

The topic of this dissertation is the development of a smart composite material, which is composed of layers of composite material and embedded foreign objects.

A literature study on electronic component miniaturization is conducted to compose a review of realistic possibilities to reduce the size of embedded devices for industrial application in the smart structure.

An experimental investigation of semiconductor strain gauge mechanical behaviour under hygrothermal and fatigue loading is performed. The results reveal that the performance of a mechanically loaded embedded device is severely compromised by hygrothermal loading. The sea salinity corrosion process gets through the laminate thickness to the device and affects it. Otherwise semiconductor strain gauges are determined to be good candidates for fully embedded strain sensing.

The impact of embedded electronics on the mechanical properties of composite has been experimentally verified with the aid of DIC scanning and with the use of optimization minimized. The shape of the embedded object has a strong influence on the mechanical performance of the whole material. Therefore it is vital to design and optimize it well to comply and cooperate with the strains and stresses inside the host structure. The first attempt of full embedment was conducted with pure un-encapsulated electronics. It was observed that the much more elastic host structure strains deform the electronics strongly and lead to early failure of the electronics components. The metallic components with a high modulus of elasticity are the most stressed. Visual examination determined that the components fail through multiple location cracking which leads to functional failure of electronics. The main locations of host structure failure start from resin pockets at the end of the foreign object, where multiple material bonding points cause, through elasticity and Poisson ratio mismatch, an increase of stress levels. It is concluded that embedding pure electronics into composite laminate has severe performance issues for both components, therefore it is feasible to isolate the strains of host material from interior content.

The integration of embedded electronics has been improved by introducing ALT technology. A novel concept of using additive layer technology to produce optimized encapsulation for the foreign object is proposed. Asymmetric ellipse cross-section is found to be the most optimal shape for NCF fabric material. The encapsulation shape is optimized. The two level optimization procedure is developed for solving the multicriteria optimization problem posed. An analysis of the optimality criteria is performed and the weighted summation technique is applied. The multilevel optimization strategy proposed allows decomposing the initial problem into two simpler tasks. which can be solved sequentially. The obtained numerical results contain the optimal shape and size of the housing for embedded electronics. The optimization procedure helps to minimize the resin pocket dimensions, the criticality of which as a delamination starting point has been verified by the digital image correlation scanning and FEM analysis. The

used linear elastic finite element model has been qualified as sufficiently accurate for evaluating strain distributions inside the specimen in a qualitative manner.

The procedure for price performance optimization of the composite sandwich is developed. As a result the composite structure with reasonable price has been developed. A Pareto frontier is developed to estimate the price performance behaviour of a structural material composed of discrete component materials. The response curve is non-linear and has a variable sensitivity in various regions.

The main objective of the study has been achieved - the methodology for the design of smart composites with structural health and performance monitoring capabilities has been developed and validated in laboratory tests and real world applications.

KOKKUVÕTE

"Integreeritud elektroonikakomponentidega targa komposiitmaterjali väljatöötamine"

Antud doktoritöö teemaks on targa komposiitmaterjali arendamine, mis koosneb komposiitmaterjali kihtidest ning integreeritud elektroonikakomponentidest. Elektroonikakomponentideintegreerimise probleem on sõnastatud multikriteeriaalse ning mitmetasemelise optimeerimisülesandena. Töö konkreetseks eesmärgiks on minimeerida integreeritud elektroonikakomponendi ning seda ümbritseva komposiitmaterjali omavahelist negatiivset vastastikmõju. Töös on kasutatud järgnevaid meetode:

- Probleemi dekompositsioon alamprobleemideks,
- Metamudelite kasutamine,
- Materjalide käitumise lihtsustamine,
- Digitaalse pildikorrelatsiooni skanneriga lõplike elementide mudelite valideerimine.

Elektroonika komponentide mõõtmete vähendamise võimalikkuse uurimiseks sooritati infootsing olemasolevate tööstuslike võimaluste kaardistamiseks.

Töös katsetati pooljuht-tensoandurite sobilikkust komposiitmaterjalisse integreeritud anduritena kasutamise seisukohalt. Sooritati hügrotermiline vanandamine ning sellele järgnev väsimuskatsetus. Hügrotermiline vanandamine imiteerib merekeskkonnas vananemist. Katsetamise tulemuseks on järeldused, et hügrotermiline koormamine kahjustab korrosiooni jm mehhanismide läbi tugevalt andurit, ent sellegipoolest on pooljuht-tensoandur hea kandidaat komposiitmaterjalisse integreerimiseks.

Integreeritud objekti mõju loodud komposiitstruktuuri mehaanilisele suutlikkusele määratleti eksperimentaalkatsetusega ning seda minimeeriti. Esimene katse integreerida võõrkeha sooritati ilma väliskestata elektroonikaga. Katsest selgus, et palju elastsem ümbritsev komposiitmaterjal sunnib oma deformatsioonidega elektroonikat kaasa deformeeruma, mis põhjustab elektroonikakomponentide varajase purunemise. Kõige enam on mehaanilise pinge poolt koormatud komposiidist kordades kõrgemate elastsusmoodulitega metalsed komponendid. Visuaalvaatlus tuvastas, et purunemine toimub rohkearvuliste mõrade ilmnemise näol. Komposiidist põhstruktuuri kahjustumine algab vaigutaskute vigastuste tekkimisega võõrkeha otstes. Seal kontsentreeruvad mehaanilised pinged mitme materjali kokkupuutepunktis tänu elastsusmoodulite ning Poissoni tegurite erinevuste tõttu. Antud katsest järeldati, et kaitsmata kujul elektroonika integreerimine põhjustab nii iseendale kui ka ümbritsevatele komposiitstruktuurile tugevat mehaaniliste ning funktsionaalsete omaduste langust. Seetõttu on vajalik isoleerida komposiitmaterjali tööolukorras ilmnevad deformatsioonid integreeritud elektroonilistest komponentidest.

Elektroonika integreerimist komposiitmaterjalisse on parendatud kasutades aditiivset laserpaagutustehnoloogiat. Elektroonikakomponendi kaitsmiseks deformatsioonide eest loodi aditiivse laserpaagutusseadme abil optimaalne elektroonika ümber paigutatav kaitsekest. Kaitsekesta kuju optimeeriti mitmekriteeriaalse kahetasemelise optimeerimise

protseduuri abil. Optimeerimine sooritati kasutades kaalutud summeerimise meetodit. Väljatöötatud mitmetasemeline optimeerimise strateegia võimaldab uuritava probleemi jaotada kaheks alamprobleemiks, mis lahendatakse järjestikuliselt. Saavutatud numbriline tulemus sisaldab kaitsekesta optimaalset kuju ning suurust. Optimeerimise protseduur aitab minimeerida võõrkeha ümber tekkiva vaigutasku mõõtmeid. Selle tasku suuruse kriitiline mõju laminaadi delamineerumis-vastupanule on eksperimentaalselt ning numbrilisi meetodeid kasutades kontrollitud. Eksperimentaalne mõõtmine viidi läbi kasutades digitaalset pildi korrelatsiooni skannerit GOM ARAMIS 2M. Numbrilise meetodina kasutati lõplike elementide meetodi. Loodud mikromehaaniline lõplike elementide mudel näitab, et võõrkeha väliskesta optimaalset kuju on võimalik veel täiustada pingete kontsentratsiooni vähendamiseks. Optimaalseks loetud elliptilise kaitsekesta otsades kontsentreeruvad von Mises´e deformatsioonid ning samuti on neil siiski veel gradiendid ebasümeetriliselt komposiidi laminaadi külgedel.

Protseduur *sandwich* komposiitpaneeli hinnasuutlikkuse optimeerimiseks on loodud. Loodi Pareto front hindamaks diskreetsetest komponentidest valmistatud struktuurse materjali hinnasuutlikkust. Saadud funktsiooni kõver on mittelineaarne ning katkev, olles erineva tundlikkusega erinevate piirkondades.

Töö põhieesmärk on saavutatud. Loodi metodoloogia struktuuri seisundi monitoorimiseks ettenähtud targa komposiitmaterjali projekteerimiseks ning see valideeriti kasutades eksperimentaalkatseid nii laboris kui ka lõpprakenduses.

APPENDICES

Digital image correlation results from tensile testing of specimens with embedded elliptical foreign objects.

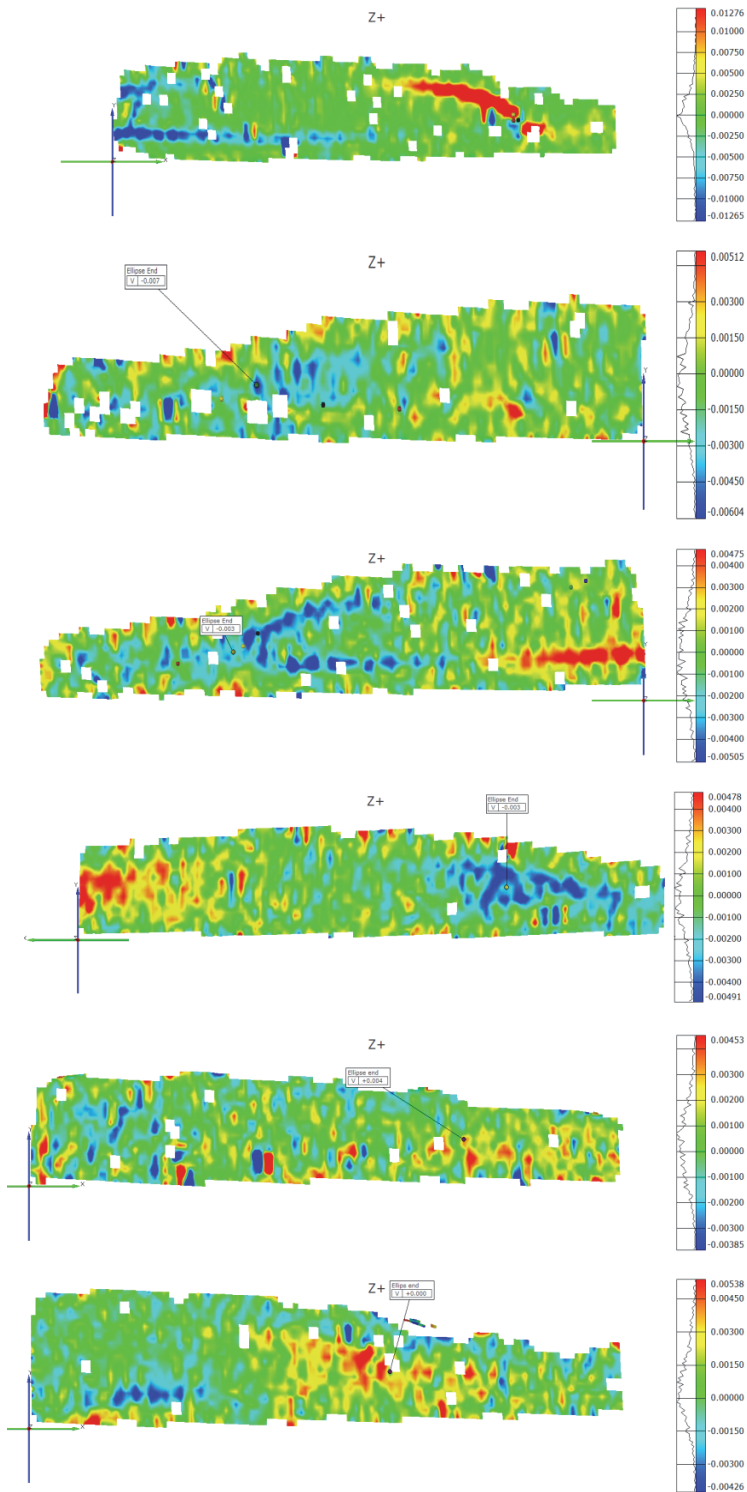


Figure 1 Shear strains of specimens from up 1 to 6 at tensile stress 118MPa

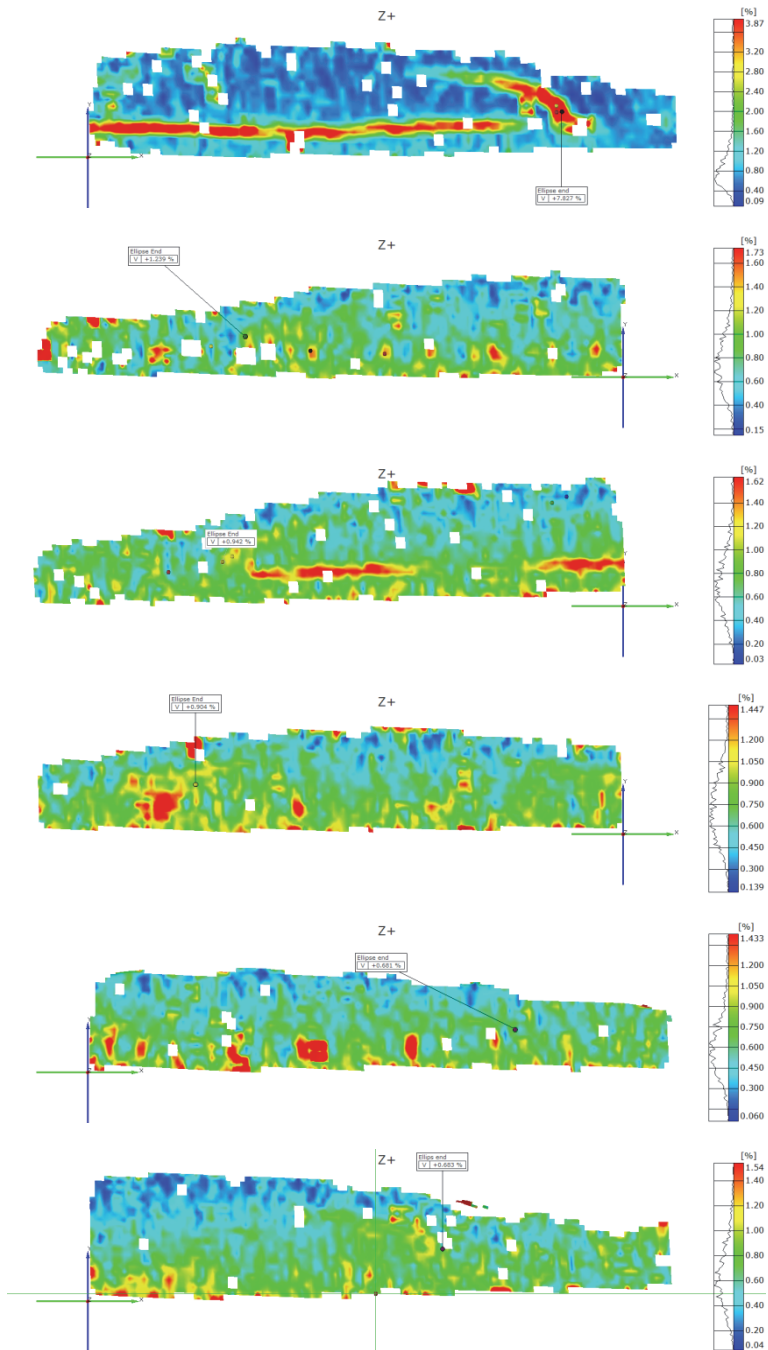


Figure 2 Von Mises strains of specimens from up 1 to 6 at tensile stress 118 MPa

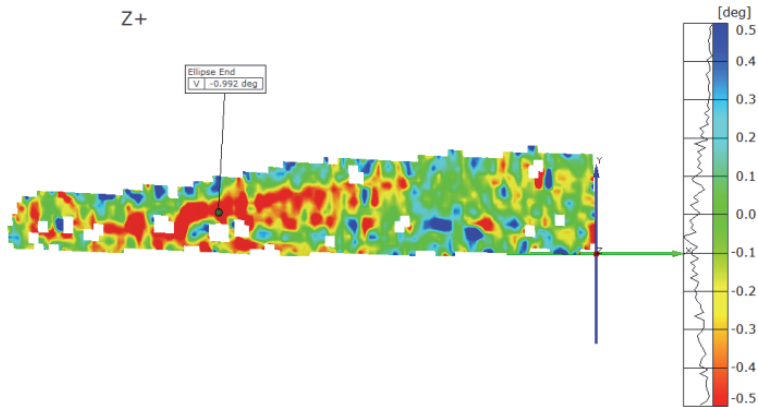


Figure 3 Shear strains of specimen 2 at 170 MPa tensile stress

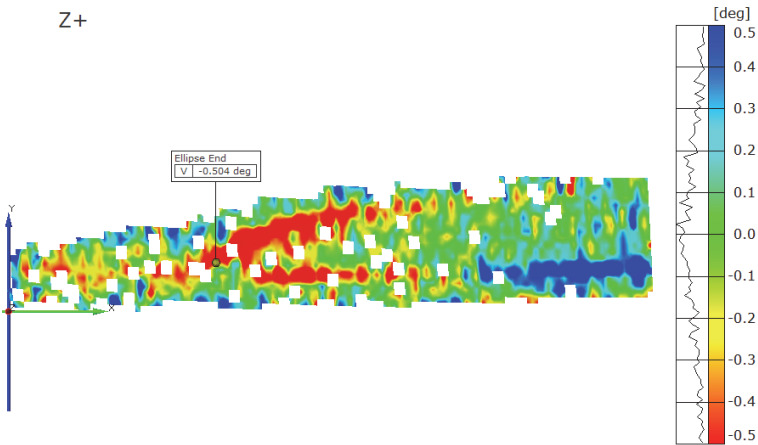


Figure 4 Shear strains of specimen 3 at 170 MPa tensile stress

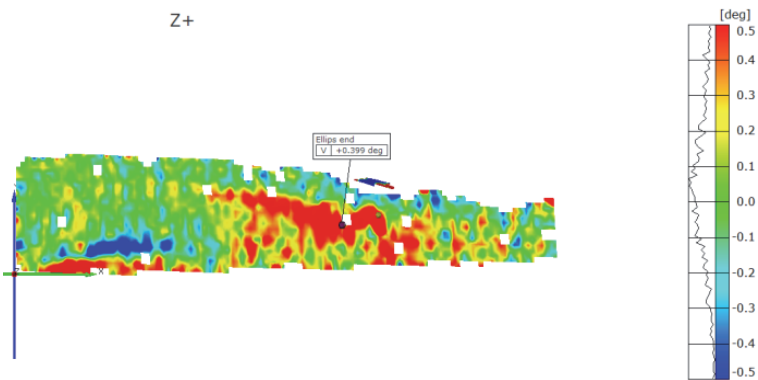


Figure 5 Shear strains of specimen 6 at 171 MPa

Paper I

H. Herranen, O. Pabut, M. Eerme, J.Majak, M. Pohlak, J. Kers, M. Saarna, G. Allikas, A. Aruniit, "Design and Testing of Sandwich Structures with Different Core Materials" *Materials Science (Medžiagotyra), Kaunas University of Technology*, vol. 18, no.1 ,pp.1-6, 2012.

Design and Testing of Sandwich Structures with Different Core Materials

Henrik HERRANEN^{1*}, Ott PABUT¹, Martin EERME¹, Jüri MAJAK¹, Meelis POHLAK¹,
Jaan KERS², Mart SAARNA², Georg ALLIKAS², Aare ARUNIIT²

¹Department of Machinery, Tallinn University of Technology, Ehitajate tee 5, 19086 Tallinn, Estonia

²Department of Materials Engineering, Tallinn University of Technology, Ehitajate tee 5, 19086 Tallinn, Estonia

crossref <http://dx.doi.org/10.5755/j01.ms.18.1.1340>

Received 13 June 2011; accepted 05 September 2011

The purpose of this study was to design a light-weight sandwich panel for trailers. Strength calculations and selection of different materials were carried out in order to find a new solution for this specific application. The sandwich materials were fabricated using vacuum infusion technology. The different types of sandwich composite panels were tested in 4-point bending conditions according to ASTM C393/C393M. Virtual testing was performed by use of ANSYS software to simplify the core material selection process and to design the layers. 2D Finite element analysis (FEA) of 4-point bending was made with ANSYS APDL (Classic) software. Data for the FEA was obtained from the tensile tests of glass fiber plastic (GFRP) laminates. Virtual 2D results were compared with real 4-point bending tests. 3D FEA was applied to virtually test the selected sandwich structure in real working conditions. Based on FEA results the Pareto optimality concept has been applied and optimal solutions determined.

Keywords: sandwich structures, 4-point bending tests, FEA, virtual testing, multicriteria optimization.

1. INTRODUCTION

Sandwich composites have high strength to weight ratio (which results in increase of payload, provides greater range and/or reduced fuel consumption), extended operational life, lower maintenance cost (due to less corrosion, and resistance to marine boring organisms), as well as a range of integrated functions, such as thermal and sound insulation, excellent signature properties, fire safety, good energy absorption, directional properties of the face sheets enabling optimized design and production of complex and smooth hydrodynamic surfaces [1].

Simple theories exist to predict bending deflections of low cost sandwich plates with a line load and specific support conditions [2]. Several studies were focused on the competing collapse mechanisms for simply supported sandwich beams with composite faces and a PVC foam core subjected to three point bending [2, 3]. Map of failure modes or collapse mechanism depending on the core thickness or materials with prediction of collapse loads was studied in [3].

Micromechanical analysis with experimental validation is used to construct parametric and probabilistic model. With this method the influence of randomness of the manufacturing process can be discarded in respect to the mechanical properties [4].

Numeric modeling and experimental test have been completed to prove effect of shear keys to improve stiffness and in plane shear strength properties of composite sandwich panels [1].

The problem considered is consisting of the following objectives: the mechanical properties of the sandwich structure (tensile strength, elongation at break, maximum stress at break) are subjected to maximization and the cost

of the materials subjected to minimization. The multicriteria optimization problem has been formulated and solved by applying multicriteria analysis techniques [5–8] and genetic algorithms [9–12].

The main goal of the current study is to develop a new composite material with optimal physical and mechanical properties.

2. EXPERIMENTAL

2.1. Preparation of GFRP for tensile test

The reinforcement fibres for glass fibre reinforcement plastics GFRP are supplied in fabrics/mats. In Chopped Strand Mat (CSM) the orientation of relatively short fibre strands (~60 mm) is random and the used binder agent is in form of powder or emulsion. Rowing mats are made of long fibre strands, arranged in bundles with little or no twist and joined in fabric form with stitching. To improve the resin flow properties in vacuum infusion process the CSM mats are used in combination of rowing mats or layer of polypropylene fibres which are stitched together.

The prepared GFRP laminates consisted of following materials:

- The three layers of balanced stitched biaxial roving mat 0°/90° (3 × 600 g/m²) reinforcement were used to prepare GFRP laminate with polyester resin (413-568) matrix by vacuum infusion process.
- To obtain the shear modulus of the GFRP laminate, the balanced stitched biaxial roving mat -45°/+45° (3 × 600 g/m²) reinforcement were used to prepare GFRP laminate with polyester resin (413-568) matrix by vacuum infusion process.
- The second laminate was prepared in vacuum infusion process. The polyester matrix resin 413-568 was reinforced with three layers of flow mat consisting of three layers of fibres: 450CSM/210PP/450CSM (in total 3 × 1110 g/m²).

*Corresponding author. Tel.: + 372-620-32-70; fax.: + 372-620-32-64.
E-mail address: Henrik.Herranen@tu.ee (H. Herranen)

After post-curing the laminates at the room temperature the rectangular tensile specimens according to ISO 527-4 (25 mm × 250 mm) were milled by 3D CNC milling machine.

2.2. Preparation of sandwich panels for 4-point bending test

Sandwich panel consists typically of two GFRP facings and a lightweight thicker core material. The most common core materials are structural foams and wood products. Foams based on polyvinyl-chloride (PVC), high-density polyethylene (HDPE), polyethylene-terephthalate (PET) polyurethane (PUR), polymethyl-methacrylate (PMI), and others. The most important mechanical properties of reinforcement filling materials are the compressive strength, shear modulus and shear strength at failure. Stiffness and strength increases with the density of core material (see Table 1). The used technique for specimens manufacturing was vacuum infusion. Firstly the mould was cleaned, and the vacuum tape was placed in the edges of the mould, then 2 layers of wax were applied and dried for polishing. The complete set of reinforcement plies (see Table 2) with core material were applied to the mould, the peel ply, vacuum and resin injection tubing with connectors and finally the vacuum film were placed on top mould and vacuum drawn. The resin was then transferred via piping/hoses from a container of premixed resin by the suction created by the vacuum. It is important that the gel time is sufficiently long so that the resin has time to infuse the whole mould before it gels.

Table 1. Material specification of the sandwich panel

Material	Mass of 1m ² , kg	Layer thickness, mm
Gelcoat GS	0.6	0.5
Flowmat 450/210/450	1.1	1.5
Biaxial 0/90, 600g	0.6	1.0
Flowmat 450/210/450	1.1	1.5
Core (PET 20 mm) 80 kg/m ³	1.60	20.0
Flowmat 450/210/450	1.1	1.5
Polyester resin	3.9	–
Total	10.0	26.0

The three different sandwich panels were manufactured according to materials specification in Table 1. The three different core materials were used (PET and HDPE having density of 80 kg/m³, PMI having density of 52 kg/m³).

2.3. Mechanical testing of composites

2.3.1. Tensile testing of GFRP laminate

The mechanical properties of experimentally manufactured sandwich composite materials were tested. Mechanical properties of the GFRP laminate are mainly defined by tensile strength of the material. The tensile strength of the composite materials strongly depends on

the adhesion strength between the matrix and reinforcement material. Tensile tests of composite plastic materials were performed according to standard EN ISO 527-4:2000. During this process the mechanical properties, such as tensile strength, elongation and modulus of elasticity were determined. Specimens for tensile tests were prepared according to EN ISO 527-4:2000 type 2 (rectangular without end tabs). The cross-sections of the specimens were measured with calibrated calliper gauge with measurement accuracy of 0.01 mm. The axial extensometer with the gauge length of 50 mm (travel +50 % to -10 %), was used to measure axial strain in the specimen. Servo hydraulic testing machine Instron 8800 was used to conduct the testing. Bluehill 2 software was used. The tensile tests were performed with loading rate 2 mm/min with a tolerance of ± 20 %.

2.3.2. Bending tests of sandwich panels

For testing the bending strength and stiffness of sandwich panels the 4-point bending test are typically used. The different types of sandwich composite panels are tested in 4-point bending conditions according to ASTM C393/C393M. 4-point bending tests were performed by using electro-mechanical testing system Instron 5866 (PV005688) equipped with the video extensometer and Bluehill software. The principal scheme of 4-point bending test is described in Fig. 1, where: P is the load, S is the distance between supports, L is the span. The span of the lower supports was 560 mm and upper supports 100 mm.

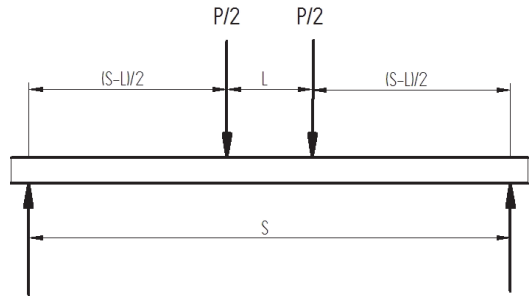


Fig. 1. Loading scheme in 4-point bending

2.4. Finite element model of sandwich panel

FEM procedures have been successfully employed in research studying the performance of composite structural sandwiches [13 – 15]. Generally a complex failure criterion is used to assess the performance of sandwich structure, e. g. Hou failure criteria [24] or Hashin failure criteria [25]. However, in this study von Mises stress in facings and shear stress in core are chosen to assess the strength of the sandwich. The end application of this development is not strength critical. Failure will not have catastrophic consequences.

Finite element analysis subjected to 4-point bending was conducted with ANSYS APDL v12.1 software. A plane strain 2D assumption was used. Parametric 2D elements with eight nodes (plane183) were chosen to model the sandwich test specimen [16]. Linear orthotropic material model was used to define laminate properties

(defined by elastic modulus E , Poisson's ratio ν and shear modulus G). Linear isotropic material model was used to define core properties (defined by elastic modulus E and Poisson's ratio ν). Mechanical properties of used core materials and GFRP facings and are presented in Table 2 and Table 3 respectively.

Table 2. Mechanical properties of core materials [18–21]

Core material	Thickness, mm	Density, kg/m ³	Compressive strength (perpendicular to the plane), MPa	Shear strength (parallel to the plane), MPa	Shear modulus (parallel to the plane), MPa
Atlas PUR F	20	60	0.6	0.55	6.5
Atlas PUR F	20	80	0.95	0.7	11
Atlas HDPE	20	100	1.3	0.9	17
Atlas HDPE	20	80	0.8	0.6	13
PET AC80	20	80	1.0	0.6	20
PMI 511G-F	20	52	0.9	0.8	19
PVC H60	20	60	0.9	0.76	20
PVC H80	20	80	1.4	1.15	27

2.5. Optimal design of sandwich panel

In order to improve mechanical properties of the sandwich structure the design optimization has been performed. The aim is to design the sandwich structure with maximum stiffness/strength properties while keeping minimal expenses. Behaviour of the different strength characteristics of the sandwich structure has been analyzed and the maximum stress was selected as optimality criterion i.e. the aim is to find out a configuration of the sandwich structure providing highest failure load. Certain similarity in behaviour of the stiffness/strength characteristics has been observed (proportional relations). An alternative concurrent optimality criterion is the cost of the sandwich structure.

Thus, the multicriteria optimization problem considered can be formulated as

$$F_1(\bar{x}) = \sigma_{\max} \rightarrow \max, \quad F_2(\bar{x}) = Cost \rightarrow \min, \quad (1)$$

subjected to linear constraints applied to the design variables vector \bar{x}

$$x_i \leq x_i^*, \quad -x_i \leq x_{i*}, \quad i = 1, \dots, n, \quad (2)$$

and non-linear constraints applied to the maximum deflection of the sandwich w_{\max} , maximum stresses of the each layer σ_k as

$$w_{\max}(\bar{x}) \leq w^*, \quad (3)$$

$$\sigma_k(\bar{x}) \leq \sigma_k^*. \quad (4)$$

In (2)–(4), the indexes * refer to the upper limit value of the corresponding variable.

The objectives (1) are normalized by taking use the following non-dimensional functions

$$f_1(\bar{x}) = \frac{\max F_1(\bar{x}) - F_1(\bar{x})}{\max F_1(\bar{x}) - \min F_1(\bar{x})}, \quad (5)$$

$$f_2(\bar{x}) = \frac{F_2(\bar{x}) - \min F_2(\bar{x})}{\max F_2(\bar{x}) - \min F_2(\bar{x})}. \quad (6)$$

Obviously, both concurrent objectives $f_1(\bar{x})$ and $f_2(\bar{x})$ are subjected to minimization and the Pareto optimality concept can be applied.

3. RESULTS AND DISCUSSION

3.1 Tensile test results

To determine the required mechanical properties of the laminates used in facings of sandwich material, the tensile tests were performed.

Elastic modulus was calculated according to standard ISO 527. Longitudinal elastic modulus E_x and transverse elastic modulus E_y , values were obtained from tensile tests (see Table 2 and Fig. 2).

As E-Glass fiber properties are similar in 0° and 90° directions, then $E_x = E_y$. Same idea is used for determining the E_z value for CSM. It was assumed to be 50 % of the polyester resin elastic modulus [17]. Poisson's ratios ν of facing materials were obtained from tensile tests (see Table 2).

Shear modulus (G) for E-Glass fiber was calculated according to standard ASTM D3518. E-Glass fiber shear modulus was obtained from tensile tests with $\pm 45^\circ$ test specimens. As fiber properties are same in x - and y -direction, then $G_{xz} = G_{yz}$. As CSM aligned with 45° fibers is not available, shear modulus was obtained from literature [22, 23].



Fig 2. Tensile test of the GFRP laminate

Table 3. Mechanical properties of GFRP laminates

E-Glass fibre 0°/90°, GPa		CSM, GPa	
E_x	19100	E_x	9400
E_y	19100	E_y	9400
E_z	1800	E_z	1800
ν_{xy}	0.11	ν_{xy}	0.26
ν_{yz}	0.30	ν_{yz}	0.33
ν_{xz}	0.30	ν_{xz}	0.33
G_{xy}	2900	G_{xy}	2200
G_{yz}	1600	G_{yz}	800
G_{xz}	1600	G_{xz}	800

Mechanical properties presented in the Table 2 are important data for performing virtual 2D bending tests with ANSYS software.

3.2. Bending test results

The flexural strength and stiffness of the three sandwich panels which had similar GFRP facings and different core materials (see Table 1) were determined. 4-point bending tests showed that the sandwich panel which had PMI foam core (see Table 4, Fig. 3) achieved best results as regards to stiffness.

Table 4. Average results of the 4-point bending test

Core material	Max force, kN	Global modulus of Elasticity, GPa	Deflection (mm)	Flexural stress, MPa
PET	2,1	2.4	48.2	17
HDPE	2.3	2.1	64.1	19
PMI	1.6	2.5	26.1	13

**Fig. 3.** Shear failure of sandwich panel with PMI core in 4-point bending test

The cost of PMI foam exceeds 5-times the cost of HDPE and PET foams. Thus, the second option for core material selection is PET foam having lower flexural stiffness, similar global modulus of elasticity and higher flexural strength than PMI. The cost of PMI foam exceeds 5-times the cost of HDPE and PET foams. Thus, the second option for core material selection is PET foam having lower flexural stiffness, similar global modulus of elasticity and higher flexural strength than PMI.

**Fig. 4.** Shear failure of sandwich panel with PET core in 4-point bending test

3.3. FEA model validation

For FEA model validation the results of 4-point bending tests and virtual testing have to be compared. As it follows from the Table 5 for the sandwich panels with PET and PMI foam the deflection rates obtained by real and virtual tests are quite similar differentiating only by 3 %–6 %, as the shear modulus of these foams (see Table 2) are in same range 19 MPa–20 MPa. Regarding the sandwich panel with HDPE foam (80 kg/m³) the deflection rate obtained by real testing is differing almost 40 % from virtual result. It can be explained by relatively low shear modulus (11 MPa) and buckling with plastic deformation of the tested panel.

Table 5. Comparison of the real and virtual 4-point bending test results

Type of core material	Maximal deflection obtained by testing, mm	Maximal deflection obtained by FEA, mm	Shear stress of the core material obtained by FEA, MPa
PET	34.2	32.0	0.97
HDPE	69.9	41.5	0.94
PMI	30.0	30.9	0.94

3.4. FEA analysis results

The sandwich materials were loaded with 2000 N force (1000 N per single loading nose). First support point had both horizontal and vertical directions fixed and second support had only vertical direction blocked. Meshing density was set to the element size with 1 mm edge length.

Von Mises stress distributions in facings are depicted in Fig. 5 and Fig. 6 respectively.

The values of the von Mises stress on lower facing are significantly higher than that in upper facing. The distribution of the xy-shear stress is depicted in Fig. 7.

After number of tests with nine core materials with different thicknesses (15, 18, 20 mm) combined with different number of biaxial reinforcement layers (1–6) in the GFRP laminate. It was noticed that all core and sheet material combinations had a failure occurring firstly in core due to shear stresses exceeding the limit value. The obtained FEA analysis results were used for optimal design of sandwich panel. The problem considered is consisting of

the following objectives: the mechanical properties of the sandwich structure (tensile strength, elongation at break, maximum stress at break) are subjected to maximization and the cost of the materials subjected to minimization. The material and production costs were calculated for each design of sandwich panel.

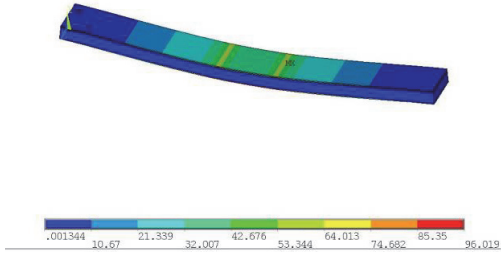


Fig. 5. Stress distribution in GFRP upper facing.

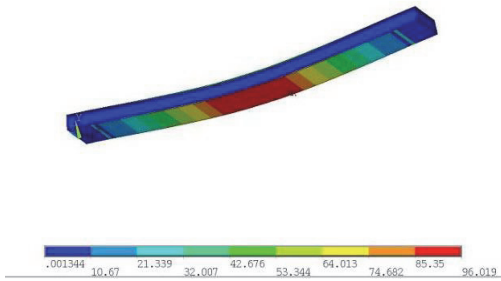


Fig. 6. Stress distribution in GFRP lower facing

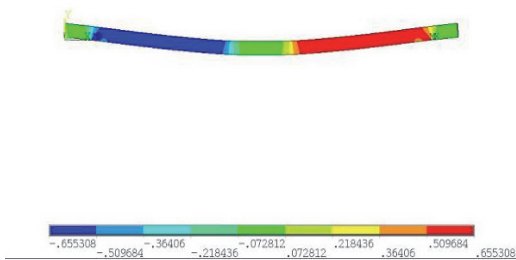


Fig. 7. Shear stresses in core material

3.5. Pareto frontier

Repetitive evaluation of the objective function $f_1(\bar{x})$ and nonlinear constraints (3)–(4) during optimization procedure is time consuming. For that reason, the FEA has been performed for fixed set of design variables and on the basis of obtained numerical results the response surface has been constructed (most commonly used technique to reduce the cost of the computational analysis and /or experimental tests). In the current study the artificial neural network (ANN) has been employed for response surface modeling. The surface constructed by the use of ANN does not normally contain the given response values (similarity with least-squares method in this respect). An approach proposed is based on the use of the MATLAB neural network toolbox (two layer network with one hidden

layer). The Pareto front of the maximum stress and cost of the sandwich structure is given in Fig. 8.

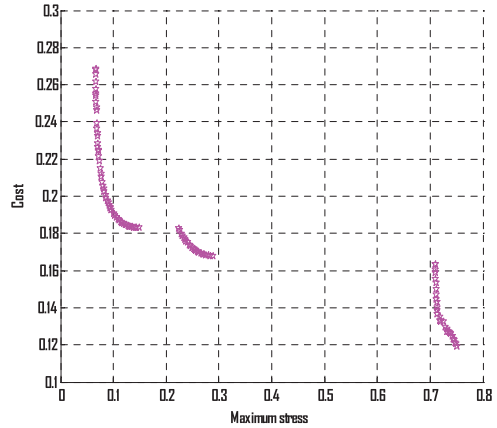


Fig. 8. Maximum stress vs cost of the sandwich structure

First note, that the minimum values of the objective function $f_1(\bar{x})$ in Pareto front correspond to maximum values of the original stress function $F_1(\bar{x})$ (see formulas (1), (5)). Pareto front depicted in Fig.8 contains discontinuities and is made up from three parts corresponding to sandwich structures with different values of the maximum stress and cost. Obviously, the Pareto front can be made less gradual by design of neural network model, but this is not the target desired. Main aim is to provide as much information as possible for decision making i.e. for selection optimal point on Pareto front. Points before sudden rise of the cost function seem most appropriate. However, all points in Pareto front are optimal (Pareto optimality) and final decision depends on particular case.

4. CONCLUSIONS

Optimal design of the light-weight sandwich panel has been performed. Different combinations of the core material and layer thicknesses are considered. The study involves experimental investigation and numerical simulation for determining mechanical properties of the layer materials of the sandwich structure. In order to reduce computational time the metamodeling technique has been employed (ANN). Finally, relying upon the obtained response surface the Pareto optimality concept is applied and optimal solutions are determined. It can be concluded that:

- the solution appears more sensitive with respect to core material selection than core layer thickness (it was assumed that the total thickness on the sandwich structure remains unchanged, i.e. core thickness can decrease with increasing facing layers thickness);
- the use of certain expensive core materials like PMI leads to sudden increase in cost, but does not provide significant improvement of the mechanical properties; thus in most of cases use of such core materials is not reasonable;

- the sensitivity of the solution with respect to design variables is times higher in points neighbouring the discontinuity points of the Pareto front.

In future studies, the sensitivity analysis needs special attention. Based on ANN model used, the closed form analytical expressions can be derived for computing the sensitivities with respect to design variables.

Acknowledgments

This study was supported by Estonian Science Foundation targeted financing project SF0140062s08 and Estonian Science Foundation grant ETF8485.

REFERENCES

1. **Mitra, N.** A Methodology for Improving Shear Performance of Marine Grade Sandwich Composites: Sandwich Composite Panel with Shear Key *Composite Structures* 92 (5) 2010: pp. 1065–1072.
2. **Glenn, C. E., Hyer, M. W.** Bending Behavior of Low-cost Sandwich Plates *Composites Part A Applied Science and Manufacturing* 36 (10) 2005: pp. 1449–1465.
3. **Steeves, C. A., Fleck, N. A.** Collapse Mechanisms of Sandwich Beams with Composite Faces and a Foam Core, Loaded in Three-point Bending. Part II: Experimental Investigation and Numerical Modeling *International Journal of Mechanical Sciences* 46 (4) 2004: pp. 585–608.
4. **Guilleminot, J., Comas-Cardona, S., Kondo, D., Binetruy, C., Krawczak, P.** Multiscale Modelling of the Composite Reinforced Foam Core of a 3D Sandwich Structure *Composites Science and Technology* 68 (7–8) 2008: pp. 1777–1786.
5. **Gerald, C. F., Wheatly, P. O.** Applied Numerical Analysis. Fifth edition. California Polytechnic State University, 1994.
6. **Rowe, M. D., Pierce, B. C.** Sensitivity of the Weighted Summation Decision Method to Incorrect Application *Socio-Economic Planning Sciences* 16 (4) 1982: pp. 173–177.
7. **Zeleny, M.** Compromise Programming. In: Multiple Criteria Decision Making. University of Southern Carolina Press, Columbia, 1973.
8. **Bassir, D. H., Zapico, J. L., Gonzales, M. P., Alonso, R.** Identification of a Spatial Linear Model Based on Earthquake-induced Data and Genetic Algorithm with Parallel Selection *International Journal of Simulation and Multidisciplinary Design Optimization* 1 2007: pp. 39–48.
9. **Pohlak, M., Majak, J., Eerme, M.** Optimization of Car Frontal Protection System *International Journal of Simulation and Multidisciplinary Design Optimization* 1 2007: pp. 31–38.
<http://dx.doi.org/10.1051/ijsmdo:2007004>
10. **Pohlak, M., Majak, J., Karjust, K., Küttner, R.** Multicriteria Optimization of Large Composite Parts *Composite Structures* 92 2010: pp. 2146–2152.
11. **Kers, J., Majak, J.** Modelling a New Composite from a Recycled GFRP *Mechanics of Composite Materials* 44 (6) 2008: pp. 623–632.
<http://dx.doi.org/10.1007/s11029-009-9050-4>
12. **Kers, J., Majak, J., Goljandin, D., Gregor, A., Malmstein, M., Vilsaar, K.** Extremes of Apparent and Tap Densities of Recovered GFRP Filler Materials *Composite Structures* 92 (9) 2010: pp. 2097–2101.
<http://dx.doi.org/10.1016/j.compstruct.2009.10.003>
13. **Borsellino, C., Calabrese, L., Valenza, A.** Experimental and Numerical Evaluation of Sandwich Composite Structures *Composites Science and Technology* 64 (10–11) 2004: pp. 1709–1715.
14. **Mines, R. A. W., Alias, A.** Numerical Simulation of the Progressive Collapse of Polymer Composite Sandwich Beams under Static Loading *Composites Part A: Applied Science and Manufacturing* 33 (1) 2002: pp. 11–26.
[http://dx.doi.org/10.1016/S1359-835X\(01\)00082-3](http://dx.doi.org/10.1016/S1359-835X(01)00082-3)
15. **Russo, A., Zuccarello, B.** Experimental and Numerical Evaluation of the Mechanical Behaviour of GFRP Sandwich Panels *Composite Structures* 81 (4) 2007: pp. 575–586.
<http://dx.doi.org/10.1016/j.compstruct.2006.10.007>
16. ANSYS, Inc. ANSYS 12.1 Manual, 2009.
17. Topplast AS, Product Datasheets <http://www.Topplast.ee>, 19.10.2011
18. Soteco Foam Technical Datasheet <http://www.Sotecospa.it/>, 19.10.2011.
19. Armacell Product Data Sheet: www.Armacell.com, 01.12.2010.
20. Rohacell Product Datasheet: www.Rohacell.com, 01.12.2010.
21. Divinycell H Manual: www.diabgroup.com, 01.12.2010.
22. Guidelines for Design of Wind Turbines. 2nd Edition. Det Norske Veritas, Copenhagen: Scanprint, 2009.
23. Military Handbook: Composite Materials Handbook – Polymer Matrix Composites Materials Usage, Design and Analysis. MIL-HDBK-17/3F (Vol. 3 of 5). U.S. Department of Defense, 2002 group.
24. **Hou, J. P., Petrinic, N., Rui, C., Hallett, C. R.** Prediction of Impact Damage in Composite Plates *Composite Science and Technology* 60 (2) 2000: pp. 228–273.
25. **Hashin, Z.** Failure Criteria for Unidirectional Fiber Composites *Journal of Applied Mechanics* 47 (2) 1980: pp. 329–334.

Presented at the 20th International Baltic Conference
"Materials Engineering 2011"
(Kaunas, Lithuania, October 27–28, 2011)

Paper II

H. Herranen, J. Kers, J. Preden, R. Talalaev, M. Eerme, J. Majak, M. Pohlak, H. Lend, G. Allikas, "Embedded Electronics Influence on the Strength of Carbon Fiber Laminate" in *Advanced Material Research, Trans Tech Publications*, vol. 905, pp.239-243, 2014.

Embedded Electronics Influence on the Strength of Carbon Fiber Laminate

Henrik Herranen^{1,a}, Jaan Kers^{2,b}, Jürjo S. Preden^{3,c}, Robert Talalaev^{2,d},
Martin Eerme^{1,e}, Jüri Majak^{1,f}, Henri Lend^{1,g}, Georg Allikas^{2,h}

¹Department of Machinery

²Department of Materials Engineering

³Department of Computer Control

^{1,2,3}Tallinn University of Technology, Ehitajate tee 5, 19086 Tallinn, Estonia

^ahenrik.herranen@ttu.ee, ^bjaan.kers@ttu.ee, ^cjurgo.preden@ttu.ee, ^drobert.talalaev@ttu.ee,
^emartin.eerme@ttu.ee, ^fjuri.majak@ttu.ee, ^ghenri.lend@ttu.ee, ^hgeorg.allikas@ttu.ee

Keywords: composite, embedded electronics, CFRP, structural health monitoring, FEM analysis.

Abstract. A complex electronics circuit placeholder is embedded in the carbon fiber laminate. The reduction of the material mechanical strength is assessed. The strain interaction between electronics and carbon fiber laminate is measured with digital image correlation based deformation scanner GOM ARAMIS 2M. A finite element analysis model is developed and validated. Based on FEA results the response model for prediction of the mechanical properties of laminate is introduced.

Introduction

Surface mounted sensors are susceptible to damage. Their protection from environment pays a weight penalty. Embedding the sensors allows for protection from adverse environmental conditions. In [1-6] the structural behavior of the composite laminate has been analyzed in the case, where a simple geometry sensor is embedded in the host structure. In [1] a field effect transistor is embedded in a structure and is tested to electronics functionality failure. In [2] 3-point bending and compression tests with embedded sensors are conducted. The performance of laminate with embedded sensors which interface to host structure is reinforced with interlacing is described in [3]. The mechanical behavior of laminates with simple piezoelectric actuators is analyzed in [5-6].

Current paper is focused on study of issues related to embedding complex geometry naked electronics circuits inside a carbon fiber composite. Paper consists of experimental study including testing of virgin structures, manufacturing of smart composite with embedded electronics, testing and examination of smart structures and development of numerical models.

Experimental study

Experimental study is concentrated to manufacturing, testing and examination of the smart composite structure obtained by embedding complex geometry naked electronics circuits inside a carbon fiber composite. The virgin structure has been tested as a reference structure.

Testing of Virgin Structure

The base material is GURIT supplied carbon fiber woven pre-preg fabric SE84 LV. The material was cured under 1bar vacuum in an oven at around 80°C according to supplier provided curing cycle. The laminate with 16 layers has been considered. The thickness of the laminate was approximately 3,5mm. The tensile, shear and compression testing were conducted according to ISO 527-4, ASTM D3518 and ASTM 6641 standards, respectively. The mechanical properties of virgin carbon fiber structure measured are shown in Table 1.

Table 1: Virgin laminate experimentally determined properties

Property	Value	Unit
Tensile strength $\sigma_x^t = \sigma_y^t$	625,65 ± 39,8	MPa
Maximum tensile strain $\varepsilon_x^t = \varepsilon_y^t$	0,987 ± 0,188	%
Compressive strength $\sigma_x^c = \sigma_y^c$	347 ± 16	MPa
Maximum compressive strain $\varepsilon_x^c = \varepsilon_y^c$	0,49 ± 0,097	%
Youngs modulus $E_x = E_y$	57,88 ± 28,2	GPa
Shear strength τ_{xy}	92,27 ± 4,74	MPa
Maximum shear strain γ_{xy}	4,74 ± 0,456	%
Shear modulus G_{xy}	7,065 ± 1,73	GPa

Manufacturing of the Specimens with Embedded Electronics

Printed circuit board (PCB) with low thickness and casing-less microchips was chosen for the electrons placeholder. The PCB is depicted in Figure 1 on the left. The height of the board was 0,6mm. The thickness with at the thickest point of PCB was 2,45mm. PCB was 22mm long and 15mm wide.

The PCB was placed longitudinally and transversely to the loading direction for tensile and compression testing. The printed circuit boards were placed in three configurations for shear testing: longitudinally, transversely and tilted at an angle of 45 degrees. The different angle of sensor placement was chosen in order to simulate the compatibility of node orientation with possible sensors that might be aligned in shear fiber locations. The chips were placed between the 8th and 9th layer to ensure that they were on the neutral axis. The tensile and compressive testing specimens failed similarly for the whole test lot: through gage zone occurred delamination crack which was followed by lateral crack on the curved surface side of the specimen. Single specimen from tensile testing had a pure delamination failure. Also in case of compressive specimens one specimen failed only through pure lateral crack. The results from mechanical testing are summarized in Table 2. The strength properties decreased averagely 14,9%. The highest reduction occurred in compressive strength properties. The compressive strength decreased 32,6%, tensile strength 14,7% and shear strength 3,3%, respectively. It is interesting to note that the maximum compressive strain and tensile strain increased 28,8% and tensile 35,9%, respectively.

Table 2: Mechanical properties of the specimens with embedded electronics

Property	Value	Unit	Change compared to virgin structure, %
PCB embedded longitudinally			
Tensile strength $\sigma_x^t = \sigma_y^t$	490,66±48,08	MPa	-21,6
Maximum tensile strain $\varepsilon_x^t = \varepsilon_y^t$	1,186±0,12	%	20,2
Compressive strength $\sigma_x^c = \sigma_y^c$	237,73±18,76	MPa	-31,5
Maximum compressive strain $\varepsilon_x^c = \varepsilon_y^c$	0,533±0,068	%	8,77
Shear strength τ_{xy}	85,58±	MPa	-7,3
Maximum shear strain γ_{xy}	4,25±1,11	%	-10,3
PCB embedded transversely			
Tensile strength $\sigma_x^t = \sigma_y^t$	576,44±11,84	MPa	-7,9
Maximum tensile strain $\varepsilon_x^t = \varepsilon_y^t$	1,496±0,03	%	51,6

Compressive strength $\sigma_x^c = \sigma_y^c$	229,85±39,49	MPa	-33,8
Maximum compressive strain $\varepsilon_x^c = \varepsilon_y^c$	0,730±0,40	%	48,9
Shear strength τ_{xy}	96,01±2,89	MPa	4,1
Maximum shear strain γ_{xy}	3,685±0,728	%	-22,3
PCB embedded at angle 45°			
Shear strength τ_{xy}	86,05±5,11	MPa	-6,7
Maximum shear strain γ_{xy}	4,998±0,01	%	5,4

During the measurement a loud sharp noise was noticed at these step points. It can be assumed that some electronic component had failed due to loading.

Numerical Modeling

In this section the FEA model is introduced and validated. The obtained results are discussed. An ANN model for prediction of the stiffness/strength properties is proposed.

Finite Element Analysis Model Development

A 2D plane stress finite element model was developed. The models strain information was compared with DIC scanning results. In the cross-section of the PCB the most space consuming parts are a surface acoustic wave (SAW) filter and the circuit board. SAW filter is the rectangular hollow object which is made of cap and bottom. SAW device consists of two materials: metallic cap and quartz wafer on to which the filter circuit is etched. Quartz is also known as silica and has chemical composition of SiO₂. The epoxy of resin-rich pocket is assumed to have the following properties: $E = 3,8\text{GPa}$, $\nu = 0,4$, $\sigma_t = 98\text{MPa}$ and $\sigma_c = 172\text{MPa}$. Only anisotropic material used in the finite element model is the carbon fiber laminate with orthotropic properties as measured on the virgin structure mentioned in Table 1. Two different geometries are simulated in ANSYS V14.0 software. First is the tensile/compression specimen with transversal orientation and second with longitudinal orientation, respectively. PCB cross-section was divided between copper and FR-4 layers. Mesh was refined at the resin rich pockets and singularities were avoided with the geometrical modification of the resin-pockets sharp edges to avoid spike-shaped contours. Minimum element side length which was used in the stress concentration areas near the edges of the resin pockets was 1 μm (0,001 mm). Both structures were analyzed with finite element method in tension and compression. Tensile specimens were loaded with tensile strain 0,6% which would create approximately tensile stress 350MPa in virgin structure. Compressive specimen simulation was loaded with compressive strain 0,5%.

The factor of safety distribution among the various materials is shown figure 1. The most critical zone in both specimen types is at the edges of the resin-rich pockets. SAW filter and resin interface have the highest stress concentration. On both snapshots in figure 9 of the rainbow diagram color values are equivalent. Therefore it is possible to compare the diagrams directly. It can be pointed out that the specimen with longitudinally oriented circuit has more red zones: the area in the resin pockets on the left and right side of the foreign object are bigger and the copper layers in the circuit board have deformed plastically. The source of the stress concentration is the stiffness and Poisson ratio mismatches of different materials in the specimens.

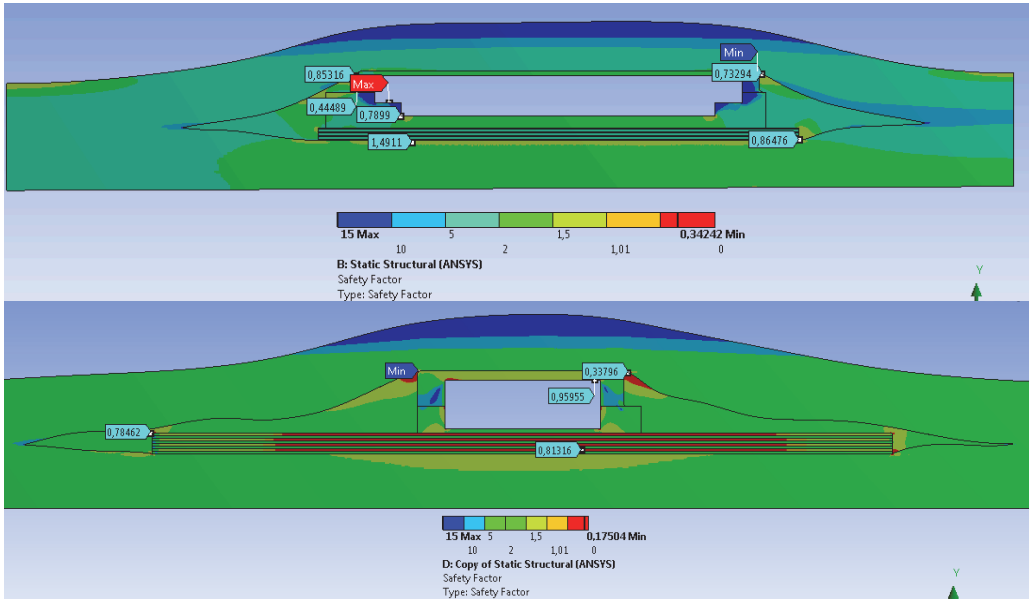


Figure 1: Factor of safety values in the cross-sections of tensile specimens

Finite Element Analysis Model Validation

The finite element analysis model was validated through comparison with the strains occurring on the surface of real specimen. Tensile testing had cracking occurring around 350MPa as sharp stiffness reduction steps. Compression testing validation value was set to be the maximum compressive stress of the weaker type (transversely placed PCB) specimen. The value used was 229MPa. In figures 2 are depicted snapshots of tensile strain field distribution surrounding the foreign object in case of tensile loading condition.

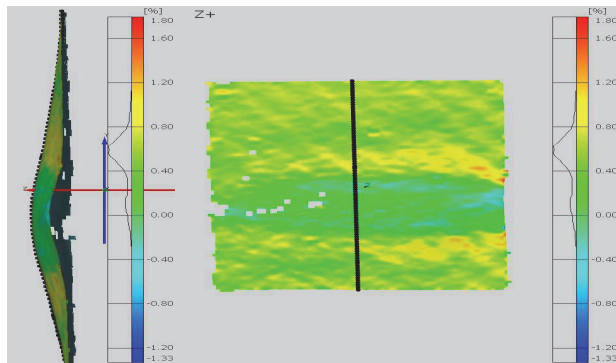


Figure 2: Tensile strain distribution on the surface of longitudinally placed PCB specimen at 359MPa tensile stress

The tensile testing specimens have high strain differences in the regions where SAW filter device ends and resin pockets start. The maximum difference occurs in the transverse placed PCB specimen at longitudinal coordinate $Y = 7\text{mm}$. The experimental strain value is 1,35% while the FE simulation value is 0,1%. This could be caused by the void bubbles near the edges of the SAW device. The compression results have maximum difference also in the transverse placed PCB

specimen at longitudinal coordinate $Y=21\text{mm}$. The experimental strain value is 0,35% while the FE simulation value is -0,05%. In both loading condition types the biggest differences between the simulation and experimental results are observed at the edges of the SAW device. The optimization algorithms include several iterations and the evaluation of objective functions is needed to perform in large number of points in design space. The numerical analysis is resource consuming independent on used methods (less or more for different methods [7-10]). For that reason in the following an ANN model is introduced for describing relation between stiffness/strength properties of the laminate and the location parameters of the embedded electronic component(s).

Summary

An experimental study on the fully embedded complex circuit placeholder inside carbon fiber laminate has been performed. The mechanical performance of the laminate with embedded system is examined. The most critical zones in the specimen are found to be the resin-rich pockets at the end of the circuit. The FEA model for simulating the behavior of the laminate with embedded electronics has been developed and validated against experimental data. In most simulation cases the resin-rich pockets were the first to fail the factor of safety test.

Acknowledgements

The work has been supported by Estonian Science Foundation grant ETF8485, ETF9441, targeted financing project SF0140035s12 and EU structural funds project “Smart composites - design and manufacturing“ 3.2.1101.12-0012.

References

- [1] Warkentin DJ, Crawley EF, Embedded, Proceedings of AIAA 32nd Conference on Structures, Structural Dynamics and Materials 1991, Baltimore, USA, p.1322
- [2] Kim KS, Breslauer M, Springer GS, Journal of Reinforced Plastics and Composites, Vol 11 (1992), p. 949
- [3] Sirkis JS, Singh H, Dasgupta A, Chang CC, Proceedings of the ADPA/AIAA/ASME/SPIE Conf. on Active Materials and Adaptive Structures 1992, Alexandria, USA, p. 563.
- [4] Hansen JP, Vizzini AJ, Journal of Intelligent Material System and Structures Vol.11 (2000), p.902
- [5] Mall S, Coleman JM, Smart Material Structures Vol. 7 (1998), p. 822
- [6] Paget CA, Levin K, Conference on Smart Structure and Integrated Systems 1999, Newport Beach, USA, Vol. 3668, p. 306
- [7] Majak J; Pohlak M; Eerme M; Velsker T, Mechanika, Vol 18(4) 2012, p. 453
- [8] Majak, J.; Pohlak, M.; Eerme, M.; Lepikult, T. Applied Mathematics and Computation, Vol. 211(2), (2009) p. 488
- [9] Majak, J.; Pohlak, M.; Eerme, M. Mechanics of Composite Materials, 45(6), (2009), p. 631
- [10] Pohlak, Meelis; Küttner, Rein; Majak, Jüri, Rapid Prototyping Journal, 11(5), (2005) p. 304

Advances in Applied Materials and Electronics Engineering III

10.4028/www.scientific.net/AMR.905

Embedded Electronics Influence on the Strength of Carbon Fiber Laminate

10.4028/www.scientific.net/AMR.905.239

Paper III

H. Herranen, G. Allikas, M. Eerme, K. Vene, T. Otto, A. Gregor, M. Kirs, K. Mädamürk, "Visualization of Strain Distribution Around The Edges of a Rectangular Foreign Object Inside The Woven Carbon Fibre Specimen" *Estonian Journal of Engineering*, vol. 18, no.3, pp. 279-287, 2012.

Visualization of strain distribution around the edges of a rectangular foreign object inside the woven carbon fibre specimen

Henrik Herranen^a, Georg Allikas^b, Martin Eerme^a, Karl Vene^a,
Tauno Otto^a, Andre Gregor^b, Maarjus Kirs^a and Karl Mädamürk^c

^a Department of Machinery, Tallinn University of Technology, Ehitajate tee 5, 19086 Tallinn, Estonia; henrik.herranen@ttu.ee

^b Department of Materials Engineering, Tallinn University of Technology, Ehitajate tee 5, 19086 Tallinn, Estonia

^c Department of Computer Control, Tallinn University of Technology, Ehitajate tee 5, 19086 Tallinn, Estonia

Received 19 June 2012, in revised form 23 July 2012

Abstract. The paper addresses the issue of embedding the rectangular printed circuit board (PCB) – the placeholder for a complex sensor system circuit – in the glass fibre laminate during the lamination. The change of the material mechanical properties due to the presence of foreign objects in the laminate is assessed by experimental testing through standardized methods ASTM D3039, ASTM D6641 and ASTM D3518. Local stress–strain relationship near the PCB in the out-of-plane direction of the specimen are monitored through the use of GOM ARAMIS 2M digital image correlation method scanner. Based on the scanned model, a finite element simulation is generated and validated.

Key words: composite, laminate embedded printed circuit board, carbon fibre, digital image correlation.

1. INTRODUCTION

Surface-mounted sensors are susceptible to damage and their protection form environment is often accompanied by noticeable extra weight increase. Embedding the sensors allows for protection from adverse environmental conditions. If high environment protection enclosures like IP67 are removed, a noticeable weight saving occurs. It is also the only means suitable for creating an autonomous structure with a smooth surface finish.

Estimation of the structure behaviour in the case when a simple geometry sensor is embedded in the host structure, has been analysed earlier [1-6]. In [1], a field effect transistor is embedded in a structure and is tested to electronics functionality failure. Main difference from the current article is the simplicity of the circuit and that the laminas have inclusions. In [2], limited tests (3-point bending and compression) with embedded sensors are conducted. Paper [3] describes the performance of a laminate with embedded sensors, which interface to host structure is reinforced with interlacing. Papers [5] and [6] handle the mechanical behaviour of a laminate with simple piezoelectric actuators.

This article describes the mechanical issues, related to embedding naked electronics circuits of complex geometry inside a carbon fibre composite. A finite element model is generated. It is validated through strain field comparison with the results of digital image correlation scanner GOM ARAMIS 2M.

2. EXPERIMENTAL SET-UP AND RESULTS

The base material is GURIT supplied carbon fibre woven pre-preg fabric with designation SE84 LV. The material was cured under 1 bar vacuum in an oven at around 80°C according to the supplier provided curing cycle. The fabric has surface density of 200 g/m². The number of lamina layers in the laminate is 16. The thickness of the laminate is 3.5 mm.

Host material was tested for in-plane properties only. Tensile testing was conducted according to ISO 527-4, shear testing according to ASTM D3518 and compression testing according to ASTM 6641. All three tests were conducted by using 10 identical specimens.

The virgin carbon fibre structure has in-plane properties as stated in Table 1. Directions x and y are equivalent.

For the electronics placeholder, an available printed circuit board with low thickness and casingless microchips was chosen. The PCB is depicted in Fig. 1. It is 22 mm long and 15 mm wide. The height of the board is 0.6 mm. The thickness at the widest section is 2.45 mm.

The circuit board was embedded in 5 specimens with orientation as shown in Fig. 2.

Table 1. Mechanical properties of the host laminate virgin structure

Property	Value	Unit
Tensile strength, $\sigma_x^t = \sigma_y^t$	625.65 ± 39.8	MPa
Maximum tensile strain, $\epsilon_x^t = \epsilon_y^t$	0.987 ± 0.188	%
Compressive strength, $\sigma_x^c = \sigma_y^c$	347 ± 16	MPa
Maximum compressive strain, $\epsilon_x^c = \epsilon_y^c$	0.49 ± 0.097	%
Youngs modulus, $E_x = E_y$	57.88 ± 28.2	GPa
Shear strength, τ_{xy}	92.27 ± 4.74	MPa
Maximum shear strain, γ_{xy}	4.74 ± 0.456	%
Shear modulus, G_{xy}	7.065 ± 1.73	GPa

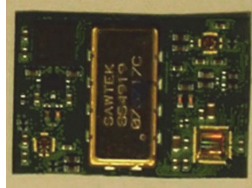


Fig. 1. Embedded electronics circuit.



Fig. 2. Orientation of the embedded circuit.

Chips were placed between the 8th and the 9th layer to ensure that they were on the neutral axis. Dipping the PCB-s inside acetone to remove any traces of dirt or grease was the only pre-treatment that was done before the lamination process. The material was fabricated on a glass plate to imitate a production mould that ensures a smooth continuous surface on one side. This formed a structure that has asymmetry in the z direction.

The specimens with embedded electronics were tested to failure with tensile, compressive and shear loads. The results are summarized in Table 2.

Compressive properties of the material were most affected: compressive strength was reduced by 31.5% and compressive strain by 66.8%

Table 2. Mechanical properties of the specimens with electronics

Property	Value	Unit	Change compared to virgin structure, %
Tensile strength, $\sigma_x^t = \sigma_y^t$	490.66 ± 48.08	MPa	-21.6
Maximum tensile strain, $\varepsilon_x^t = \varepsilon_y^t$	1.186 ± 0.12	%	16.8
Compressive strength, $\sigma_x^c = \sigma_y^c$	237.73 ± 18.76	MPa	-31.5
Maximum compressive strain, $\varepsilon_x^c = \varepsilon_y^c$	0.491 ± 0.149	%	-66.8
Shear strength, τ_{xy}	85.58 ± 11.4	MPa	-7.3
Maximum shear strain, γ_{xy}	4.25 ± 1.11	%	-10.3

3. FINITE ELEMENT MODEL

A 2D plane stress finite element model is constructed using software ANSYS V14.0. The CAD geometry was directly derived from pictures of the microscope (Figs 3 and 4). The scale was determined based on the microscope scale ruler on the original pictures and was double-checked, based on the measurements made earlier on the electronics board (length, width, thickness of the PCB board, height of the surface acoustic wave device). Simulation model mesh is depicted in Fig. 5. It has 32 032 elements.

In the cross-section of the PCB, the most space consuming parts are the surface acoustic wave (SAW) filter and the circuit board. The SAW device consists of two materials: steel cap and quartz wafer onto which the filter circuit is etched. The mechanical properties of used materials are listed in Table 3. The properties of electronics are derived from literature. The printed circuit board is composed of copper layers and of glassfibre/epoxy composite FR-4. FR-4 properties are taken from [7,8]. Quartz and copper are both taken from [1].

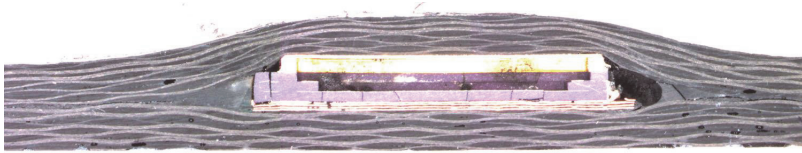


Fig. 3. Cross-sectional view of the specimen after failure.



Fig. 4. Constructed finite element model.

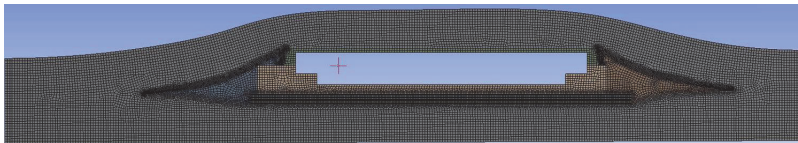


Fig. 5. The mesh of the model had 32 032 elements with refinements at the edges of the interfaces of the materials.

Table 3. Mechanical properties of materials used in simulation

Material	Material model	Elasticity properties	Strength properties
Quartz	Isotropic, linear	$E = 7 \text{ GPa}, \nu = 0.17$	$\sigma_t = 100 \text{ MPa},$ $\sigma_c = 1100 \text{ MPa}$
Steel	Isotropic, bilinear kinematic hardening	$E = 200 \text{ GPa}, \nu = 0.3,$ $E_{\text{tangent}} = 40 \text{ GPa}$	$\sigma_{\text{yield}} = 250 \text{ MPa},$ $\sigma_u = 510 \text{ MPa}$
Copper	Isotropic, bilinear kinematic hardening	$E = 130 \text{ GPa}, \nu = 0.34,$ $E_{\text{tangent}} = 25 \text{ GPa}$	$\sigma_y = 45 \text{ MPa},$ $\sigma_u = 210 \text{ MPa}$
FR-4 glassfibre laminate	Isotropic, linear	$E = 20 \text{ GPa}, \nu = 0.20$	$\sigma_t = 345 \text{ MPa},$ $\sigma_c = 415 \text{ MPa}$
Epoxy resin	Isotropic, linear	$E = 3.8 \text{ GPa}, \nu = 0.4$	$\sigma_t = 98 \text{ MPa},$ $\sigma_c = 172 \text{ MPa}$

The only anisotropic material in the finite element model is the carbon fibre laminate with orthotropic properties as measured on the virgin structure, mentioned in Table 1.

Virtual model of the specimen cross-section was loaded with 0.6% strain. At this strain level a loud cracking sound occurred, which indicates the structural failure of some embedded circuit board components. At this point the average stress in the tensile specimen is 353 MPa. Simulation results are depicted in Figs 6 and 7. The stress distribution in the cross-section of the specimen is shown in Fig. 6. Highest stress levels occur at the edges of the steel cap and under the printed circuit board. From these points the failure is initiated.

The factor of safety for materials, based on their ultimate strength, is plotted in Fig. 7. The lowest values are at the edges of the steel cap, quartz wafer and ends of PCB. Therefore the lowest strength in this application occurs in the region where the high-stiffness steel cap is adhered to the carbon fibre laminate.

4. VALIDATION OF THE FINITE ELEMENT MODEL

The finite element model is validated through the comparison with digital image correlation scanner results. The surface strains of the specimens were measured with a digital image correlation system (DIC) GOM ARAMIS 2M. The measuring volume was set to $35 \times 25 \text{ mm}$. Project parameters are as follows: the computational size is set to 3, validity quote 55%, the calculation method is set to total strain method and computation type is set to plane stress. Scanner data is taken from the stage, where tensile strain is 0.6% (equals to 32080 N tensile force and 353 MPa tensile stress). The tensile strain distribution on the curved surface of the specimen is depicted in Fig. 8.

The FEM top surface strain distribution is compared with the DIC scanner data in Fig. 9. The curves of strain distributions are close to each other, with strain difference 0.35% at the even surface (between longitudinal coordinates 10 to 20 mm). In physical specimens the tensile strains are higher up to 1.0%.

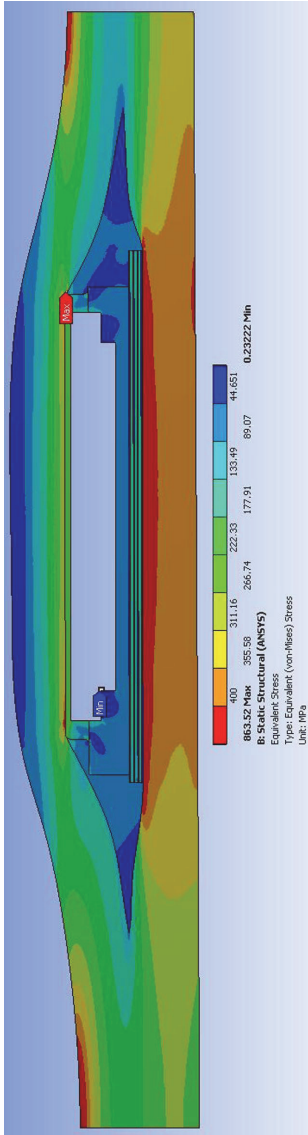


Fig. 6. Von Mises stress distribution in the specimen.

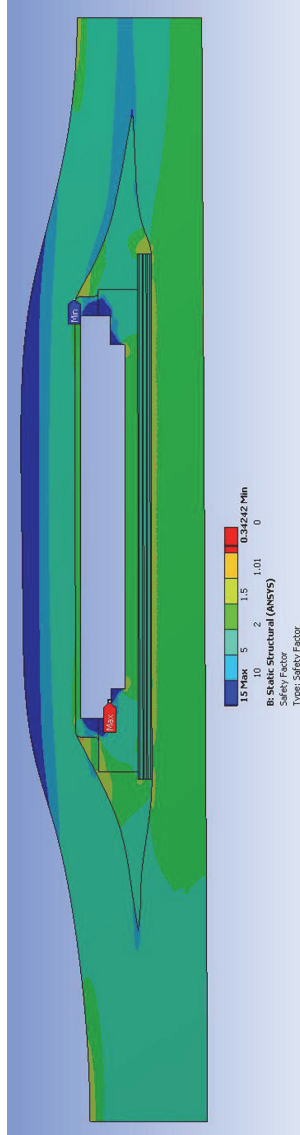


Fig. 7. Factor of safety of the materials.

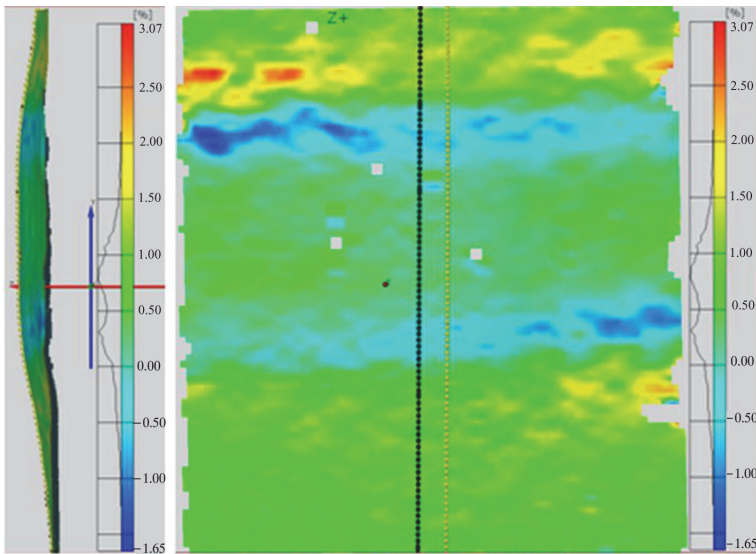


Fig. 8. Tensile strain distribution on the surface of the transversely placed PCB specimen, measured with the digital image correlation scanner. The black vertical line shows the location of the section where the strain is compared with the FEM model results.

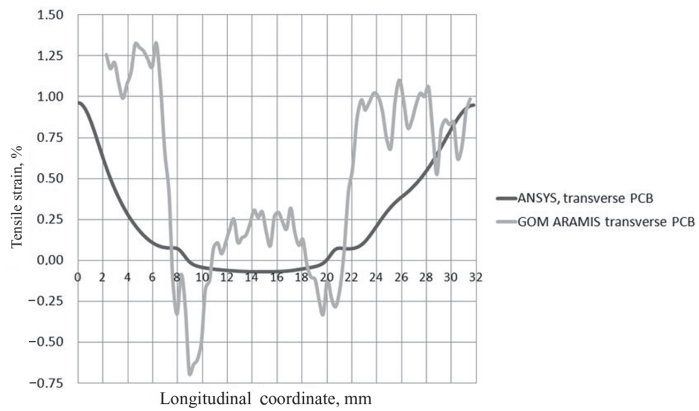


Fig. 9. Comparison of the tensile strain distributions.

This can be explained by the impurities, located at the edges of the SAW device. One such example is seen in Fig. 3 as a void or air bubble at the edge of the steel

cap. Waviness of the DIC measured strain distribution is probably caused by the weaving pattern of the fabric. The FEM model uses homogenized material for the composite laminate, which has much more smoother strain distribution.

5. CONCLUSIONS

A finite element method simulation was made in order to investigate the inner stresses of a composite structure with embedded electronics. The simulation was validated with tensile strain data from experimental testing. The strain distribution shows good correlation, which is influenced strongly by the impurities of the real material. Failure of the whole structure starts from the mismatch of the stiffness properties between steel and the composite material. This creates stress concentration that reduces the mechanical properties of the host material up to 32% of ultimate compressive strength. Future research direction would be the development of a suitable casing and multicriteria optimization procedure, like in [9,10] for optimizing the host structure and electronics to smoothen the stress gradients. The interaction between the host structure and the electronics can be influenced by multiple variables such as thickness of the electronics, thickness of the laminate, orientation of the laminas, geometrical shape of the electronics, etc.

REFERENCES

1. Warkentin, D. J. and Crawley, E. F. Embedded electronics for intelligent structures. In *Proc. AIAA 32nd Conference on Structures, Structural Dynamics and Materials*. Baltimore, 1991. AIAA Paper, AIAA-91-1084CP, 1991, 1322–1331.
2. Kim, K. S., Breslauer, M. and Springer, G. S. The effect of embedded sensors on the strength of composite laminates. *J. Reinforced Plastics Composites*, 1992, **11**, 949–958.
3. Sirkis, J. S., Singh, H., Dasgupta, A. and Chang, C. C. Experimental determination of damage and interaction strain fields near active and passive inclusions embedded in laminated composite materials. In *Proc. ADPA/AIAA/ASME/SPIE Conference on Active Materials and Adaptive Structures*. Alexandria, USA, 1992, 563–566.
4. Hansen, J. P. and Vizzini, A. J. Fatigue response of a host structure with interlaced embedded devices. *J. Intelligent Mater. Syst. Struct.*, 2000, **11**, 902–909.
5. Mall, S. and Coleman, J. M. Monotonic and fatigue loading behavior of quasi-isotropic graphite/epoxy laminate embedded with piezoelectric sensor. *Smart Mater. Struct.*, 1998, **7**, 822–832.
6. Paget, C. A. and Levin, K. Structural integrity of composites with embedded piezoelectric ceramic transducer. In *Proc. SPIE Conference on Smart Structure and Integrated Systems*. Newport Beach, California, 1999, SPIE 3668, 306–312.
7. Acculam Epoxyglas G10/FR4. *IDES Prospector*. IDES Inc., 2012. http://prospector.ides.com/DataView.aspx?I=34&TAB=DV_DS&E=112876&SKEY=34.986842.50872380%3A9a0ec215-bdfc-41a9-86ea-7110135e126e&CULTURE=en-US
8. Arlon 45N properties. *IDES Prospector*. IDES Inc., 2012. http://prospector.ides.com/DataView.aspx?I=34&TAB=DV_DS&E=120891&SKEY=34.986842.50872380%3A9a0ec215-bdfc-41a9-86ea-7110135e126e&CULTURE=en-US
9. Pohlak, M., Karjust, K. and Küttner, R. Multi-criteria optimization of large composite parts. *Composite Struct.*, 2010, **92**, 2146–2152.

10. Pohlak, M. and Majak, J. Optimal material orientation of linear and non-linear elastic 3D anisotropic materials. *Meccanica*, 2010, **45**, 671–680.

Suhteliste deformatsioonide visualiseerimine süsinikkiudkomposiidis neljakandilise objekti ümbruses

Henrik Herranen, Georg Allikas, Martin Eerme, Karl Vene, Tauno Otto,
Andre Gregor, Maarjus Kirs ja Karl Mädamürk

On uuritud pingeaotust süsinikkomposiidist katsekeha ristlõikes, millesse on integreeritud õhuke elektroonika trükkplaat. Pingete kontsentratsiooni analüüsitakse, kasutades lõplike elementide meetodi tarkvara ANSYS V14.0. Simulatsiooni korrektsust kontrollitakse tulemuste võrdlemisega digitaalse pildi korrelatsiooniskanneri GOM ARAMIS 2M abil määratud tõmbedeformatsioonidega. Simulatsioonist selgub, et kõige tugevamini mõjutavad komposiitmaterjali sinna lamineeritud jäigad metalsed kehad. Skaneerimise andmeid mõjutavad kõige enam pooride olemasolu ja süsiniklaminaadi kiududest tingitud mikrotaseme mitteisotroopsus.

Paper IV

H. Herranen, T. Saar, R. Gordon, M. Pohlak, H. Lend, "Durability Performance Of Semiconductor Strain Gauges In GFRP Laminate," in *Proceedings of 6th ECCOMAS Thematic Conference on Smart Structures and Materials (SMART2013)*, 2013.

DURABILITY PERFORMANCE OF SEMICONDUCTOR STRAIN GAUGES IN GFRP LAMINATE

Henrik Herranen^{*}, Tõnis Saar[†], Rauno Gordon[‡], Meelis Pohlak^{*}, Henri Lend^{*}

^{*}Tallinn University of Technology
Department of Machinery
Ehitajate tee 5
19086, Tallinn, Estonia
e-mail: henrik.herranen@ttu.ee, web page: <http://www.ttu.ee>

[†]ELIKO - Competence Centre in Electronics-,
Info- and Communication Technologies
Mäealuse 2/1
12618, Tallinn, Estonia
e-mail: tonis.saar@eliko.ee web page: www.eliko.ee

[‡]Tallinn University of Technology
Thomas Johann Seebeck Department of Electronics
Ehitajate tee 5
19086, Tallinn, Estonia
e-mail: rauno@elin.ttu.ee, web page: <http://www.ttu.ee>

Key words: Silicon strain gauge, Embedded sensor, Hygrothermal conditions.

Summary. *Semiconductor strain gauges have good potential for embedded structural health monitoring (SHM) applications. Silicon mechanical and thermal properties are similar to glass fiber. In this paper the high cycle loading of specimens with embedded and surface mounted semiconductor strain gauges is conducted. The base material is glass fiber laminate. Two different matrixes are used: polyester and epoxy resins. Hygrothermal loading is introduced to weaken the sensor-matrix interface and to imitate real application conditions.*

1 INTRODUCTION

Strain sensitive characteristic dependability from local defects has been often utilized to identify damage in structures [1]. Semiconductor strain gauges have good potential for embedded structural health monitoring (SHM) applications. The sensors usually have rectangular thin bar shape, with thickness around tenths of millimeter. The shape similarity to fibers and material similarity to glass fibers make this sensor appealing to composite SHM. The proportions of the sensor are close to the typical fiber: length dimension is magnitude

higher than width or thickness.

The semiconductor strain gauges have high piezoresistivity. The resistance change occurs in all conditions of static and dynamic strain. The gauge factor for semiconductor strain gauges are 50...60 times higher compared to metallic foil gauges [2]. This removes the necessity to use high gain voltage amplifier associated with metallic strain gauges.

The main advantage of semiconductor strain gauge is its high fatigue life. Since the gages are single-crystal elements, they have no measurable hysteresis or creep. This makes them attractive for long-term installations or for use in unique transducer applications.

Distributed wireless sensor node networks are good example where to apply the semiconductor strain gauges [3]. Nodes are able to measure the temperature locally near the strain sensors. This allows to the compensation of the non-linear behavior of the strain sensor. This article research topic is fatigue testing of fully embedded semiconductor strain gauges in order to check their potential in embedded structural health monitoring system applications. In the testing procedure two different composite materials are used. Different matrixes were used for specimen manufacturing: vinylester and epoxy resins. Epoxy resins have very high adhesion properties while vinylesters are widely used medium cost polymers for wind turbine and seaborne industries.

Hygrothermal conditioning is used to imitate the real application conditions. It is known, that moisture attacks the material interface between semiconductor and matrix [4,5]. Vinylester has a magnitude lower interfacial strength than epoxy. It is also more susceptible to damage caused by humidity [5].

The further challenge is to improve aging performance of the composite structure with embedded components. Thus, special attention should be paid on optimal design of composite materials and structures [6-8]. The global optimization and meta-modeling techniques can be combined in order to overcome complexities related with design of real world structures [9-11]. Different simplifications, including reduced order models, etc can be employed [12-13].

2 MATERIALS AND PREPARATION

The laminate had two types of setups. The reinforcement was the same for each type, but the matrixes were chosen different. The reinforcing fabric is biaxial 0°/90° non-crimp type glass fiber with surface density 600g/m². The matrix resins were epoxy LARIT L285 with hardener L286 and vinylester resin ATLAC 580 ACT with hardener Butanox M50 (3% volume fraction of resin). The mechanical properties of the laminates are depicted in Table 1. For the sake of simplicity the mechanical properties of both materials are set the same for current testing. The epoxy resin based laminate has 8 symmetric layers and total thickness of 4,5mm. Vinylester has 12 layers and total thickness of 7,5mm. Materials are made with vacuum bagging at room temperature and post-cured at 60°C for 16 hours.

The specimens were cut-out from workpiece with high speed milling machine at 32000 RPM with low feed rat in order to minimize the specimen edge delamination probability.

E_x, E_y	20GPa
E_z	5GPa
ν_{xy}	0,26
ν_{yz}	0,01
ν_{xz}	0,01
G_{xy}	2,9GPa
G_{xz}	1,6GPa
G_{yz}	

Table 1 : Mechanical properties of GFRP laminate

From each type of material two specimens are made. One specimen is tested as virgin material and the other is tested after environmental conditioning. For environmental conditioning the specimens were held at 60°C for 9 days (216 hours) in seawater filled chamber. The salinity was chosen to be 30‰.

In all specimens 6 silicon resistance strain gauges were embedded under the first layer. Three are on one side and three on the other side of specimen. The silicon strain gauges are sensitive to temperature variations. Therefore a thermistor from Vishay was adhered to the surface of the specimens. The strain gauges are naked type semiconductor strain gauges made by BCM Sensor Technologies Ltd. The properties of both sensors are given in Table 2 and Table 3.

Semiconductor strain gauges	SN5-1000-3.8-P-2	SN5-1000-5-P-2
Internal resistance	1000Ω	1000Ω
Gauge factor	150 ± 5%	150 ± 5%
Temperature factor of resistance	0,4%/°C	0,4%/°C
Temperature coefficient of gauge factor	0,3%/°C	0,3%/°C
Dimensions	5mm x 0,24mm x 0,03mm	3,8mm x 0,2mm x 0,03mm

Table 2 : Properties of used semiconductor strain gauges

Thermistor	NTCLE100E3332JB0
Internal resistance	3300Ω
Beta value	3977K
Operating range	-40°C...+125°C
Tolerance	5%

Table 3 : Properties of used thermistor



Figure 1: Vinylester specimen during wire soldering process

Data acquisition was conducted with National Instruments Daqpad-6259 and for supply voltage a precision voltage supply was used. The measuring procedure was conducted with simple voltage divider circuit, where one element is the semiconductor strain gauge and the other $1k\Omega$ resistor with 1% accuracy resistance value.

3 METHOD

The performance of embedded semiconductor strain gauges was estimated using fatigue testing similar to the ASTM E1949 standard. This standard describes the experimental measurement procedure of the fatigue performance of the metallic foil resistance strain gauges. The shape of specimen was developed similarly to ASTM E251 standard. A cantilever constant stress body with linearly decreasing cross-section was developed based on a requirement to maximize the uniformity of longitudinal strain field distributions. The cyclical load to be applied had $R = -1$ ratio value. If the body is loaded with point load vector at free end then for the stress uniformity it is vital to decrease sectional modulus of body according to the variation of bending moment along the span of body. For composite material it is difficult to design linearly variable thickness t since to material is created ply-wise with discrete thicknesses. The only feasible variable can be the width of the beam b . Therefore the width becomes a function of longitudinal coordinate X :

$$b(X) = KX \quad (t = \text{const}) \quad (1)$$

The stresses at cross-section are constant:

$$\sigma(X) = \frac{6FX}{KXt^2} = \frac{6F}{Kt^2} = \text{const} \quad (2)$$

And in case of isotropy the strain ϵ also would be constant:

$$\varepsilon(X) = \frac{6F}{EKt^2} = \text{const.} \quad (3)$$

Based on the strain equation (3) the aspect ratio K was calculated to achieve strain value of 0,55%. The strain value is roughly equal to the glassfiber laminate tensile strain limit divided by factor of safety value of four. Additionally it is near the semiconductor fatigue strain limit $500\mu\epsilon$ at which the sensors should have life expectancy of $2 \cdot 10^6$ [14].

The design parameters were constrained in the ranges as summarized in Table 4.

Parameter	Value range
Thickness	4mm to 8mm
Length	150mm to 250mm
Width	100mm to 300mm
Deflection	5mm to 40mm
Bending force	150N to 670N

Table 4 : Properties of used thermistor

The parameters were determined based on the testing machine geometrical limits and thickness was constrained in the range in which are marine laminates average properties. The testing machine was a chosen to be heavy duty machining centre with the fly cutter holder.

The analytical calculation was numerically verified with ANSYS Workbench V14.0. The used body was generated as shell-type geometry and orthotropic material properties were determined (see Table 1). First results showed that the free edge shear stresses concentration and the bolt hole structure at the free end cause perturbations in the uniformity of laminate surface major strain values. In Workbench Design of Experiments module response surface was created to find sufficiently uniform stress field. The longitudinal strain gradients values difference minimization was set as design criteria. The optimal shape of laminate was searched in the near region of the preliminary designed laminate. The most suitable body layouts for both materials are depicted on Figure 2 and Figure 3. Mechanical testing of one specimen ins depicted on figure 4.

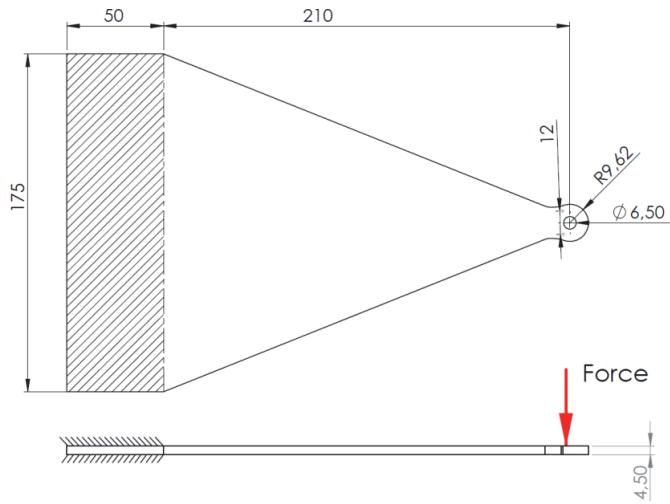


Figure 2: Constant stress body with epoxy resin

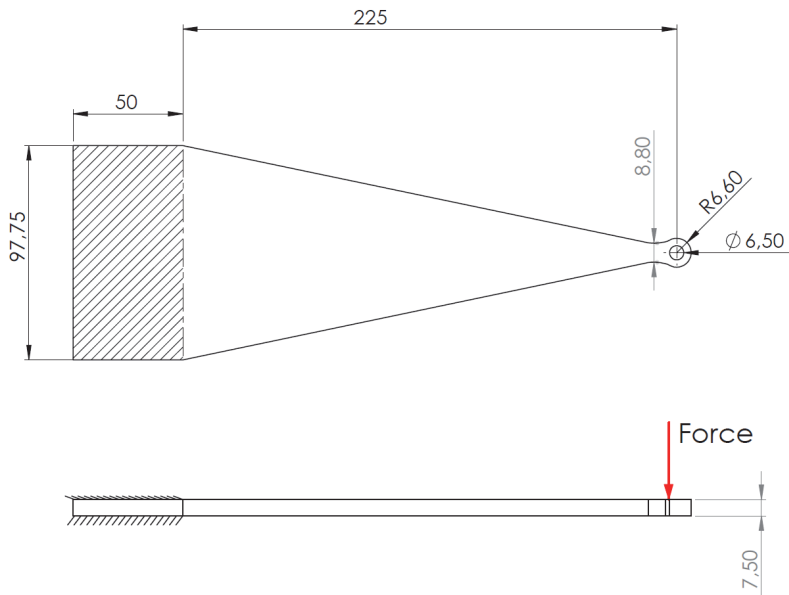


Figure 3: Constant stress body with vinylester resin

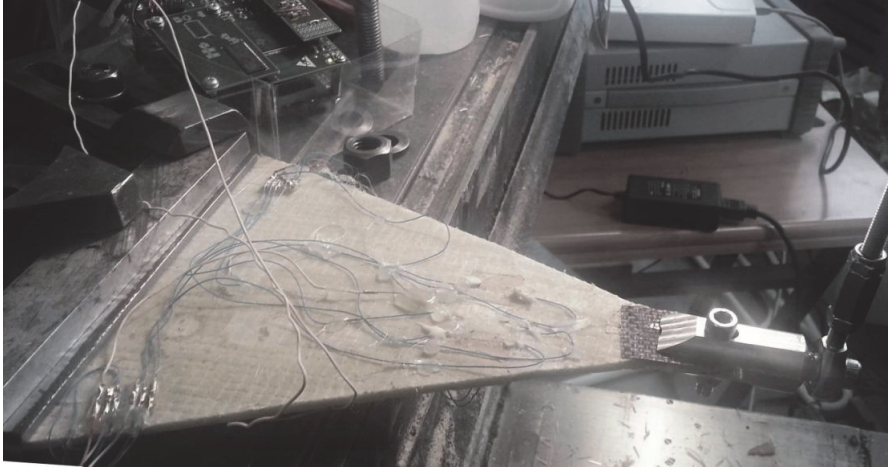


Figure 4: Hygrothermally conditioned epoxy specimen in fatigue bench

Sufficient uniformity of longitudinal strain values are depicted on Figure 5 and for transverse strain on Figure 6. Transverse strains uniformity is important because strain gauges have small transverse strain sensitivity. The location of semiconductor strain gauges is noted on Figure 5.

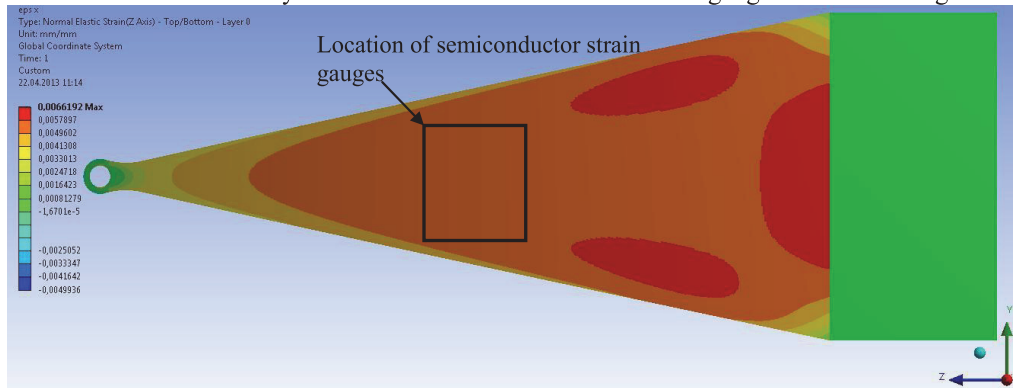


Figure 5: Longitudinal strain contour plot

Figure 6: Transverse strain contour plot

4 RESULTS

Fabrication process damaged most of the sensors. Probably resin application process with hand tools deformed some of the sensors until failure. At least 6 sensors were damaged during

soldering process: the junctions protruding from composite surface were difficult to solder because their melting point was low at 215°C and the diameter of the wire was extremely small – any mechanical tension broke the junction off. In virgin non-damaged structures epoxy resin type specimen had two working sensors left and in vinylester specimen 4 sensors. The environmental conditioned specimens were not separately measured before the conditioning. After the salt water bathing two sensors were functional in epoxy specimen and only one in vinylester. The cause of failure for these sensors might have been moisture expansion combined. In vinylester type specimens copper extension wires laminated under the first layer were severely corroded. Therefore it is concluded that at this salinity level direct seawater access through sufficient cracking near the sensors will damage the electronics through corrosion. Also the strain sensor polymer contact adhesive had a darkening change of color.

The fatigue life of the sensors is summarized in Table 5. It is interesting to note that the sensors did not have any sensitivity declination or hypersensitivity occurrence until failure. Also the temperature increase due to mechanical strains was negligible. The temperature curves were constant and had no correlation with the change of the excitation speed. The average environmental temperature was 26,6°C.

Epoxy virgin					
Cycles/min	200	400			
Cycles count, N	10970	124306			
Strain value, %	0,24	0,24			
Vinylester virgin					
Cycles/min	800	560	560	560	560
Cycles count, N	85200	91920	203080	368700	384800
Strain value, %	0,019	0,123	0,123	0,172	0,262
Epoxy damaged					
Cycles/min	800	800	800		
Cycles count, N	153698	318938	357818		
Strain value, %	0,066	0,121	0,15		
Vinylester damaged					
Cycles/min	800				
Cycles count, N	8465				
Strain value, %	0,0643				

Table 5 : Loading history of sensors

The epoxy resin specimen was tested first. The designed deformation value was too high: first sensor failed at 0,45% after 1800 cycles. The second failed after $8 \cdot 10^5$ cycles. This is far away from the strength limit of the sensor at $6000\mu\epsilon$ and also below at the fatigue strength value of

500 $\mu\epsilon$ [14]. After the first specimen the other were loaded stepwise with stroke length values 10, 20, 30 and 40mm. The loading history of specimens is depicted on **Error! Reference source not found.**. The fatigue breakdown is described with chart in Figure 7. It is obvious that despite the low amount of sensors the fatigue life is severely shortened with environmental conditioning. Epoxy resin specimen fatigue performance is difficult to analyze since the first virgin structure loading was not progressively conducted. From the epoxy resin fatigue results can be concluded that the breakdown strain value will be decreased from virgin structure 0,22% and 0,26% to 0,06% and 0,15%. From vinylester testing results is difficult to estimate the sensor strength reduction values because damaged specimen had only one operational sensor left. Nevertheless it is evident that the virgin structure strength is decreased from 0,17% and 0,26% to 0,065%.

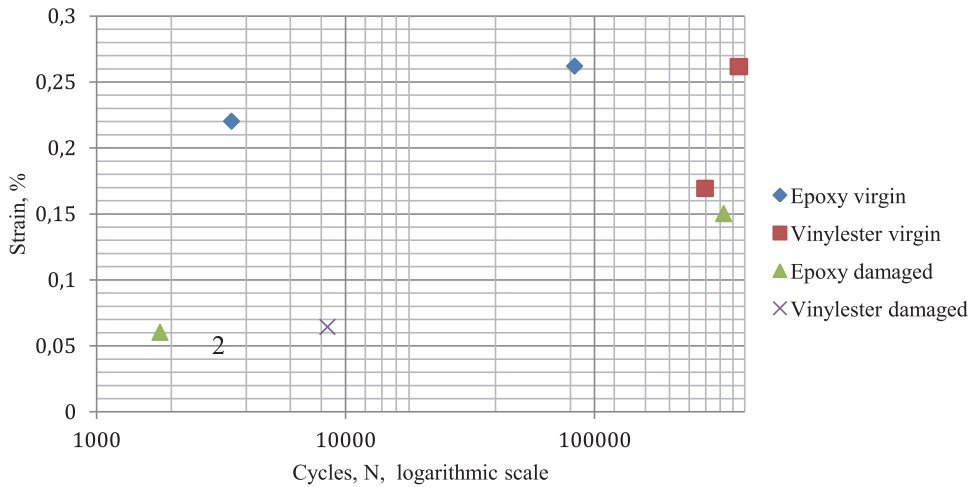


Figure 7: Sensor fatigue breakdown

The breakdown of sensors is probably caused by the separation of one contact from the surface of the sensor. This is estimated based on the fact that the sensors stopped working normally in tension mode, but restored electrical circuit continuity in compression mode (see Figure 8).

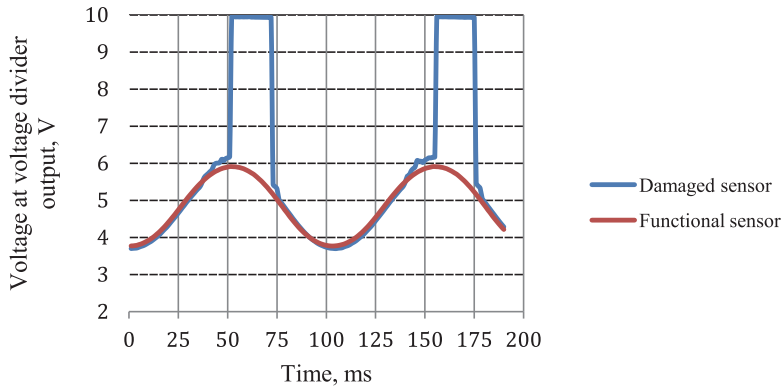


Figure 8: Sinus signal shape change due to loss of electrical contact(matched from two measurings)

The breakdown in most cases did not start as a abrupt change, instead the shape of sine curve at the peak strain values lost its smoothness at first(see Figure 9) and progressively the shape of sine function was totally lost.

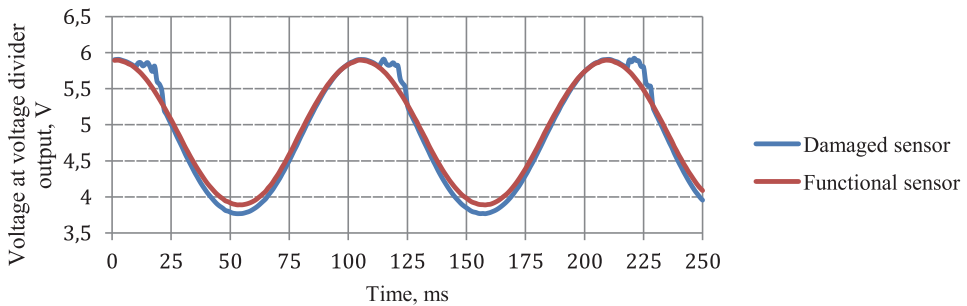


Figure 9: Abruption of sine function continuity – the first sign of sensor failure

After mechanical testing the strain gauges were examined. On the aged specimens some of the electrodes had corrosion signs. The glue that originally joined the golden electrode to the silicon has corrosion signs. Two edges of the same sensor are compared on the Figure 10 and Figure 11. This specimen was made of epoxy resin.

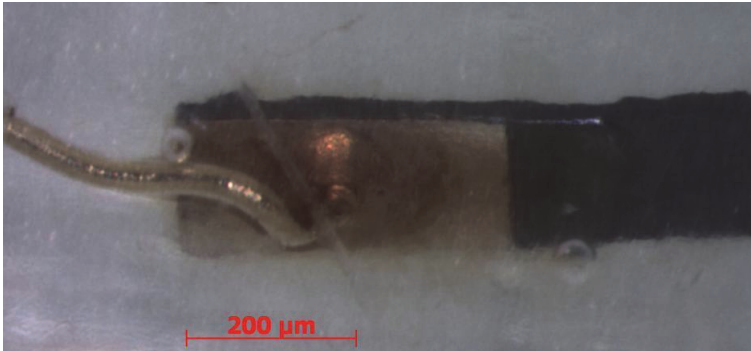


Figure 10: Normal junction

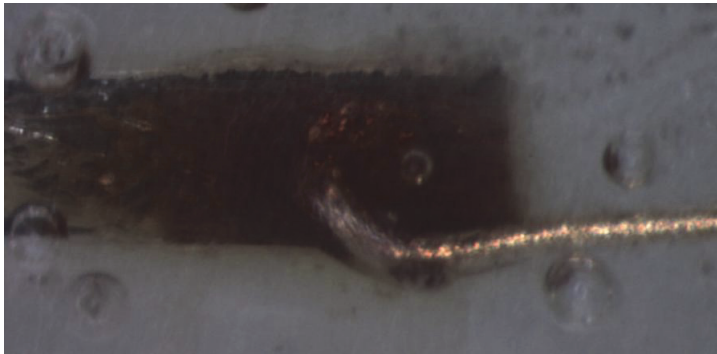


Figure 11: Corroded and delaminated junction

The corroded junction example has also easily distinguishable junction peel-off zone that probably caused the electrical failure. See Figure 12.

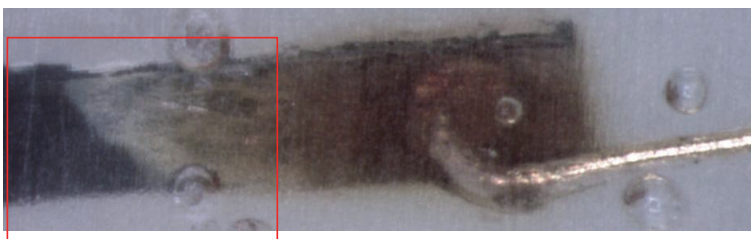


Figure 12: Delamination peel-off zone clearly identifiable on the left by white color

One specimen had aside visible junction peel-off signs also mechanical cracking of silicon crystal (see Figure 13). Based on that finding it is concluded the sensors, which were exposed to 0,15% strain could also fail due to semiconductor crystal cracking.



Figure 13: Sensor failure due to cracking

5 CONCLUSIONS AND FUTURE WORK

Fully embedded semiconductor strain gauge testing revealed that surrounding composite material matrix phase reduces the sensor strength appreciably. The environmental aging damages the sensor by corrosion and also reduces significantly sensors fatigue performance. It is critical to protect sensors from moisture attack, especially in the area of junction crystal-joint. The weakest link seems to be electrical junction contact point to the silicon plate. The strains in these regions should be relieved by some stress relieving geometrical solution. Aside the reduced strength properties the semiconductor strain gauges worked fairly well: no noticeable zero point drift, increased sensitivity or other anomaly was detected before the first signs of total failure. Using the silicon strain gauges seem to be good solution for detecting strains: the gauges have strong signal output, which is easily to measureable using simple voltage divider.

6 AKNOWLEDGEMENTS

Current work has been supported by EU structural funds project „Smart composites - design and manufacturing“3.2.1101.12-0012, target financings SF0140035s12 and SF0142737s06 and grants ETF8905 and ETF8485 (Estonian Science Foundation) and by the European Union through the European Regional Development Fund.

REFERENCES

[1] Y.Y. Li. Hypersensitivity of Strain-based Indicators for Structural Damage Identification: A Review. *Mechanical Systems and Signal Processing* 24(3), 653–664, 2010.

- [2] R. B. Watson, W. N. Sharpe. *Springer Handbook of Experimental Solid Mechanics: Bonded Electrical Resistance Strain Gages*. Springer US, 2008.
- [3] H. Choi, S. Choi, and H. Cha. Structural Health Monitoring System Based on Strain Gauge Enabled Wireless Sensor Nodes. *5th International Conference on Networked Sensing Systems 20*, 211–214, 2008.
- [4] A. L. Chateauminois, L. Vincent, B. Chabert and J.P. Soulier. Study of the Interfacial Degradation of a Glass-epoxy Composite During Hygrothermal Ageing Using Water Diffusion Measurements and Dynamic Mechanical Thermal Analysis. *Polymer 35(22)*, 4766–4774, 1994.
- [5] S. Pavlidou, C.D Paspaspyrides. The Effect of Hygrothermal History on Water Sorption and Interlaminar Shear Strength of Glass/polyester Composites with Different Interfacial Strength. *Composites Part A: Applied Science and Manufacturing 34(11)* 1117-1124, 2003.
- [6] J. Majak, M. Pohlak, M. Eerme, Application of the Haar Wavelet based discretization technique to orthotropic plate and shell problems, *Mechanics of Composite Materials*, 45(6), 631 – 642, 2009.
- [7] Karjust, K.; Pohlak, M.; Majak, J. Technology Route Planning of Large Composite Parts . *International Journal of Material Forming*, 3(Suppl:1), 631 – 634, 2010.
- [8] J. Lellep, J. Majak, Nonlinear constitutive behavior of orthotropic materials, *Mechanics of Composite Materials*, 36(4), 261 – 266, 2000.
- [9] M. Pohlak, J. Majak, K. Karjust, R. Küttner, Multicriteria optimization of large composite parts, *Composite Structures*, 92(9), 2146 – 2152, 2010.
- [10] J. Kers, J. Majak, Modelling a new composite from a recycled GFRP, *Mechanics of Composite Materials*, 44(6), 623 – 632, 2008.
- [11] J. Kers, J. Majak, D. Goljandin, A. Gregor, M. Malmstein, K. Vilsaar, Extremes of apparent and tap densities of recovered GFRP filler materials, *Composite Structures*, 92(9), 2097 – 2101, 2009.
- [12] J. Majak, M. Pohlak, Decomposition method for solving optimal material orientation problems, *Composite Structures*, 92(8), 1839 – 1845, 2010.
- [13] J. Majak, M. Pohlak, M., Optimal material orientation of linear and non-linear elastic 3D anisotropic materials, *Meccanica*, 45(5), 671 – 680, 2010.

[14] BCM Sensor Technologies bvba. Semiconductor strain gauges. Accessed: 25th March 2013, Hyperlink:<http://www.bcmsensor.com/sub-categories.php?secid=2>

Paper V

H. Herranen, H. Lend, A. Kuusik, S. Czichon, J. Kers, M. Piirlaid, "Foreign Object Induced Fiber Undulation Influence On Mechanical Properties Of Composite Laminate," in *Proceedings of 19th International Conference on Composite Materials (ICCM19)*, 2013.

FOREIGN OBJECT INDUCED FIBER UNDULATION INFLUENCE ON MECHANICAL PROPERTIES OF COMPOSITE LAMINATE

H. Herranen^{1*}, M. Eerme¹, H. Lend¹, A. Kuusik², S. Czichon³, J. Kers⁴, M. Piirlaid⁵

¹Department of Machinery, Tallinn University of Technology, Tallinn, Estonia

²ELIKO Competence Center, Tallinn, Estonia,

³Elan-Ausy GmbH, Hamburg,

⁴Department of Materials Engineering, Tallinn University of Technology, Tallinn, Estonia,

⁵Department of Polymer Materials, Tallinn Univ. of Technology, Tallinn Estonia

* Corresponding author (henrik.herranen@tu.ee)

Keywords: *embedded devices, composite laminate, DIC, additive layer manufacturing, optimization*

1 General Introduction

Composite materials have found a wide range of applications in engineering due to their high strength-to-weight ratio, resistance to fatigue and environmental influences. Fiber composites are laminated anisotropic materials, which damage is often not easily detectable. The increasing demand for structural health monitoring has stimulated efforts to integrate self-sensing capabilities into materials and structures. Surface mounted sensors are susceptible to damage and their protection from environment is often noticeable extra weight gain. Embedding the sensors in housing allows for protection from adverse environmental conditions. It is also the only means suitable for creating an autonomous structure with a smooth surface finish. Previous efforts to integrate sensors and MEMS devices into fiber-reinforced composites have often required that such a device be placed between the fiber layers of a composite as it is being fabricated. As a result, the device is usually surrounded by the matrix phase, typically a polymer, which is generally the weaker phase within the composite. Interlaminar stresses arise at or near the inclusions and could result in delamination, which in turn reduces load carrying capability and further reduces the ability of an embedded sensor to detect its surrounding environment. Therefore, it is necessary to characterize the effects of embedding sensors on the mechanical properties of the host structural composite material.

The main sources of problems are caused by elastic properties mismatch, specifically high difference of the modulus of elasticity.

Embedding electronics inside mechanically working composite creates a controversy. The metallic and semiconductor parts with high stiffness do not comply with the strains of operating composite and composite materials on the other hand do not match with the embedded foreign objects, which generate severe stress concentrations in the host structure.

Selective laser sintering (SLS) is technology, which allows layer-wise build-up of very complex geometrical shapes. It is an additive layer technology (ALT). SLS is technology which is feasible solution for manufacturing a enclosure around electronics, which are to be integrated inside the main material.

This article is focused on embedding SLS produced components inside main structure. SLS built enclosure around composite reduces the elasticity mismatch or even isolates the un-compatible materials from each other.

Inserting foreign object inside the laminate is similar to the effect of void on the composite structure. The change of geometry causes fiber undulation around the object and locally increased waviness. This change affects significantly structural performance of the composite [1]. Beside the undulation the embedded object has different elasticity – if it is electronics, then it is much stiffer and causes extra stresses. In this article SLS produced PA-12 nylon enclosure for electronics is inserted in the host material. The mechanical properties of PA-12 nylon are very similar to polyester resins and epoxy resins. Additionally SLS produced PA-12 nylon could weaken by hygrothermal influences [2]. A phenomenon called plasticization occurs. This

further reduces the mechanical strength of the two material interface. In order to simulate that, the foreign objects had no friction enhancing or room interlocking features to increase contact zone rigidity.

2 Methodology

Embedding the electronic components directly in composite may lead to impairments of the components during fabrication or exploitation of the composite structure (mechanical defects, overheating, etc). For that reason the additive layer technology has been employed for manufacturing housings which can host the electronic components. Any embedded components have impact on mechanical, thermal, etc properties of the composite structure. Thus, the design of housings is necessary. First the design of experiment has been performed. Next the specimens with ALT manufactured embedded structures are fabricated and mechanical tests performed.

The finite element (FE) model has been developed for modeling the stress-strain behavior of the composite structure with embedded components. The finite element model is validated through comparison with digital image correlation scanner results. Also, the results obtained from mechanical tests and FE model are compared. The FE model developed covers fiber undulation caused by embedded objects.

Based the experimental results the mathematical model is developed.

Finally the size and shape optimization of the embedded structure has been performed. The size of the pockets formed at ends of the embedded structure and the mechanical stresses around the embedded structure are considered as objective functions. The multicriteria optimization problem posed has been divided into multistage optimization procedure and solved by use of weighted summation technique. Due to presence of integer variables the genetic algorithm (GA) was employed.

3 Specimen design

It is correct to point out that in current context the design of specimen contains mainly design of housing for electronics which will be mounted in specimen (in addition to specimen dimensions, the shape and dimensions of the housing are considered as design variables).

The strength characteristics of the specimen have been analyzed. The following optimality criteria were selected

$$\begin{aligned} F_1 &= H(x_1, \dots, x_n) \rightarrow \min, \\ F_2 &= L(x_1, \dots, x_n) \rightarrow \min, \\ F_3 &= \alpha_{max}(x_1, \dots, x_n) \rightarrow \min, \\ F_4 &= \sigma_f(x_1, \dots, x_n) \rightarrow \max, \end{aligned} \quad (1)$$

where H, L, α_{max} and σ_f stand for the height and length of the pocket, maximal angle of the pocket diagonal side and failure stress, respectively. Parameters x_1, \dots, x_n stand for design variables.

Before selection of multicriteria optimization strategy it is important to understand general characteristic behaviour of the optimality criteria used [3,4,5]. Preliminary analysis of the optimality criteria (1) allows to conclude, that in general:

- The optimality criteria F_1, F_2, F_3 given by (1) are not contradictory (decrease or increase for the same dataset).
- The optimality criterion F_4 increase with decreasing values of criteria F_1, F_2, F_3 and vice versa. However, criterion F_4 is subjected to maximization, and there is not contradictory with criteria F_1, F_2, F_3 .

Thus, there is no need for applying Pareto optimality concept for handling conflicting objectives. In the following the weighted summation technique is employed. The objectives (1) should be first normalized, due to their different magnitude. The normalization is performed by formulas

$$f_i(\bar{x}) = \frac{F_i(\bar{x}) - \min F_i(\bar{x})}{\max F_i(\bar{x}) - \min F_i(\bar{x})}, \quad (2)$$

for objectives subjected to minimization (F_1, F_2, F_3) and by formulas

$$f_4(\bar{x}) = \frac{\max F_4(\bar{x}) - F_4(\bar{x})}{\max F_4(\bar{x}) - \min F_4(\bar{x})}, \quad (3)$$

for objectives subjected to maximization (F_4).

In (2)-(3) $i = 1, 2, 3$ and \bar{x} stands for the vector of design variables.

According to weighted summation technique the combined objective can be written as

$$f = \sum_{i=1}^m w_i f_i \rightarrow \min, \quad (4)$$

where w_i stand for the weights of the objectives (2)-(3) and are evaluated as

$$w_1 = w_2 = w_3 = w_4 = 0.25, \quad (5)$$

i.e. all are considered to have the same importance. The housings for embedded electronics with different shapes have different number of design parameters x_1, \dots, x_n . For that reason the two level optimization strategy has been introduced [6,7,8].

3.1. Higher level design

In higher level design stage the most suitable shape and size of the housing have been determined. The following geometrical shapes were considered:

- rectangular
- trapezoid
- round
- ellipse

The size of the each shape has been varied. Two parameters have been considered for each shape with the exception of trapezoid and circle. Circular cross-section has only diameter as variable and trapezoid has three parameters: height, width and the angle of sides relative to base. The full factorial design of experiment has been employed for shapes except trapezoid. In latter case the Taguchi design of experiment was applied. The size range was chosen to accommodate the structure to specific electronic device. Circular cross-section has no real application potential. It was used in order to investigate the fiber undulation around short object. The variables are discrete values as shown in Table 1.

Table 1: Variables of geometrical shapes

Shape	Length [mm]	Height [mm]	Side angle [°]
Ellipse	10; 25; 40;	1; 2; 3;	-
Circular	diameter 1.5mm; 2mm; 4mm;		
Rectangular	10; 25; 40;	1; 2; 3;	-
Trapezious	10; 25; 40;	1; 2; 3;	50; 53; 56;

The level values for Taguchi method is therefore 3. Three parameters and three levels would require in

full factorial testing 3^3 or 27 combinations. Taguchi design matrix is depicted in

Table 2. P1, P2 and P3 are parameters. Based on that methodology the trapezoid shape dimensions are derived as shown in Table 3.

Table 2 Parameter values and experiment

Experiment	P1	P2	P3
1	1	1	1
2	1	2	2
3	1	3	3
4	2	1	2
5	2	2	3
6	2	3	1
7	3	1	3
8	3	2	1
9	3	3	2

Table 3 Parameter values for trapezoid

Nr.	Width, mm	Height, mm	Angle, °
1	10	1	50
2	10	2	53
3	10	3	56
4	25	1	53
5	25	2	56
6	25	3	50
7	40	1	56
8	40	2	50
9	40	3	53

In the case of full factorial design, three parameters and three levels are needed $3^3 = 27$ testing combinations instead of 9 used for Taguchi design. Numerical analysis performed allows concluding that the ellipse appears to be most suitable shape of the housing. Also the optimal values of the height and width of the housing are found to converge to 1 and 25, respectively. However, the results depend on selected values of weights (5), also from accuracy of the measured values of objectives functions. The smaller height of the housing is obviously better – causing less damage of the structure by not influencing the straightness of fiber bundles. Actually here are a lot of options for the selection,

design of embedded electronics depending on its price, aptitude, etc. Unfortunately, not all variants of embedded electronics can be fitted in housing with height values equal to 1mm and even to 2 mm. Thus, different heights should be considered for future analysis (cost can be included).

3.2. Lower level design

In lower level design the selected elliptic shape of the housing is assumed, but certain improvement of the shape is introduced. Namely, the elliptic shape is divided into two parts, consisting from two ellipses with different half-axis (see Figure 1).

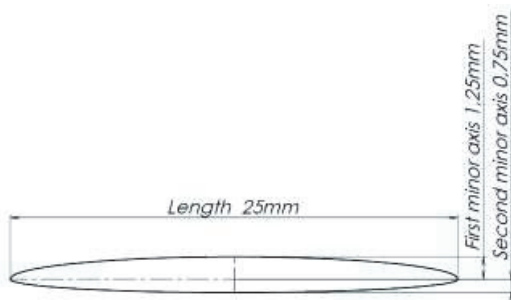


Figure 1 Design variables: minor half-axes

The minor half-axes of the ellipse are considered as design variables. For fixed values of the minor half-axes the major half-axes values are determined by total length of the ellipse and continuity conditions. The remaining design variable considered in lower level design is the length of the specimen.

Preliminary numerical results obtained include optimal design where the value of the length of specimen is near minimal value considered and the minor half-axes of the lower ellipse (see Figure 1) is substantially smaller than minor half-axes of the upper ellipse (1/2...1/4 depending on total height of the ellipse).

The mathematical model introduced for data fitting is based on use of artificial neural networks and is satisfactory. However, in order to improve the accuracy of the obtained results, the dataset used need to be completed, the design area enlarged (limits of design variables extended).

4 Experimental testing

4.1 Specimen manufacturing

The reinforcement is biaxial $0^\circ/90^\circ$ non-crimp type glass fiber fabric type Saint-Gobain ELT 600 125 FMA 5008 C with surface density 600g/m^2 . The matrix is vinylester resin ATLAC 580 ACT with hardener Butanox M50 (1,5% volume fraction of resin). The mechanical properties of the laminate are depicted in Table 4.

The foreign objects are manufactured with selective laser sintering machine EOS GmbH Formiga P100. Selective laser sintering technology allows to create complex shapes with almost no geometrical limits. The base material is PA-12 polymer (EOS PA2200). The foreign objects were cleaned with pressurized air and acetone before the lamination process to remove any residue from laser sintering process.

The foreign objects were laminated between 6 plies of laminate on the mid-plane, the lay-up notation is $[0^\circ/0^\circ/0^\circ/\text{ForeignObject}/0^\circ/0^\circ/0^\circ]$. The specimen was laminated at 0.8 bar vacuum and post-cured after manufacturing at 60°C for 16 hours.

The specimens were cut-out from workpiece with high speed milling machine at 32000 RPM with low feed rate in order to minimize the specimen edge delamination probability.

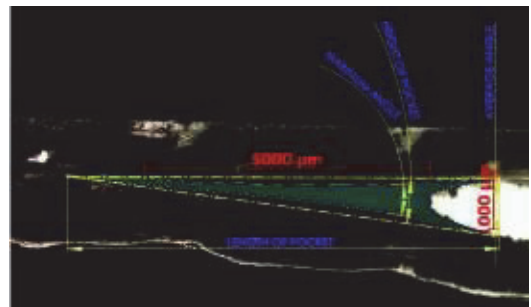


Figure 2 Resin pocket example

E_x, E_y	19,6GPa
E_z	5GPa
ν_{xy}	0,26
ν_{yz}	0,01
ν_{xz}	0,01
G_{xy}	3,28GPa
G_{xz}, G_{yz}	1,6GPa
σ_x^c, σ_y^c	215,9MPa
σ_x^t, σ_y^t	304,7MPa
$\tau_{xy}^{0,2}$	23,1MPa

Table 4 Mechanical properties of laminate

4.2 Examination of preliminary specimens

The undulation size and shape will be estimated from sectioned specimens with microphotography. The measurable parameters are depicted in Figure 2. It is known from various authors that fiber waviness is one of the most critical parameters of composite mechanical properties[11,12,]. In this article simple waviness parameters like amplitude and wavelength are not sufficient to describe the resin pocket properties. This is because the resin pocket around foreign object is single event not repeating pattern. Lemanski and Sutcliffe [10] measured fiber misalignment angle influence on the mechanical properties of unidirectional laminate. In this research the measurable parameters are as mentioned in methodology section the height H and length L of the pocket, maximal angle α_{max} and average angle α_{avg} of the pocket diagonal side and failure stress σ_f , respectively. All the parameters except of failure stress can be measured from microscope pictures. The examination results are shown for all three thicknesses accordingly in Table 5, Table 6 and Table 7.

The data from these tables was inserted in weighted summation optimization procedure. The weight values are taken from equation (5).

Table 5 measured parameters for 1 mm thick foreign objects. 1-ellipse, 2-rectangular, 3-trapezoid.

Shape	Length [mm]	Pocket height [μm]	Pocket length [μm]	Avg. undulation angle (°)	Max. Undulation angle (°)
1	10	689	5204	7	10,2
1	10	546	3169	9,3	10,6
1	25	648	8820	4	7,8
1	40	642	10790	3,6	8,4
1	40	995	11669	5,4	12
2	10	1184	9451	5	6,9
2	10	1257	10480	4,6	8,4
2	25	1077	11087	3,2	7
2	25	1256	11662	2	5
2	40	1248	13984	3	3,8
3	10	926	7119	8	10,7
3	25	986	9473	5,4	10,5
3	25	1063	9444	6,2	13,5
3	4	1057	7264	6,7	8,5

Table 6 Results for 2mm thick foreign objects

Shape	Length [mm]	Pocket height [μm]	Pocket length [μm]	Avg. undulation angle (°)	Max. Undulation angle (°)
1	1	1520	10280	4	7,3
1	1	1747	9984	3,3	5,7
1	2,5	1027	9036	4,6	6
1	4	1846	13830	6,4	9,8
2	1	2232	9976	9,8	17,7
2	1	2097	11546	9	14,5
2	2,5	2195	12760	9,6	16
2	4	2241	10582	7,8	12,1
3	1	1822	13736	6,8	10,1
3	2,5	1779	10533	8,3	14,6
3	4	1576	11467	9	16,6

Table 7 Results for 3mm thick foreign objects

Shape	Length [mm]	Pocket height [μm]	Pocket length [μm]	Avg. undulation angle (°)	Max. undulation angle (°)
1	1	2501	16746	5,2	8,6
1	1	2262	15335	6,7	10
1	2,5	951	8417	11,3	19,1
1	2,5	1301	8018	12,6	21
1	4	1544	18560	4	8,4
2	1	3151	13220	10	13,3
2	1	3420	13732	7,4	12,2
2	2,5	3000	11494	11	20
2	4	3069	11573	10,4	13,8
3	1	2483	13116	12,5	17,3
3	2,5	1722	8843	17	29
3	2,5	1596	6417	19	31
3	4	2643	13908	8,4	11

4.3 Design of new specimens

Based on the results of weighted summation optimization method the smallest influence on fiber undulation has ellipse with dimensions 25mm x 2mm. It was discovered during the microscopic examination procedure that some slender ellipses tried to conform to the flat manufacturing mould surface by bending the closer surface curvature to collinearity with mould surface. Therefore it is proposed that most suitable shape for foreign object should be instead composed of two half ellipses with different minor radiuses. Batch with different half ellipse combinations was manufactured. The length of ellipse stood the same 25mm value, but the minor radius combinations were varied as depicted in

Table 8. Two possible thicknesses for the whole foreign object were chosen. Also an un-common combination of half-ellipse and straight line was used(the sharp ends were rounded by fillet with radius 0,18mm).

Table 8 Dimensions of new specimens

Length [mm]	Minor radius 1, [mm]	Minor radius 2 [mm]	Total thickness [mm]
25	2,75	0,25	3
25	1,5	0,5	2
25	3	flat	3
25	1,75	0,25	2
25	1,25	0,75	2
25	2,5	0,5	3

4.4 Examination of new specimens

The new batch specimen had microphotography based measurements repeated analogically to the previous batch. The results are in Table 9.

Table 9 Results for new specimens

Shape	Pocket length [μm]	Pocket height [μm]	Avg. undulation angle (°)	Max. undulation angle (°)
1	4117	806	8,3	12,8
2	9203	1827	10,8	15
3	3650	764	8,8	12
4	14543	1653	5,5	11,3
5	1773	664	16,6	24
6	5705	1154	9,9	14,5

4.5 Mechanical testing

The specimens with embedded object were tested only for tensile loading. It was concluded from previous research [9] that the main source of failure is delamination initiated from resin pockets at the interface surface of foreign object and matrix. The failure mechanisms are similar for compression and tension, only difference is the properties reduction magnitude. The tensile testing is less sensitive to manufacturing faults, therefore it was chosen as more reliable method. Testing was carried out with tensile testing machine Instron 8516 coupled with digital image correlation (DIC) scanner GOM ARAMIS 2M. The base standard for test settings was ISO 527-4(equivalent to ASTM D3039). The

testing results are depicted on Figure 3 and summarized in Table 10.

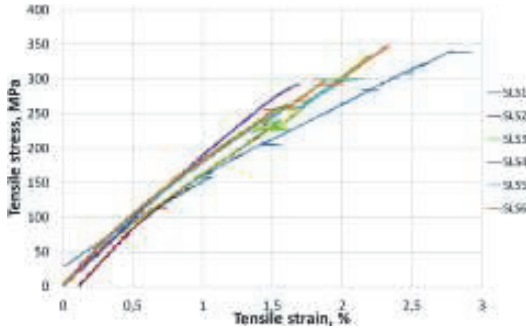


Figure 3 Tensile testing results chart

No.	Thickness of undist. section [mm]	Thickest point at for.object [mm]	Minor radius 1 [mm]	Minor radius 2 [mm]	Failure stress [MPa]
SLS1	3,12	6,4	2,75	0,25	155,6
SLS2	2,93	5,3	1,5	0,5	231,6
SLS3	3,1	6,6	3	0	236,1
SLS4	3	5,3	1,75	0,25	202,8
SLS5	3	5,1	1,25	0,75	261,2
SLS6	3	6,3	2,5	0,5	252,3
Average:					223,28

Table 10 Tensile testing results

The highest strength had specimen number 5, which was 16,9% higher than the average. This specimen had also very small resin pocket which was tightly packed by three 90° fiber yarns. Cross-section image is shown in Figure 4. The tensile strength was determined from DIC scanning images. The laminate was considered to failed after the first macrocrack occurrence.



Figure 4 Specimen number 5 cross-section image. Foreign object visible at the right side of the picture.

4.6 Digital image correlation results

The strain distribution around and inside the embedded device was measured in thickness direction at the side of the specimen using digital image correlation scanner GOM ARAMIS 2M similarly to one of the authors previous works [9]. The surface strains of the specimens were measured with a digital image correlation system (DIC) GOM ARAMIS 2M. The measuring volume was set to 35 mm x 25 mm. System measuring parameters were as follows: the computational size was set to 3, validity quote to 55%. The computation type was set to total strain method and plane stress.

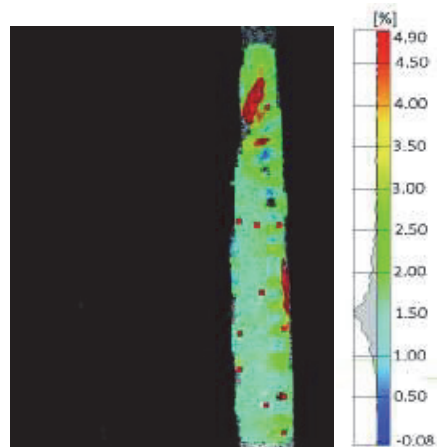


Figure 5 The strain distribution of specimen 5 at failure stress

The major strain distribution around on the specimen edge is shown in Figure 5. It is evident that the delamination starts from the resin pocket, although it is quite small.

5 Conclusions

The two level optimization procedure is developed for solving multicriteria optimization problem posed. An analysis of the optimality criteria is performed and the weighted summation technique applied. The response modeling is utilized by use of artificial neural networks. The multilevel optimization strategy proposed allows decomposing initial problem into two simpler tasks, which can be solved sequentially. The obtained numerical results contain optimal shape and size of the housing for embedded electronics. The optimization procedure helps to minimize the resin pocket dimensions, which criticality as a delamination starting point has been verified by the digital image correlation scanning.

6 Acknowledgement

This research was supported by the EU structural funds project „Smart Composites - Design and Manufacturing“ 3.2.1101.12-0012, ETF grant 8485 and targeted financing project SF0140035s12.

References

- [1] H.-J. Chun, J.-Y. Shin, I.M. Daniel “Effects of material and geometric nonlinearities on the tensile and compressive behavior of composite materials with fiber waviness”. *Composite Science and Tehnology*, Vol. 61, No. 1, pp 125-134, 2001.
- [2] R. Seltzer, F.M. Escalera, J. Segurado “Effect of water conditioning on the fracture behavior of PA12 composites processed by selective laser sintering”. *Materials Science and Engineering:A*, Vol. 528, No. 22-23, pp 6927-6933, 2011.
- [3] M. Pohlak, J. Majak, K. Karjust, R. Küttner (2010). “Multicriteria optimization of large composite parts” *Composite Structures*, Vol.92 No.9, 2146 - 2152.
- [4] K. Karjust, M. Pohlak, J. Majak “Technology Route Planning of Large Composite Parts” *International Journal of Material Forming*, Vol.3 No.1, pp631 – 634, 2010.
- [5] M. Pohlak, R. Küttner, J. Majak “Modeling and optimal design of sheet metal RP&M processes”. *Rapid Prototyping Journal*, Vol.11, No.5, pp 304 – 311, 2005
- [6] J. Majak, M. Pohlak., Decomposition method for solving optimal material orientation problems. *Composite Structures*, Vol.92, No.8, pp 1839 – 1845, 2010.
- [7] J. Majak, M. Pohlak. (2010). “Optimal material orientation of linear and non-linear elastic 3D anisotropic materials. *Meccanica*, 45(5), 671 - 680.
- [8] Lellep, J.; J. Majak (2000). Nonlinear constitutive behavior of orthotropic materials. *Mechanics of Composite Materials*, 36(4), 261 - 266.
- [9] H.Herranen, G. Allikas, M.Eerme, K. Vene, A. Gregor, T.Otto, M. Kirs, K. Mädamürk, “Visualization of strain distribution around the edges of a rectangular foreign object inside the woven carbon fibre specimen”. *Estonian Journal of Engineering*, Vol.18, No.4, pp279-287, 2012.
- [10] S.L.Lemanski, M.P.F. Sutcliffe, “Compressive failure of finite size unidirectional composite laminates with a region of fibre waviness” *Composites Part A: Applied Science and Manufacturing* Vol. 43, No.3, pp435–444, 2012
- [11]H. Chun,J. Shin, and I.M. Daniel. Effects of material and geometric nonlinearities on the tensile and compressive behavior of composite materials with fiber waviness. *Composites Science and Technology*, Vol.61, No.1, pp125-134, 2001.
- [12] G. Karami, M.Garnich „Effective moduli and failure considerations for composites with periodic fiber waviness.“ *Composite Structures*, Vol.67, No.4, pp461-475, 2005.

ELULOOKIRJELDUS

1. Isikuandmed

Ees- ja perekonnanimi	Henrik Herranen
Sünniaeg ja -koht	16.01.1985 Tallinn, Eesti Vabariik
Kodakondsus	Eesti
Telefon	6203270
E-posti aadress	henrik.herranen@ttu.ee

2. Hariduskäik

Õppeasutus (nimetus lõpetamise ajal)	Lõpetamisaeg	Haridus (eriala/kraad)
Tallinna Tehnikaülikool	2009	Tootearenduse eriala (magister)
Tallinna Tehnikaülikool	2007	Tootearenduse eriala (bakalaureus)
Tallinna Saksa Gümnaasium	2003	(keskharidus)

3. Keelteoskus (alg-, kesk- või kõrgtase)

Keel	Tase
Eesti keel	kõrgtase
Inglise keel	kõrgtase
Saksa keel	kesktase
Soome keel	algtase
Vene keel	algtase

4. Täiendusõpe

Õppimise aeg	Täiendusõppe korraldaja nimetus
05.2007	GOM ATOS II, ARAMIS 2M, ARGUS kasutajakoolitus Cascade Computing AB
02.2008-04.2008	„Orgaanilised komposiitmaterjalid täiendusõppe kursus” TTÜ
02.2009	ANSYS V12.1 kasutajakoolitus Process Flow Ltd OY

05.2010	CadON Consulting OÜ, Solidworks Simulation Premium FEM tarkvara koolitus
05.2012	GOM PONTOS 4M kasutajakoolitus, Cascade Computing AB
09.2013	ANSYS ACP kasutajakoolitus Medeso OY

5. Teenistuskäik

Töötamise aeg	Tööandja nimetus	Ametikoht
2007-...	Tallinna Tehnikaülikool, Masinaehituse instituut	nooremteadur
2009-2011	Nor-Tek Tehnologisenter AS (Norra)	tehnik
2006-2006	KT Arengu AS	mehaanikainsener
2004 - 2005	Golden Neo-Life Diamite International OÜ	tellimuste vormistaja - klienditeenindaja

6. Kaitstud lõputööd

Magistritöö: Laternaposti optimeerimine Flagmore AS, 2009, Tallinna Tehnikaülikool

Bakalaureusetöö: Järelhaagise katsetussüsteem Bestnet AS, 2007, Tallinna Tehnikaülikool

Juhendaja lõputöödele:

Tarko Koger, magistrikraad, 2013, (juh) Henrik Herranen, Teraapiakapsli kaane kontseptsioonid, Tallinna Tehnikaülikool, Mehaanikateaduskond, Masinaehituse instituut

Kaasjuhendaja lõputöödele:

Henri Saar, magistrikraad, 2013, (juh) Henri Lend, Henrik Herranen, APJ freespingi kahetelgse töötluspea konstrueerimine, Tallinna Tehnikaülikool, Mehaanikateaduskond, Masinaehituse instituut

Georg Allikas, magistrikraad, 2010, (juh) Jaan Kers, Henrik Herranen, Sandwich-tüüpi komposiitmaterjalist paneeli tugevusanalüüs ja materjali valik, Tallinna Tehnikaülikool

7. Teadustöö

- Projekti tehnilise külje administraator Archimedes projektil AR 12139 “Smart Composites – Design and Manufacturing”
- Projekti TTÜ-poolse tehnilise arendustegevuse koordinaator FP7 projektis “EmerEEG”.

Teadustöö põhisuunad:

- Lõplike elementide meetod kasutades modelleerimist
- Komposiitmaterjalide projekteerimine ning optimeerimine
- Komposiitmaterjalide seisundi monitoorimine (vibratsiooni- ja deformatsiooni-põhised meetodid)
- Eksperimentaalne katsetamine 3D skanneritega GOM PONTOS 4M ja GOM ARAMIS 2M

CURRICULUMVITAE

1. Personal data

Name	Henrik Herranen
Date and place of birth	16.01.1985 Tallinn, Estonia
Phone	(+372)6203270
E-mail address	henrik.herranen@ttu.ee

2. Education

Educational institution	Graduation year	Education (field of study/degree)
Tallinn University of Technology	2009	Product development (MSc)
Tallinn University of Technology	2007	Product development (BSc)
Tallinn German Gymnasium	2003	(Highschool education)

3. Language competence (fluent, average, basic skills)

Language	Level
Estonian	fluent
English	fluent
German	average
Finnish	basic skills
Russian	basic skills

4. Special courses

Period	Educational or other organisation
05.2007	GOM ATOS II, ARAMIS 2M, ARGUS end-user training Cascade Computing AB
02.2008-04.2008	„Course of Organic Composite Materials" TUT
02.2009	ANSYS V12.1 software training, Process Flow Ltd OY
05.2010	CadON Consulting OÜ, Solidworks Simulation Premium FEM software training
05.2012	GOM PONTOS 4M end user training, Cascade Computing AB
09.2013	ANSYS ACP software training, Medeso OY

5. Professional Employment

Period	Organization	Position
2007-...	Tallinn University of Technology Department of Machinery	Junior-Researcher
2009-2011	Nor-Tek Teknologisenter A/S (Norway)	Technician
2006-2006	KT Arengu Ltd	Mechanical engineer
2004-2005	Golden Neo-Life Diamite International Ltd	Order handler, customer service

6. Defended theses

Master thesis: Optimization of Lightning Column for Flagmore Ltd, 2009, Tallinn University of Technology, Department of Machinery

Bachelor thesis: Experimental measuring system for towing trailer Bestnet Ltd, 2007, Tallinn University of Technology

Supervisor for master thesis:

Tarko Koger, master degree, 2013, Henrik Herranen, Therapy capsule cover concepts, Tallinn University of Technology, Department of Machinery

Co-supervisor for master's theses:

- Henri Saar, masters degree, 2013, (sup.) Henri Lend, Henrik Herranen, Design of 2-axis machining head for CNC machine tool, Tallinn University of Technology, Department of Machinery
- Georg Allikas, masters degree, 2010, (sup.) Jaan Kers, Henrik Herranen, Strength calculation and material selection for composite material sandwich panel, Tallinn University of Technology, Department of Materials Engineering.

7. Main areas of scientific work:

- Technical administrator of Archimedes project AR 12139 "Smart Composites – Design and Manufacturing"
- TUT participation technical development coordinator of FP7-SME project EmerEEG.

Current research topics:

- Application of finite element method
- Development and optimization of composite materials
- Structural health monitoring of composite materials (vibration and strain based methods)
- Experimental testing with 3D scanners GOM PONTOS 4M ja GOM ARAMIS 2M.

**DISSERTATIONS DEFENDED AT
TALLINN UNIVERSITY OF TECHNOLOGY ON
*MECHANICAL ENGINEERING***

1. **Jakob Kübarsepp**. Steel-Bonded Hardmetals. 1992.
2. **Jakub Kõo**. Determination of Residual Stresses in Coatings & Coated Parts. 1994.
3. **Mart Tamre**. Tribocharacteristics of Journal Bearings Unlocated Axis. 1995.
4. **Paul Kallas**. Abrasive Erosion of Powder Materials. 1996.
5. **Jüri Pirso**. Titanium and Chromium Carbide Based Cermets. 1996.
6. **Heinrich Reshetnyak**. Hard Metals Serviceability in Sheet Metal Forming Operations. 1996.
7. **Arvi Kruusing**. Magnetic Microdevices and Their Fabrication methods. 1997.
8. **Roberto Carmona Davila**. Some Contributions to the Quality Control in Motor Car Industry. 1999.
9. **Harri Annuka**. Characterization and Application of TiC-Based Iron Alloys Bonded Cermets. 1999.
10. **Irina Hussainova**. Investigation of Particle-Wall Collision and Erosion Prediction. 1999.
11. **Edi Kulderknup**. Reliability and Uncertainty of Quality Measurement. 2000.
12. **Vitali Podgurski**. Laser Ablation and Thermal Evaporation of Thin Films and Structures. 2001.
13. **Igor Penkov**. Strength Investigation of Threaded Joints Under Static and Dynamic Loading. 2001.
14. **Martin Eerme**. Structural Modelling of Engineering Products and Realisation of Computer-Based Environment for Product Development. 2001.
15. **Toivo Tähemaa**. Assurance of Synergy and Competitive Dependability at Non-Safety-Critical Mechatronics Systems design. 2002.
16. **Jüri Resev**. Virtual Differential as Torque Distribution Control Unit in Automotive Propulsion Systems. 2002.
17. **Toomas Pihl**. Powder Coatings for Abrasive Wear. 2002.
18. **Sergei Letunovitš**. Tribology of Fine-Grained Cermets. 2003.
19. **Tatyana Karaulova**. Development of the Modelling Tool for the Analysis of the Production Process and its Entities for the SME. 2004.
20. **Grigori Nekrassov**. Development of an Intelligent Integrated Environment for Computer. 2004.
21. **Sergei Zimakov**. Novel Wear Resistant WC-Based Thermal Sprayed Coatings. 2004.
22. **Irina Preis**. Fatigue Performance and Mechanical Reliability of Cemented Carbides. 2004.
23. **Medhat Hussainov**. Effect of Solid Particles on Turbulence of Gas in Two-Phase Flows. 2005.
24. **Frid Kaljas**. Synergy-Based Approach to Design of the Interdisciplinary Systems. 2005.

25. **Dmitri Neshumayev.** Experimental and Numerical Investigation of Combined Heat Transfer Enhancement Technique in Gas-Heated Channels. 2005.
26. **Renno Veinthal.** Characterization and Modelling of Erosion Wear of Powder Composite Materials and Coatings. 2005.
27. **Sergei Tisler.** Deposition of Solid Particles from Aerosol Flow in Laminar Flat-Plate Boundary Layer. 2006.
28. **Tauno Otto.** Models for Monitoring of Technological Processes and Production Systems. 2006.
29. **Maksim Antonov.** Assessment of Cermets Performance in Aggressive Media. 2006.
30. **Tatjana Barashkova.** Research of the Effect of Correlation at the Measurement of Alternating Voltage. 2006.
31. **Jaan Kers.** Recycling of Composite Plastics. 2006.
32. **Raivo Sell.** Model Based Mechatronic Systems Modeling Methodology in Conceptual Design Stage. 2007.
33. **Hans Rämmal.** Experimental Methods for Sound Propagation Studies in Automotive Duct Systems. 2007.
34. **Meelis Pohlak.** Rapid Prototyping of Sheet Metal Components with Incremental Sheet Forming Technology. 2007.
35. **Priidu Peetsalu.** Microstructural Aspects of Thermal Sprayed WC-Co Coatings and Ni-Cr Coated Steels. 2007.
36. **Lauri Kollo.** Sinter/HIP Technology of TiC-Based Cermets. 2007.
37. **Andrei Dedov.** Assessment of Metal Condition and Remaining Life of In-service Power Plant Components Operating at High Temperature. 2007.
38. **Fjodor Sergejev.** Investigation of the Fatigue Mechanics Aspects of PM Hardmetals and Cermets. 2007.
39. **Eduard Ševtšenko.** Intelligent Decision Support System for the Network of Collaborative SME-s. 2007.
40. **Rünno Lumiste.** Networks and Innovation in Machinery and Electronics Industry and Enterprises (Estonian Case Studies). 2008.
41. **Kristo Karjust.** Integrated Product Development and Production Technology of Large Composite Plastic Products. 2008.
42. **Mart Saarna.** Fatigue Characteristics of PM Steels. 2008.
43. **Eduard Kimmari.** Exothermically Synthesized B₄C-Al Composites for Dry Sliding. 2008.
44. **Indrek Abiline.** Calibration Methods of Coating Thickness Gauges. 2008.
45. **Tiit Hindreus.** Synergy-Based Approach to Quality Assurance. 2009.
46. **Karl Raba.** Uncertainty Focused Product Improvement Models. 2009.
47. **Riho Tarbe.** Abrasive Impact Wear: Tester, Wear and Grindability Studies. 2009.
48. **Kristjan Juhani.** Reactive Sintered Chromium and Titanium Carbide-Based Cermets. 2009.
49. **Nadežda Dementjeva.** Energy Planning Model Analysis and Their Adaptability for Estonian Energy Sector. 2009.

50. **Igor Krupenski**. Numerical Simulation of Two-Phase Turbulent Flows in Ash Circulating Fluidized Bed. 2010.
51. **Aleksandr Hlebnikov**. The Analysis of Efficiency and Optimization of District Heating Networks in Estonia. 2010.
52. **Andres Petritšenko**. Vibration of Ladder Frames. 2010.
53. **Renee Joost**. Novel Methods for Hardmetal Production and Recycling. 2010.
54. **Andre Gregor**. Hard PVD Coatings for Tooling. 2010.
55. **Tõnu Roosaar**. Wear Performance of WC- and TiC-Based Ceramic-Metallic Composites. 2010.
56. **Alina Sivitski**. Sliding Wear of PVD Hard Coatings: Fatigue and Measurement Aspects. 2010.
57. **Sergei Kramanenko**. Fractal Approach for Multiple Project Management in Manufacturing Enterprises. 2010.
58. **Eduard Latõsov**. Model for the Analysis of Combined Heat and Power Production. 2011.
59. **Jürgen Riim**. Calibration Methods of Coating Thickness Standards. 2011.
60. **Andrei Surzhenkov**. Duplex Treatment of Steel Surface. 2011.
61. **Steffen Dahms**. Diffusion Welding of Different Materials. 2011.
62. **Birthe Matsi**. Research of Innovation Capacity Monitoring Methodology for Engineering Industry. 2011.
63. **Peeter Ross**. Data Sharing and Shared Workflow in Medical Imaging. 2011.
64. **Siim Link**. Reactivity of Woody and Herbaceous Biomass Chars. 2011.
65. **Kristjan Plamus**. The Impact of Oil Shale Calorific Value on CFB Boiler Thermal Efficiency and Environment. 2012.
66. **Aleksei Tšinjan**. Performance of Tool Materials in Blanking. 2012.
67. **Martinš Sarkans**. Synergy Deployment at Early Evaluation of Modularity of the Multi-Agent Production Systems. 2012.
68. **Sven Seiler**. Laboratory as a Service – A Holistic Framework for Remote and Virtual Labs. 2012.
69. **Tarmo Velsker**. Design Optimization of Steel and Glass Structures. 2012.
70. **Madis Tiik**. Access Rights and Organizational Management in Implementation of Estonian Electronic Health Record System. 2012.
71. **Marina Kostina**. Reliability Management of Manufacturing Processes in Machinery Enterprises. 2012.
72. **Robert Hudjakov**. Long-Range Navigation for Unmanned Off-Road Ground Vehicle. 2012.
73. **Arkadi Zikin**. Advanced Multiphase Tribo-Functional PTA Hardfacings. 2013.
74. **Alar Konist**. Environmental Aspects of Oil Shale Power Production. 2013.
75. **Inge Roos**. Methodology for Calculating CO₂ Emissions from Estonian Shale Oil Industry. 2013.
76. **Dmitri Shvarts**. Global 3D Map Merging Methods for Robot Navigation. 2013.

77. **Kaia Lõun.** Company's Strategy Based Formation of e-Workplace Performance in the Engineering Industry. 2013.
78. **Maido Hiimaa.** Motion Planner for Skid-Steer Unmanned Ground Vehicle. 2013.
79. **Dmitri Goljandin.** Disintegrator Milling System Development and Milling Technologies of Different Materials. 2013.
80. **Dmitri Aleksandrov.** Light-Weight Multicopter Structural Design for Energy Saving. 2013.
82. **Heiki Tiikoja.** Experimental Acoustic Characterization of Automotive Inlet and Exhaust System. 2014